Electrochemical Characterization and Development of Nickel-based Materials as Oxygen Evolution, Hydrogen Evolution, and Urea Oxidation Electrocatalysts

Isaac Kretzmer

A dissertation
submitted in partial fulfillment of the
requirements for the degree of

Doctor of Philosophy

University of Washington
2023

Reading Committee:
Eric M. Stuve, Chair
Stuart Adler
Daniel Schwartz

Program Authorized to Offer Degree:
Chemical Engineering

University of Washington

Abstract

Electrochemical Characterization and Development of Nickel-based Materials as Oxygen Evolution, Hydrogen Evolution, and Urea Oxidation Electrocatalysts

Isaac Kretzmer

Chair of the Supervisory Committee:
Professor Eric M. Stuve
Chemical Engineering

In the past decade, energy generation using solar, wind, and hydroelectricity has increased dramatically. Widespread adoption of these renewable sources, however, is bottlenecked by energy conversion and storage devices such as fuel cells and batteries. Hydrogen is a promising energy carrier that can be produced through low temperature alkaline water electrolysis, stored as a gas or liquid, and later converted back to electrical energy when needed. The cost-effectiveness of a hydrogen-based energy storage system, however, is in part limited by the high electrochemical overpotentials needed to drive the hydrogen evolution reaction (HER), oxygen evolution reaction (OER), and/or urea oxidation reaction (UOR). Consequently, development and understanding of advanced electrocatalysts is a critical step in realizing hydrogen energy for grid-scale power applications.

In this work, nickel and nickel-transition metal alloys were investigated as HER, OER, and UOR catalysts. Reproducible oxide layers were grown by potential cycling between 0.85 and 1.52 V *vs.* RHE up to 600 cycles, and the transition between $Ni(OH)_2$ and NiOOH was monitored by cyclic voltammetry throughout. Through voltammograms and a Tafel analysis, it was determined that dissolution of chromium and molybdenum led to the formation of high electrochemical surface area electrodes with increased formation of the γ-NiOOH phase. Alloys with dissimilar Cr:Mo ratios leached significantly more, suggesting an electrode with

similarly high Cr and Mo content is more stable in the examined conditions. Dissolution of Cr was verified through the use of x-ray impedance spectroscopy. The equal Cr:Mo concentration alloy and pure Ni developed a primarily β-NiOOH surface, and had 1.8–2.0 times larger TOF values than those containing significant γ-NiOOH. The NiCrMo alloys required smaller overpotentials (54–80 mV) to produce 10 mA cm^{-2} of OER current, and had comparable Tafel slopes to pure Ni. The findings here indicate a β-NiOOH-developed surface to be more OER-active than a γ-NiOOH-developed surface and suggest certain NiCrMo alloys have promise as OER electrocatalysts.

Next, the OER-active nickel-oxyhydroxide (NiOOH) phases were characterized using cyclic voltammetry, impedance spectroscopy, and scanning electron microscopy on pure Ni. Using selective electrochemical cycling from 0.9 V_{RHE} to switching potentials between 1.51 and 1.61 V_{RHE} in 0.5 M KOH at 25 °C, it was determined that the γ-NiOOH phase would preferentially form at higher switching potentials. This phenomenon was attributed to induced surface roughening through NiOOH lattice expansion and contraction, thereby enhancing electrochemical surface area (ECSA) and improving the intercalation of cations. The resulting increase in the number of grain boundaries was verified through scanning electron microscopy. Kinetics of the OER were evaluated using Tafel analysis and turnover frequency (TOF); an electrode developed with a switching potential of 1.51 V_{RHE} had TOF values 6–17 times larger than an electrode developed with a switching potential of 1.61 V_{RHE}, indicating improved OER kinetics of the β-NiOOH phase. The results from this study provided evidence for the relative activity of NiOOH phases, and showed that selective electrochemical cycling can be used to control the formation of NiOOH species.

The findings in these studies indicate that, while alkaline water electrolysis is a mature technology, there is still significant room for improvement using nickel-based electrodes. Moreover, the techniques developed here may have application in other NiOOH-based systems for examining and improving their electrocatalytic performance.

TABLE OF CONTENTS

LIST OF FIGURES

Figure Number Page

LIST OF TABLES

Table Number Page

ACKNOWLEDGMENTS

I am incredibly grateful to the many people who have supported and defined my graduate school experience over the past 5 years. First, I would like to thank everyone on my committee for their valuable feedback and involvement throughout the years: Prof. Eric Stuve, Prof. Stuart Adler, Prof. Dan Schwartz, and Prof. Lara Gamble. Eric Stuve, especially, has extended exceptional support and guidance as my PI throughout the program. From electrochemistry to font theory, Eric is a tremendous knowledge resource who has provided more assistance in succeeding as a graduate researcher than I could have asked for.

A huge thank you to all my Seattle friends and UW colleagues, with extra appreciation for Dr. Orion Dollar, Jeremy Filteau, Hawley Helmbrecht, Sage Scheiwiller, Julia Boese, Anthony Pyka, Maria Politi, Giang Le, Dr. Kelly Carpenter, Dr. Jon Witt, Dr. Brian Gerwe, and Mia Ragozino. Additionally, my friends from Los Angeles, Tucson, and all the stops along the way; whether through school, tabletop games, or fantasy football, you have all helped me make it to this point.

Finally, to my incredibly supportive family: My mom, Pat, my dad, Tony, my sister, Hanna, and my partner, Davanna, who all — in countless forms — have been there every step of the way. Your encouragement, support, and love have been endless, and this would absolutely not have been possible without each of you.

DEDICATION

To my family and friends, your support has been everything.

Chapter 1

INTRODUCTION

In the past decade, energy generation through renewable energy sources (RES) has dramatically increased; between 2008 and 2019, energy produced by RES — including wind, hydroelectric, solar, and thermal sources — increased from 7.9% to 16.3%, as shown in Figure 1.1.[1] While the amount of power generated by RES is generally predictable, their

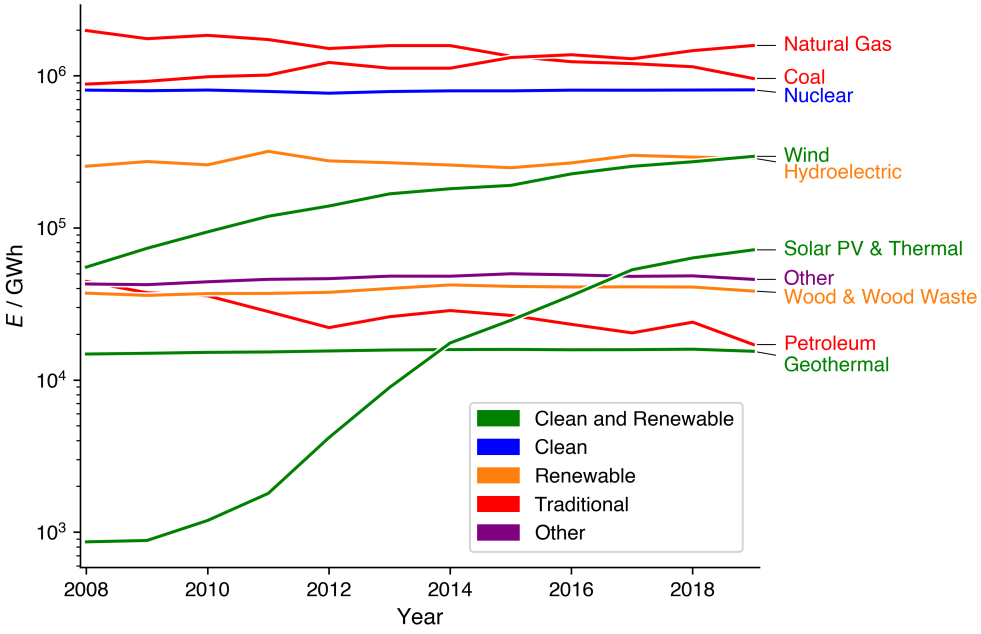

Figure 1.1: U.S. energy production by source. [1] 'Other' consists of combined renewable, clean, and traditional energy sources. Interactive version and additional visualizations available at: https://observablehq.com/@isaack8/energy-visualizations

intermittency introduces issues regarding electrical stability and availability. As a result, the absence of efficient and affordable technologies for electricity storage remains a major hindrance towards the widespread adoption of clean, renewable energy.[2, 3] This bottleneck has led to the development of energy storage systems (ESS). ESS are used to decouple energy production from demand by converting electrical energy to magnetic, chemical, kinetic, or potential energy. By storing energy during excessive generation periods and supplying energy during periods of high demand, the availability of electricity for the residential and industrial sectors is more consistent and intermittency issues can be minimized. Pumped hydroelectric is by far the most common form of ESS, accounting for approximately 95% of the U.S. — and 90% globally — utility-scale energy storage.[4] While an effective and tested renewable form of ESS, recent studies indicate the greenhouse gas costs of water storage reservoirs are more significant than previously believed. Methane, a potent greenhouse gas, makes up 80% of water storage reservoir emissions.[5] Anoxic methane production occurs in the pores of fine-grained sediment that accumulate in water reservoirs, while organic material from decaying vegetation or watershed runoff will decompose to form methane.[6] When water levels in the reservoir lower, the decrease in hydrostatic pressure allows stored methane to escape and subsequently enter the atmosphere.[6] As a result, emerging technologies such as grid-scale batteries and hydrogen storage have the potential to greatly increase grid storage capacity and reliability while reducing the overall carbon footprint of ESSs.

Advancements in ESS technologies are greatly dependent on electrochemical materials research and development. In particular, nickel (Ni) is designated a “high importance” mineral for the development of electric vehicles, battery storage, and hydrogen technologies.[7] Ni is a major component in common secondary (rechargeable) lithium-ion batteries such as nickel-cobalt-aluminum and nickel-manganese-cobalt as well as the nickel-metal hydride battery often used in consumer electronics. Consequently, Ni is an essential material in the development of advanced battery technologies for grid-scale energy storage applications.[8]

Nickel-based catalysts also have a prominent role in the field of hydrogen fuel production through alkaline water electrolysis (AWE). In AWE, hydrogen gas is produced through the hydrogen evolution half reaction (HER), where water is reduced at the cathode surface. At the anode, the oxygen evolution half reaction (OER) occurs when hydroxide ions are oxidized to form oxygen gas. While this reaction is clean, the electricity input required to drive AWE results in a more expensive process than producing hydrogen through fossil fuels and other production methods. As a result, efficient and low-cost electrocatalysts are a necessary development before hydrogen as an ESS can be actualized. Nickel is an especially attractive option for AWE due to its low cost, high electrical conductivity, and resistance to corrosive alkaline environments.[9] Ni acts as a bifunctional catalyst for AWE, capable of operating as the anode, cathode, or both. Nickel can take on a variety of forms, including nickel-foam, a porous, high-surface area material that is ideal for electrocatalytic applications. Moreover, Ni often has a synergistic relationship with additive elements such as iron, cobalt, chromium, and molybdenum, enhancing the electrocatalytic properties of the material as a whole.[10]

Compared to the HER, however, the OER is a complex, 4-electron reaction with sluggish kinetics; the high overpotential required to drive the OER hinders the overall efficiency of AWE. Consequently, development of stable, low-cost Ni-based materials for high-efficiency OER is an intensely studied field, and there have been more publications regarding Ni for the OER than the HER, as seen in Figure 1.2.

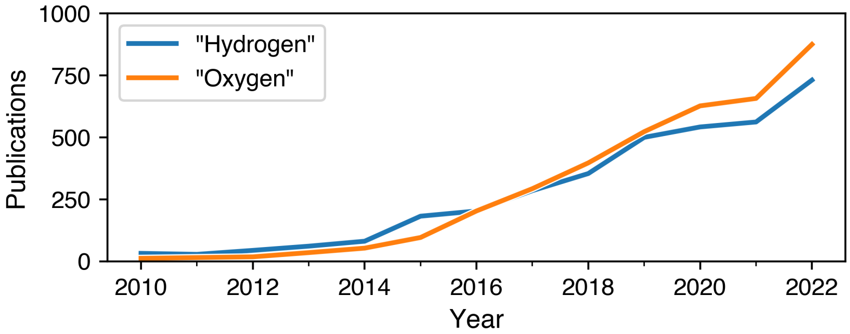

Figure 1.2: Publications by year with titles or abstracts containing the words “Nickel” and “X Evolution”, where X is either “Hydrogen” or “Oxygen”.[11]

In the past two decades, the discovery of nickel's affinity for the urea oxidation reaction (UOR) has led to a new research focus. Urea is the largest constituent in urine, Earth's most abundant waste product.[12] Through urea electrolysis, Ni splits urea into gaseous carbon dioxide and nitrogen at the anode, while hydrogen is produced at the cathode. Additionally, the lower overpotential of the UOR compared to the OER reduces the energy input required to drive hydrogen formation. In this system, Ni is capable of facilitating the production of low-cost hydrogen while simultaneously treating urea-rich wastewater, as shown in Figure 1.3.

This work is motivated by the need for a transition to efficient, reliable, and clean energy production and storage methods. Hydrogen storage is a promising option, and Ni, consequently, is an important material in the development of this ESS technology. The focus of this research is to advance the understanding and development of Ni-based materials for use in electrochemical applications, specifically the oxygen evolution half-reaction. While the HER is the electrochemical process by which hydrogen — the fuel of interest in AWE — is

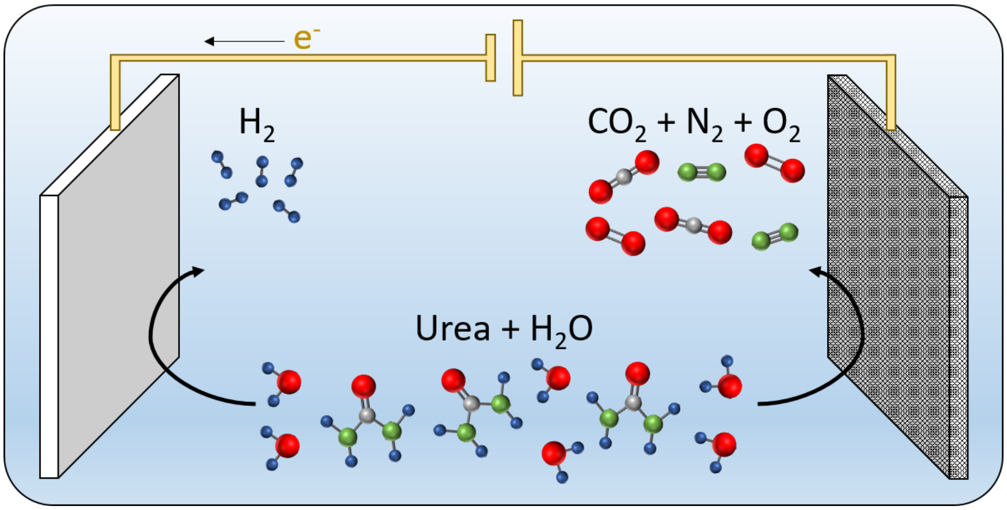

Figure 1.3: Schematic of the urea electrolysis system, where hydrogen is produced at the cathode and urea is oxidized to gaseous carbon dioxide and nitrogen at the anode.

produced, the OER is the electrochemical process causing a bottleneck towards the adoption of hydrogen power as a grid-scale ESS technology. Consequently, significantly more research has been dedicated in this work towards the OER. Additionally, urea oxidation on Ni-based materials is evaluated as an alternative to the OER. Through the use of a wide variety of electroanalytical and materials characterization techniques, the state of the electrocatalytic oxide layer formed during alkaline electrolysis is first examined. Subsequently, the stability, activity, and feasibility of Ni and Ni-based electrocatalysts towards the OER and UOR electrolytic processes are quantified and discussed. In Chapter 2, the current state of Ni-based electrocatalysis is reviewed with respect to alkaline water and urea electrolysis. Chapters 3 and 4 will discuss the development and benchmarking of nickel-chromium-molybdenum materials for the HER, OER, and UOR. In chapter 5, the use of potential cycling to control the electrocatalytic properties of the NiOOH layer is investigated. Chapter 6 examines the use of computational fluid dynamics modeling to improve mass transfer of the UOR, and finally, chapter 7 summarizes the results of these studies and provides a perspective on the research of Ni-based materials for alkaline electrochemistry.

Chapter 2

LITERATURE REVIEW

2.1 Nickel Electrocatalysis

2.1.1 Nickel (Oxy)Hydroxide Phases

Practical electrocatalysis using nickel has been studied since the late 1960s, with some of the earliest work focusing on applications for hydrogen fuel cells.[13] The earliest electrochemical characterization of nickel in alkaline conditions, however, was studied over two decades earlier. The works of Feitknecht *et al.* and Bode *et al.* were pioneering in the field of Ni electrocatalysis, first identifying the formation of nickel hydroxide ($Ni(OH)_2$) and nickel oxyhydroxide (NiOOH) phases in alkaline conditions.[14, 15] The Bode scheme, illustrated in Figure 2.1, was first introduced in 1966 and has been extensively studied by the catalyst community through electrochemical, morphological, and spectroscopic techniques.[10, 15–24]

In alkaline media, and in the potential range of 0 to 0.5 V_{RHE} (0.1 M KOH[†]), Ni metal forms NiO and the alpha-phase hydroxide, α-$Ni(OH)_2$.[25] The α-$Ni(OH)_2$ phase is described as turbostratic layers of $Ni(OH)_2$ intercalated by water molecules.[22] This phase is unstable in alkaline conditions; potentials greater than 0.5 V_{RHE} cause an irreversible transformation of α-$Ni(OH)_2$ to the beta-phase hydroxide β-$Ni(OH)_2$, the dehydrated form of α-$Ni(OH)_2$.[20] While the oxidation state of the two hydroxide phases is identical, the hydrated α-$Ni(OH)_2$ form has almost double the interlayer spacing than that of β-$Ni(OH)_2$ (8 *vs.* 4.6 Å), contributing to its instability. Due to the low potentials required for these reactions, formation of α-$Ni(OH)_2$ and subsequently β-$Ni(OH)_2$ happen spontaneously when exposed to alkaline media at open circuit potential, the rates of which depend on hydroxide concentration and

---

[†] Subsequent potentials are also reported for a 0.1 M KOH electrolyte unless specified otherwise.

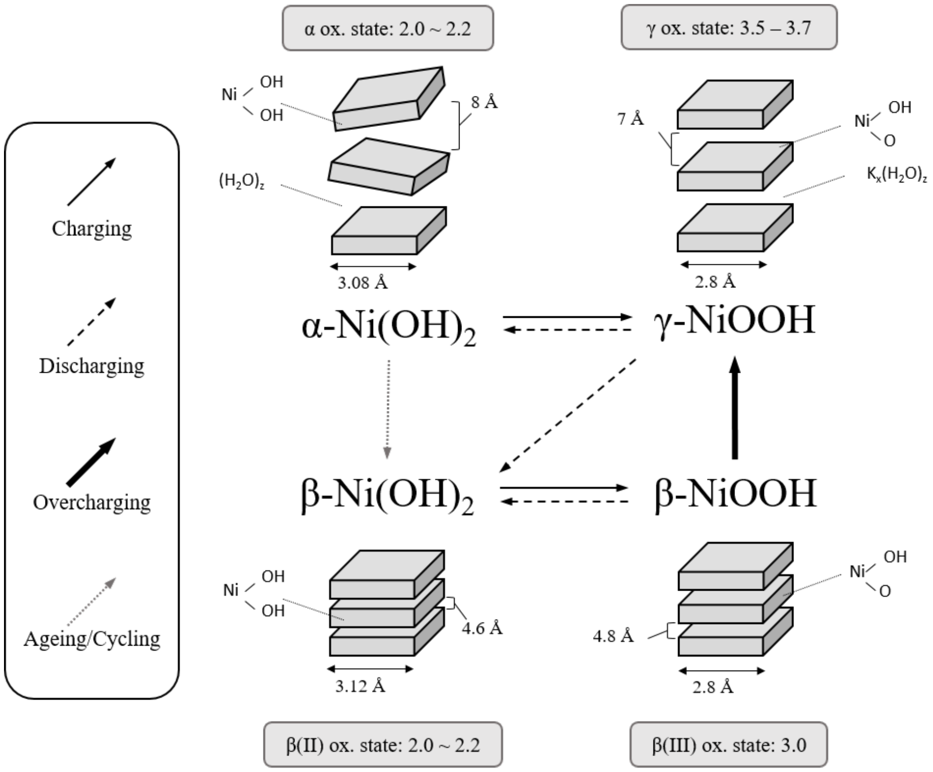

Figure 2.1: The general Bode scheme representation of the relationship between hydroxide and oxyhydroxide Ni surface states formed during the charge-discharge cycle in alkaline media. Adapted from Van der Ven *et al.*[18]

temperature. At more positive potentials greater than 1.35 V_{RHE}, β-Ni(OH)$_2$ undergoes oxidation to its oxyhydroxide state, β-NiOOH.[12, 21] The reaction for this oxidation process is often described by Equation 2.1:

$$\mathrm{Ni(OH)_2 + OH^- \rightleftharpoons NiOOH + H_2O + e^-} \tag{2.1}$$

This transformation is reversible, and β-NiOOH is easily reduced back to β-Ni(OH)$_2$. When subjected to overcharge, β-NiOOH transforms to γ-NiOOH.[22] Overcharge is loosely described as application of potentials much greater than the standard equilibrium potential (E^{o}) over prolonged periods. The value of E^{o} is reported to be 1.33 V_{RHE} for the α-Ni(OH)$_2$ to γ-NiOOH transformation and 1.36 V_{RHE} for the β-Ni(OH)$_2$ to β-NiOOH transformation.[26] One possible mechanism for the reaction is described by Equation 2.2:[18]

$$3\,\beta\text{-NiOOH} + \text{KOH} + \text{H}_2\text{O} \longrightarrow \text{H}_2\text{K}(\text{H}_2\text{O})_2\text{Ni}_3\text{O}_6 \tag{2.2}$$

The chemical formula $H_2K(H_2O)_2Ni_3O_6$ is just one of many possible forms of the γ-phase family, which is written simply as γ-NiOOH. When discharged, γ-NiOOH reduces to both α-Ni(OH)$_2$ or β-Ni(OH)$_2$.[21] Studies indicate that γ-NiOOH can also directly form from α-Ni(OH)$_2$ during the charging process due to their similar intercalated structures.[26] The structure, electrochemical properties, and stability of these phases vary considerably depending on the conditions and potential bias, and the complex pathways make electrochemical investigation of the Ni oxide layer challenging.

2.1.2 Oxygen and Hydrogen Evolution on Nickel

The hydrogen evolution reaction (HER) and the oxygen evolution reaction (OER) are the two crucial mechanisms of clean hydrogen production. The focus of this paper is alkaline water electrolysis (AWE), and as such, all water-based reactions will be written in their alkaline form. The HER — occurring at the cathode in AWE — is described overall by Equation 2.3:[10, 27]

$$2\,\text{H}_2\text{O} + 2\,\text{e}^- \longrightarrow \text{H}_2 + 2\,\text{OH}^- \tag{2.3}$$

The HER is a multistep mechanism consisting of a Volmer, Tafel, and Heyrovsky step, and the overall reaction can occur by either a Volmer-Tafel or Volmer-Heyrovsky process:[10, 27]

$$\text{Volmer}: \quad 2\,\text{H}_2\text{O} + \text{M} + 2\,\text{e}^- \longrightarrow 2\,\text{MH}_{\text{ads}} + 2\,\text{OH}^- \tag{2.4}$$

$$\text{Tafel}: \quad 2\,\text{MH}_{\text{ads}} \longrightarrow \text{H}_2 + 2\,\text{M} \tag{2.5}$$

$$\text{Heyrovsky}: \quad \text{MH}_{\text{ads}} + \text{H}_2\text{O} + \text{e}^- \longrightarrow \text{H}_2 + \text{M} + \text{OH}^- \tag{2.6}$$

The OER occurs at the anode in AWE, as described by Equation 2.7:[10, 27]

$$4\,\text{OH}^- \longrightarrow \text{O}_2 + 2\,\text{H}_2\text{O} + 4\,\text{e}^- \tag{2.7}$$

While the HER is neatly described using the Volmer, Tafel, and Heyrovsky steps above, the mechanism by which the OER occurs is dependent on the electrocatalyst and the pH of the electrolyte. Multiple possible intermediate variations have been reported, and the exact mechanism for a specific system is difficult to determine. The same two elementary steps are usually assumed to initiate the OER, as described by Equation 2.8 and Equation 2.9:[10, 27]

$$\mathrm{M + OH^- \longrightarrow MOH + e^-} \tag{2.8}$$

$$\mathrm{MOH + OH^- \longrightarrow MO + H_2O + e^-} \tag{2.9}$$

In these two steps, a hydroxide ion ($\mathrm{OH^-}$) adsorbs to a metal active site (M), forming MOH, a metal-hydroxide species. The subsequent electrochemical removal of a proton results in MO, a lone oxygen atom adsorbed on an active site. Following these initiation steps, one of two possible pathways may occur. The first is described by Equation 2.10:[10, 27]

$$\mathrm{2\,MO \longrightarrow 2\,M + O_2} \tag{2.10}$$

Here, two adsorbed oxygen atoms may combine to form an $\mathrm{O_2}$ molecule and free up two active sites. Alternatively, an additional three-step process may follow the original two elementary steps, as described by Equation 2.11, Equation 2.12, and Equation 2.13:[10, 27, 28]

$$\mathrm{MO + OH^- \longrightarrow MOOH + e^-} \tag{2.11}$$

$$\mathrm{MOOH + OH^- \longrightarrow MOO^- + H_2O} \tag{2.12}$$

$$\mathrm{MOO^- \longrightarrow M + O_2 + e^-} \tag{2.13}$$

In this mechanism, a MO species reacts with a hydroxide ion in solution to form MOOH, a metal oxyhydroxide species. Deprotonation of the oxyhydroxide species results in the formation of $\mathrm{MOO^-}$, which is subsequently oxidized to form an $\mathrm{O_2}$ molecule and the original active site. The final two steps in this mechanism are often written as a combined chemical-electrochemical step:

$$\mathrm{MOOH + OH^- \longrightarrow M + O_2 + H_2O + e^-} \tag{2.14}$$

The additional three-step mechanism is more often referenced in electrochemical studies, as many transition metals — including Ni — will often form the necessary oxyhydroxide phases for O_2 evolution to occur. [10, 27]

Oxygen evolution on Ni-based catalysts is a well-studied field, and much effort has been dedicated to increasing reaction kinetics through surface area modifications, morphological adjustments, and elemental doping.[10, 16, 24, 29–36] A commonly used method for improving the OER performance is through transition metal doping, the addition of one or more different transition metals to a Ni electrode. Iron is often incorporated, and NiFe electrodes have shown exceptional electrocatalytic activity, increased stability during the OER, and high electrochemical surface areas.[16, 37] Furthermore, Ni-based oxides have a high affinity for Fe adsorption, resulting in the formation of dynamic active sites with increased OER activity.[29] Other commonly used transition metals are cobalt and manganese.

Examples of electrocatalytic performance benchmarks include the Tafel slope, overpotential, and turnover frequency. The Tafel slope (b) is a measure of how responsive the reaction rate is to a change in applied potential. It is measured in units of millivolt-per-decade ($\mathrm{mV\,dec^{-1}}$), corresponding to the amount of potential increase that is required to increase the current response by a factor of 10. Consequently, a lower Tafel slope is desired. The overpotential required to generate 10 mA $\mathrm{cm^{-2}}$ (η_{10}) is another kinetic benchmark electrocatalysis. The value of 10 mA $\mathrm{cm^{-2}}$ is often used, as it corresponds to the approximate current density required at the anode in a 10% efficient solar water electrolysis device under 1 sun illumination.[38] As the overpotential is a measure of applied energy per charge, a lower η_{10} value corresponds to a more effective catalyst. The turnover frequency (TOF) is a measure of catalytic frequency. Measured in units of $\mathrm{s^{-1}}$, the TOF corresponds to how many times a catalytic reaction can occur (“turns”) in a given time period, and a higher value indicates a better catalyst.

Electrocatalytic benchmarks values for $Ni(OH)_2/NiOOH$ and some Ni-based materials are shown in Table 2.1. Iron is one of the most commonly used additives for Ni-based oxygen evolution; a strong electron interaction between Ni and Fe leads to a decrease in the energy

Table 2.1: Comparison of Ni-based electrocatalysts for the OER in alkaline medium. Values compared are the Tafel slope (b), overpotential (η_{10}) required to generate 10 mA cm^{-2} of OER current, and the turnover frequency (TOF).

Electrocatalyst	Ref.	b mV dec^{-1}	η_{10} (10 mA cm^{-2}) mV	TOF (300 mV) s^{-1}
Ni(OH)$_2$/NiOOH	[31, 39]	100	530	0.011
NiFe-LDH	[32]	40	302	0.05
FeNi-GO	[30]	40	220	0.38
NiCo-LDH	[32]	41	334	0.1
CoNiP	[35]	66.5	280	-
(NiCo)$_{0.85}$Se	[40]	79	255	-
NiMn-LDH	[41]	40	350	-

needed to initiate OER.[29] Moreover, doping with Fe increased the formation of active sites, improving kinetics of the OER.[39] The subsequent Tafel slope and overpotential decrease, as well as the increase in turnover frequency, can be seen in Table 2.1. Using a NiFe-LDH (layered double hydroxides) electrode decreases the Tafel slope by 60 mV dec^{-1} and the overpotential by 228 mV compared to pure Ni. Additionally, the turnover frequency of the NiFe-LDH electrode was almost 5 times that of the pure Ni electrode. The use of a FeNi-GO (graphene oxide) electrode resulted in a similar Tafel slope decrease, but also reduced the overpotential by 310 mV and increased the turnover frequency by a factor of 35. Cobalt and manganese have similar, synergistic effects with Ni, resulting in the improved OER kinetics shown in Table 2.1. Summarily, “cheap” transition metals keep the electrocatalyst cost low while improving the intrinsic activity of the electrode towards the OER.

2.2 Urea Oxidation

The earliest research on the oxidation of urea was published by NASA in the 1960s.[42] These studies were motivated by extended space flight, with research focused on reclaiming clean water from urine. Here, urea oxidation was presumed to undergo an indirect mechanism, reacting with hypochlorite in solution that forms from the oxidation of chloride ions. The hypochlorite-mediated urea decomposition process is described by the following reaction:[42]

$$\mathrm{CO(NH_2)_2 + 3\,NaOCl \longrightarrow N_2 + CO_2 + 3\,NaCl + 2\,H_2O} \tag{2.15}$$

In the 1970s, continued research revealed the presence of an alternative, direct urea oxidation reaction (direct-UOR) on a platinum electrode, as described by Equation 2.16:[43]

$$\mathrm{CO(NH_2)_2 + 6\,OH^- \longrightarrow N_2 + CO_2 + 5\,H_2O + 6\,e^-} \tag{2.16}$$

This electrochemical oxidation reaction does not rely on hypochlorite-mediation, allowing for the direct decomposition of urea-rich, chloride-free electrolytes using a noble metal catalyst. Following this development, research on additional catalysts such as ruthenium oxide (RuO_2) and iridium oxide (IrO_2) led to the determination that noble metals — while active towards the direct-UOR — had a low efficiency, forming partial decomposition products such as nitrates and nitrites.[44, 45] The high cost of noble metal catalysts and undesirable side products would hinder development of a practical direct-UOR catalyst.

It was not until 2009 that the discovery of nickel's exceptional activity towards urea oxidation resulted in a series of important new research.[12, 46, 47] Through these studies, it was determined that the NiOOH phase formed through the electrochemical oxidation of Ni in alkaline electrolyte would be reduced to the $Ni(OH)_2$ phase *by* urea, resulting in an additional pathway for urea electrolysis to occur. This indirect mechanism (indirect-UOR) is described by Equation 2.17:[47]

$$\mathrm{CO(NH_2)_2 + 6\,NiOOH + H_2O \longrightarrow N_2 + CO_2 + 6\,Ni(OH)_2} \tag{2.17}$$

When Ni is used as the electrocatalyst, both the direct and indirect mechanisms occur and NiOOH will catalyze the reaction in both cases. The direct mechanism is classified as an E_rE_i case, where a reversible electrochemical reaction ($Ni(OH)_2$ oxidation) precedes an irreversible electrochemical reaction (direct-UOR).[48] The indirect mechanism is considered an E_rC_i' case, where the same reversible $Ni(OH)_2$ oxidation precedes a catalytic chemical reaction (indirect-UOR).[48]

Following these discoveries, nickel-based urea electrocatalysts have become a subject of intense study. The addition of doping elements such as cobalt, rhodium, iron, molybdenum, and phosphides has been shown to increase the performance of urea oxidation.[49–53] The addition of these doping elements can effectively reduce the overpotential required for urea oxidation, increase the electrochemical surface area, and increase electrode stability, extending catalyst lifetime.

Transition-metal doping for the UOR has similar benefits to that of the OER: improved catalytic activity at a low cost. Incorporating cobalt during $Ni(OH)_2$ electrodeposition negatively shifts the UOR onset potential of the resulting electrocatalyst.[54] The negative shift was attributed to an overall reduction in the energy required to oxidize Ni — and subsequently urea — due to the Ni-Ci electronic interactions. Adding iron to α-$Ni(OH)_2$ nanosheets has been shown to reduce the overall charge-transfer resistance of the UOR, while including Mo into a Ni_3S_2-based electrode improves the cleavage of urea C−N bonds. The electrolyzer developed using the Mo−Ni_3S_2 electrodes was capable of producing 10 mA cm^{-2} a 70 mV smaller overpotential compared to traditional water electrolysis.[55]

The use of specialized deposition methods can significantly increase the electrochemical surface area and improve the UOR performance. By directly depositing α-$Ni(OH)_2$ on a carbon cloth substrate using a methanol-directed hydrothermal method, a multi-layered nanosheet catalyst was formed.[56] The nanosheet catalyst had a high capacitance — an equivalent measure of ECSA — of 130.2 mF cm^{-2}, and a UOR current density of 436.4 mA cm^{-2} at 0.5 $V_{Ag/AgCl}$. Cobalt electrodeposited on a Ni-foam based electrode has been shown to form a "chrysanthemum-like" catalyst structure, increasing the base electrode's electrochemical surface area by 2.4–23.4 times.[57] Depositing manganese-cobalt using a hydrothermal-calcination-hydrothermal method results in a very high ECSA and an exceptional UOR current density of 650 mA cm^{-2} in 5 M KOH and 0.33 M urea electrolyte at 0.6 $V_{Ag/AgCl}$.[58]

Recently, density functional theory (DFT) has been used to uncover the catalytic UOR mechanisms. A DFT study analyzed the elementary dissociation reactions of urea to nitrogen and carbon dioxide in the presence of NiOOH and hydroxide ions, and determined that the removal of carbon dioxide was the rate-determining step (4.3×10^{-65} s^{-1}).[59] A study on the fate of nitrogen during the UOR on Ni-based catalysts revealed that side products such as NO_2^-, N_2O, and NO_3^- were formed due to over-oxidation.[60] To combat these undesirable reactions, a polyaniline coating was designed to shift the UOR selectivity towards N_2. Additionally, DFT has been used to improve catalyst development by determining the role of catalyst structure on efficient urea oxidation. One study determined that the Ni atoms near the edge of a β-Ni(OH)$_2$ layer displayed significant UOR activity compared to atoms within the basal plane, and large β-Ni(OH)$_2$ vacancies resulted in lower urea adsorption energies.[61]

Chapter 3

ELECTROCHEMICAL TECHNIQUES

As the focus of this work is an electroanalytical study of nickel electrocatalysis, a brief description of the electrochemical techniques used throughout the paper is included. The cyclic voltammetry and staircase voltammetry sections summarize the electroanalytical methods as described by Bard *et al.*.[48] The basic theory and usage of electrochemical impedance spectroscopy is summarized as described by Orazem & Tribollet, Lacey, Pine Research, Gamry Instruments.[62–65]

3.1 Cyclic Voltammetry

Cyclic voltammetry (CV) is a potentiodynamic measurement where the potential of the working electrode is ramped over time from an initial potential (E_1) to a switching potential (E_λ) and back down to E_1, as shown in Figure 3.1(a). This is one cycle, taking t seconds to complete. The sweep rate (ν / mV s^{-1}) remains constant during each experiment but may differ between experiments. This is repeated until n cycles are completed. The current response is measured throughout and then plotted as a function of time (Figure 3.1(b)) or potential (Figure 3.1(c)). This electrochemical process is generally used qualitatively, providing information on which electrochemical processes are occurring in a particular potential range and the reversibility of a reaction.

In Figure 3.1, panels (b) and (c) show the same current response, but *vs.* time and *vs.* potential, respectively. The current *vs.* potential representation is more common, as it provides a visual representation of characteristic potentials. A pair of matching peaks in a cyclic voltammogram usually corresponds to a simple, reversible "E" redox-reaction:

$$\mathrm{O} + \mathrm{ne}^- \rightleftharpoons \mathrm{R} \tag{3.1}$$

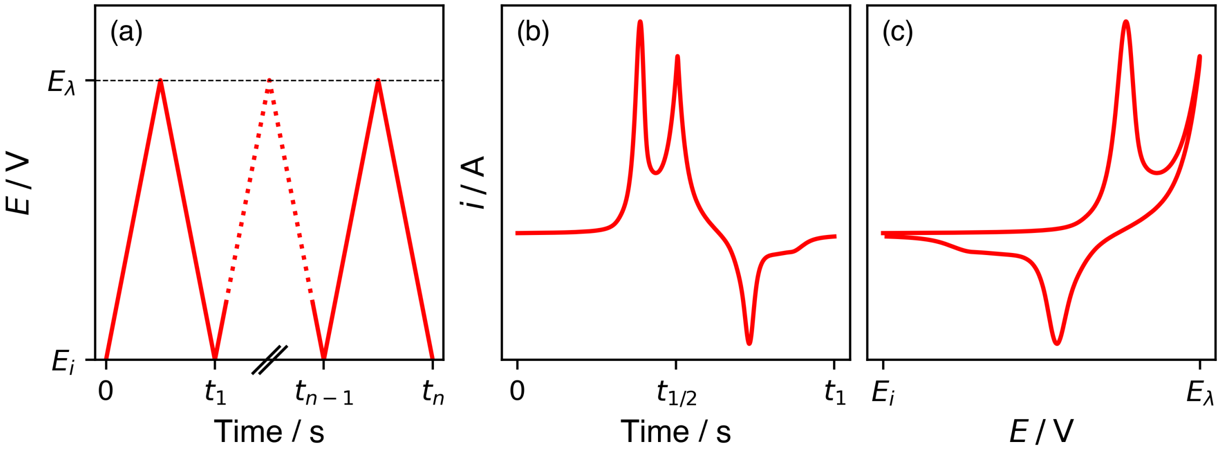

Figure 3.1: (a) A typical cyclic voltammetry experimental waveform and the corresponding (b) current-time and (c) current-potential responses.

while an unmatched peak — as seen in Figure 3.1(b) might correspond to to an irrerversible redox reaction:

$$\mathrm{O} + \mathrm{ne}^- \longrightarrow \mathrm{R} \tag{3.2}$$

A sample CV is shown in Figure 3.2, annotated with the characteristic potentials and currents of interest. In a typical scan, the potential is swept positively from an initial potential (0.2 V) to a final potential (0.7 V) and negatively back to the initial potential. Current is measured as the applied potential drives an oxidation reaction during the forward (anodic) scan. The formation of a peak appears where the rate of oxidation is at its highest. The current at this point is referred to as the anodic peak current, $i_{\mathrm{p,a}}$, and it occurs at the anodic peak potential, $E_{\mathrm{p,a}}$. During the reverse (cathodic) scan from 0.7 V back to 0.2 V, the rate of reduction is at its highest at the cathodic peak potential, $E_{\mathrm{p,c}}$, and the current measured here is the anodic peak current, $i_{\mathrm{p,c}}$. The potential directly in the middle of $E_{\mathrm{p,a}}$ and $E_{\mathrm{p,c}}$ is referred to as the half-wave potential, $E_{1/2}$, and is generally a good estimate for the standard equilibrium potential of a reversible or quasi-reversible redox reaction.[66] The difference between $E_{\mathrm{p,a}}$ and $E_{\mathrm{p,c}}$ is called the peak-to-peak separation, ΔE_{p}, and combined with the

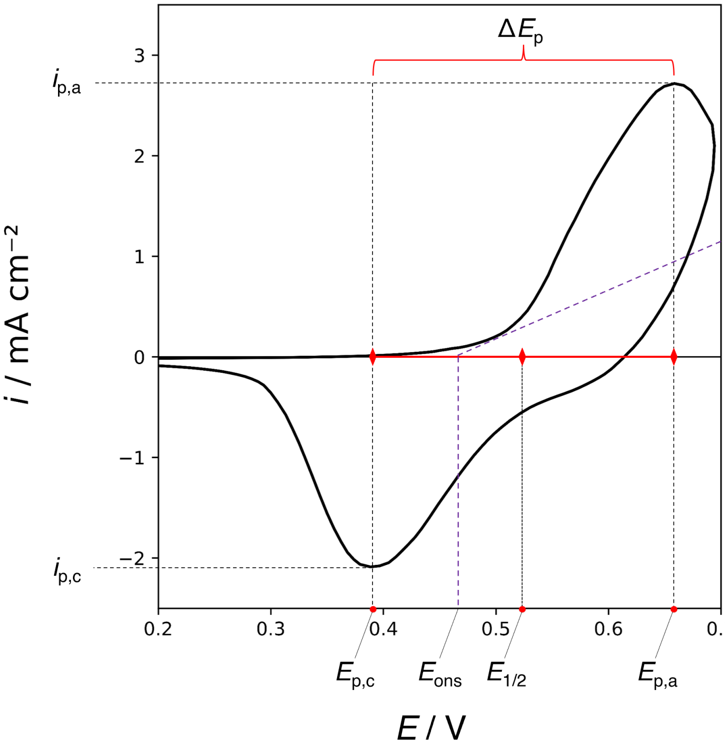

Figure 3.2: A sample cyclic voltammogram between 0.2 V and 0.7 V with characteristic potentials and currents.

half-wave potential, acts as an indicator for the magnitude of oxidation and reduction overpotentials. Finally, the onset potential (E_{ons}) is estimated by drawing a tangent down from the rising current of a wave. This value roughly corresponds to the “initiation point” of an electrochemical process, or the minimum potential required for an electrochemical reaction to occur.

3.2 Staircase Voltammetry

Staircase voltammetry (SV) is a type of potentiostatic voltammetry, where — like CV — the potential of the working electrode is ramped over time. In this case, however, discrete potential steps are each held for a time t, as shown in Figure 3.3(a). Holding at a set potential

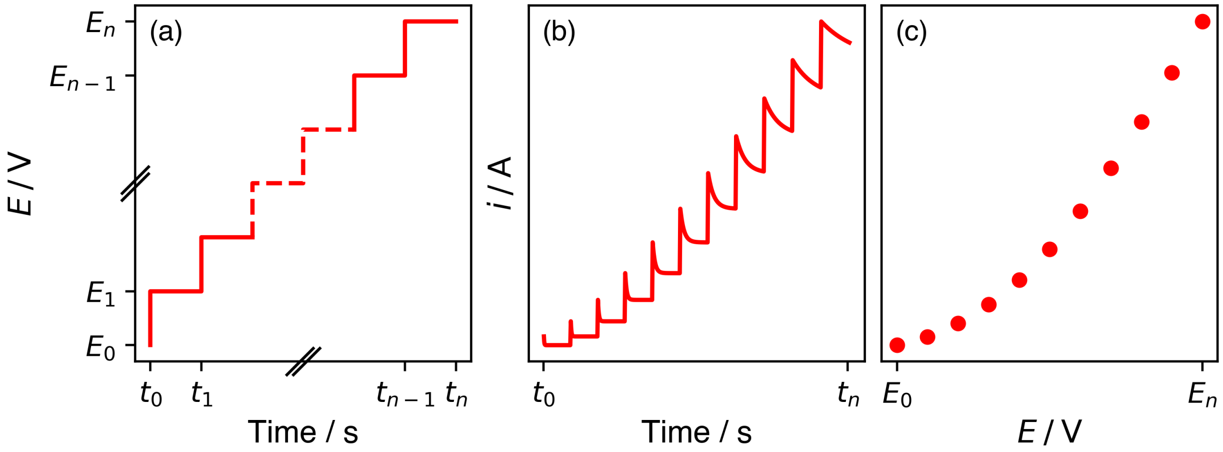

Figure 3.3: (a) A typical staircase voltammetry experimental waveform, the corresponding (b) current-time response, and (c) a polarization curve constructed from the data in (b).

allows for a concentration gradient to form near the electrode surface, causing the current to decay until a steady-state reaction rate is realized (Figure 3.3(b)). Generally, the current decays according to the Cottrell equation:

$$i = \frac{nFAc_{\mathrm{i}}^{0}\sqrt{D_{\mathrm{i}}}}{\sqrt{\pi t}} \tag{3.3}$$

where n is the number of electrons exchanged, F is the Faraday constant, A is the geometric area of the electrode, c_{i}^{0} is the initial concentration of the oxidized/reduced species (i), D_{i} is the diffusion coefficient of species i, and t is time. The Cottrell equation is often used in conjunction with staircase voltammetry to evaluate the diffusion coefficient of a chemical species.

The current may not decay to a complete steady state due to the time scales in which some electrochemical processes occur, and in these cases, a hold of at least 15 minutes is generally considered sufficient for a practical steady state. Multiple steps may be conducted, resulting in a current-time response like the one seen in Figure 3.3(b). The steady state current value for each step can be evaluated and plotted *vs.* the potential used for each step, resulting in a current-potential plot as seen in Figure 3.3(c). This type of polarization data is used to evaluate the Tafel slope, turnover frequency, and other benchmarks for electrochemical reaction kinetics.

A Tafel plot — as shown in Figure 3.4 — is an alternate representation of the polarization curve shown in Figure 3.3(c). Here, the half-cell potential is converted to an overpotential by subtracting the standard equilibrium potential of the reaction being examined:

$$\eta = E - E^o \tag{3.4}$$

Consequently, the overpotential is reference-agnostic and plotted on the y-axis. The log of current (or current density) is plotted on the x-axis, resulting in a plot of η *vs.* $\log(i)$. The slope of this curve has units of mV-per-decade, and is often referred to as a Tafel slope (b / $\mathrm{mV\,dec^{-1}}$). Mathematically, the Tafel equation is as follows:

$$\eta = \pm b \cdot \log_{10}(i) \tag{3.5}$$

The Tafel equation is a simplification of the Butler-Volmer equation under the assumption that $\eta > 0.1\mathrm{V}$ and that the concentration of reactant at the surface of the electrode is sufficiently high such that the system is not limited by the mass transfer rate. In other

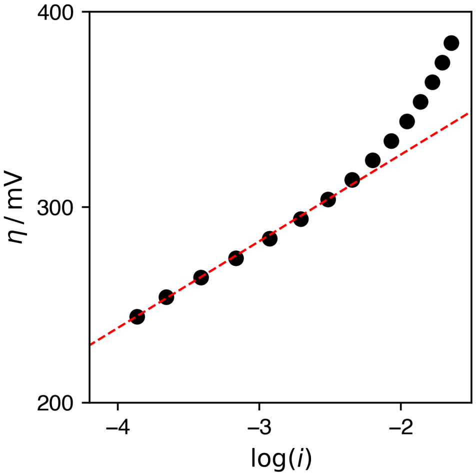

Figure 3.4: An example Tafel plot with a Tafel slope fit using the low overpotential range.

words, the Tafel equation is valid for a kinetically limited system at a sufficiently high overpotential. Consequently, the Tafel slope is often used as a kinetic benchmark, and measures how responsive the reaction rate is to a change in applied potential, i.e. a low Tafel slope corresponds to a system with faster kinetics.

3.3 Electrochemical Impedance Spectroscopy

Electrochemical impedance spectroscopy (EIS) is an electroanalytical technique that uses a sinusoidal input to probe the electrochemical response of a system, as shown in Figure 3.5. While EIS can be conducted potentiostatically or galvanostatically, only potentiostatic EIS is used and discussed in this work.

During a typical EIS experiment, a sinusoidal potential is applied to an electrochemical system and the resulting current is measured. The time-dependent expressions for potential

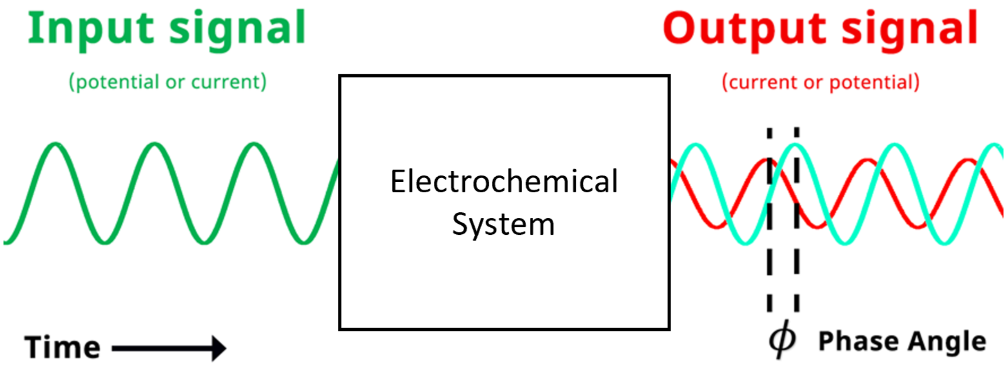

Figure 3.5: A typical EIS experiment flow, where a sinusoidal potential or current is applied to an electrochemical system, the resulting current or potential is measured, an FFT is applied, and a Nyquist plot constructed from the impedance data. Figure from *Pine Research*.[64]

and current are described by:

$$E(t) = E_\mathrm{o}\sin(\omega t) \tag{3.6}$$

$$i(t) = i_\mathrm{o}\sin(\omega t + \phi) \tag{3.7}$$

where E_o and i_o are the potential (V) and current (A) wave amplitudes, respectively, ω is the angular frequency (rad s^{-1}), t is time (s), and ϕ is the phase shift (rad). Both the potential amplitude and frequency are controlled, and the output current signal may be shifted by a finite amount (ϕ). The phase shift is due to electrical reactance, an opposition to alternating current caused by a system's inductance or capacitance. This process is repeated several times, with the frequency of the varying between each experiment. In this work, the frequency is evenly spaced on a log scale, descending from ∼1 MHz to ∼0.1 Hz. The impedance of the system (Z) can be expressed using an equation analogous to Ohm's Law:

$$Z = \frac{E(t)}{i(t)} = \frac{E_0\sin(\omega t)}{i_0\sin(\omega t + \phi)} = Z_\mathrm{o}\frac{\sin(\omega t)}{\sin(\omega t + \phi)} \tag{3.8}$$

Using Euler's formula:

$$\exp(j\phi) = cos(\phi) + j\sin(\phi) \tag{3.9}$$

where j is the imaginary unit, the potential and current time responses can be expressed as complex functions:

$$E(t) = E_\mathrm{o}\exp(j\omega t) \tag{3.10}$$

$$i(t) = i_\mathrm{o}\exp(j\omega t - \phi) \tag{3.11}$$

allowing for impedance to be represented as a complex number:

$$Z(\omega) = \frac{E(t)}{i(t)} = Z_0\exp(j\phi) = Z_0[\cos(\phi) + j\sin(\phi)] \tag{3.12}$$

The impedance is often split into a real (Z_r) and imaginary (Z_i) impedance:

$$Z(\omega) = Z_0[\cos(\phi) + j\sin(\phi)] = Z_0\cos(\phi) + Z_0 j\sin(\phi) = Z_\mathrm{r} + jZ_\mathrm{i} \tag{3.13}$$

A Nyquist plot is a graphical representation of impedance data — where each data point corresponds to Equation 3.13 evaluated at a different frequency value — generally plotted as $-Z_\mathrm{i}$ *vs.* Z_r. The former term is the reactive portion of impedance, while the latter is the resistive portion. Each feature on a Nyquist plot has a defining shape, width, and characteristic frequency, and quantitative characteristics about the electrochemical system can be extracted from these features.

The electrochemical systems in this work can be described simply using resistors and capacitors. A resistor — which obeys Ohm's law — is always proportional to the voltage. There is no reactive part (phase shift) and therefore no dependency on the frequency. Consequently, the impedance of a resistor (Z_R) is simply equal to its resistance (R):

$$Z_\mathrm{R} = R \tag{3.14}$$

A capacitor, conversely, is purely reactive. An electrode-electrolyte interface acts as a capacitor, which opposes changes in the flow of charge. Consequently, as $\omega \to 0$, $Z_\mathrm{C} \to \infty$. In other words, frequency and capacitive impedance have an inversely proportional relationship:

$$Z_\mathrm{C} = \frac{1}{j\omega C} \tag{3.15}$$

where C is the capacitance. An RC circuit — consisting of a resistor and capacitor — can either be in series or in parallel. Impedance circuits follow the same additive rules as traditional circuits, leading to the following relationships:

$$\text{Series:} \quad Z_\mathrm{RC} = Z_\mathrm{R} + Z_\mathrm{C} = R + \frac{1}{j\omega C} \tag{3.16}$$

$$\text{Parallel:} \quad \frac{1}{Z_\mathrm{RC}} = \frac{1}{Z_\mathrm{R}} + \frac{1}{Z_\mathrm{C}} = \frac{1}{R} + j\omega C \therefore Z_\mathrm{RC} = \frac{R}{1 + j\omega RC} \tag{3.17}$$

For a series relationship, the capacitive impedance element is simply shifted along the real axis by a resistance R. In a parallel relationship, it can be seen that as the frequency goes to zero, the capacitive impedance term ($j\omega RC$) also goes to zero, and the circuit behaves like a resistor. As the frequency goes to infinity, however, the impedance trends towards 0. The resulting circuit element takes on the form of a semicircle with a diameter R. In EIS, a semicircle generally corresponds to a charge transfer process and is a good indicator of the type of electrochemical process occurring in the system. In many actual electrochemical systems, however, capacitors behave imperfectly due to rough surfaces, multiple reaction rates, non-uniform current distributions, etc. To account for this, a circuit element called the constant phase element (CPE, Q) is often used:

$$Z_{\mathrm{Q}} = \frac{1}{Q_{\mathrm{o}}(j\omega)^{n}} \tag{3.18}$$

where Q_{o} is a pseudo-capacitance (S s^{n}) and n is an exponent between 0 and 1, where a value of $n = 1$ would represent an ideal capacitor. The exponent n deviating from 1 results in a "depressed" semicircle, and the corresponding effective capacitance (C_{eff}) can be estimated from a CPE using the equation:

$$C_{\mathrm{eff}} = \frac{(Q_{\mathrm{o}}R)^{\frac{1}{n}}}{R} \tag{3.19}$$

To extract useful electrochemical system parameters from complex EIS data, an equivalent circuit model is developed to describe the system accurately. Each element in the circuit corresponds to a physical aspect of the electrochemical system. A resistor may correspond to the electrolyte providing a resistance to ionic charge transfer, while the electrochemical double-layer can be represented by a simple RC circuit element. In this work, a simplified Randles circuit is used to describe the electrochemical reactions occurring at the electrode surface, and is shown in Figure 3.6(left).

In this system, the Ohmic resistance (R_{s}) is the sum of all ionic and electrical resistances between the potentiostat and the electrodes. As the electrolyte generally makes up the majority of this term, the Ohmic resistance is often called the ionic, solution, or electrolyte resistance. Due to the electrode-electrolyte interface, a capacitive element is included to represent the double layer capacitance. In this work, a CPE is used. When a Faradaic reaction such as the OER is also occurring at the electrode-electrolyte interface, it is described using a charge-transfer resistance (R_{ct}) in parallel with the double-layer capacitance. The parallel RC circuit has a diameter of R_{ct} and is shifted positively along the Z_{r} axis by R_{s}, as shown in Figure 3.6(right).

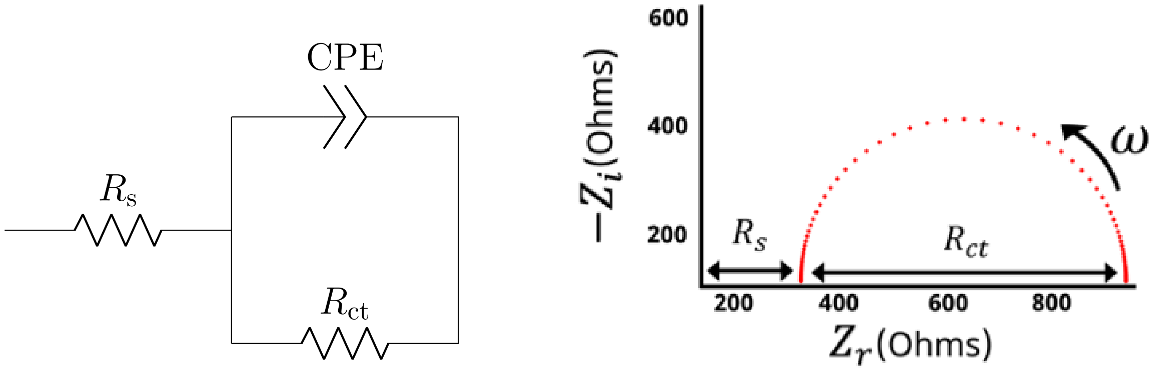

Figure 3.6: (left) The simplified Randles circuit and its (right) corresponding characteristic Nyquist plot. Figure from *Pine Research.*[64]

The Randles circuit is fit to the experimental EIS data using software or other programs. In this work, `impedance.py` — a Python package developed by Murbach, Gerwe, Dawson-Elli & Tsui — is used for equivalent circuit fitting.[67] From the circuit fit, values of R_s, Q_o, n, R_{ct}, and C_{eff} can be estimated and analyzed.

3.4 Electrochemical Surface Area

In this work, the electrochemical surface area (ECSA) was estimated using the "Capacitance", "Beta", or "Impedance" method, as described by Cossar *et al.* and Orazem & Tribollet[62, 68] The "Beta" method will subsequently be referred to as the "Reduction" method to more appropriately describe its use here.

3.4.1 The "Capacitance" Method

In the capacitance method, the electrode is cycled around its open circuit potential (OCP) in a small window (±50 mV) at a series of scan rates (ν / mV s^{-1}), as shown in Figure 3.7(a). For each scan rate, a charging current (i_{ch} / μA) can be measured. The charging current corresponds to the anodic or cathodic current value at the open circuit potential. Here, the anodic charging current is evaluated for each scan rate, resulting in a plot of i_{ch} *vs.* ν, as shown in Figure 3.7(b)

The slope of this line has equivalent units of $\mathrm{A\,s\,V^{-1}}$, equal to a capacitance (F). This value is used as an estimate of the double-layer capacitance (C_{dl}), and can be converted to an estimated ECSA by dividing by the specific capacitance (q):

$$\mathrm{ECSA} = \frac{C_{\mathrm{dl}}}{q} \tag{3.20}$$

The specific capacitance is a material property, and is approximated as 40 μF cm^{-2} for pure Ni.[68] This value is used for all Ni-based electrodes examined in this study due to their high Ni content, and consequently, the calculated ECSA is considered an estimated value.

3.4.2 The "Reduction" Method

In the reduction method, the electrochemical surface area is estimated by calculating the amount of charge passed during the reduction of NiOOH. During the reverse sweep of a cyclic voltammogram, the point where the current crosses the $i = 0$ axis — and becomes reducing current — is designated t_1. The end of the sweep is designated t_2, and these two

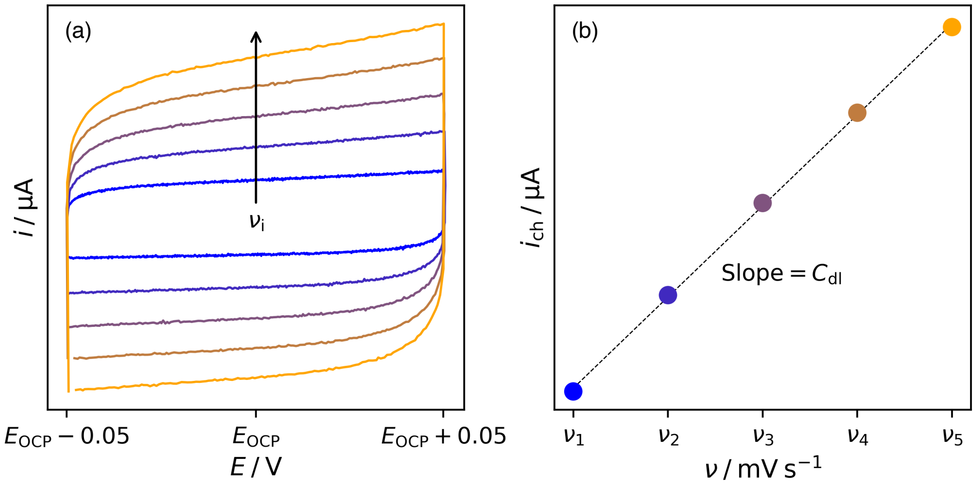

Figure 3.7: Example electrochemical surface area estimation plot, where (a) shows the OCP-cycling at different scan rates, and (b) shows the plot of charging current *vs.* scan rate.

points are shown in Figure 3.8(a). The area between the current response and the $i = 0$ axis is designated the "reduction area". By plotting the same data in its current-time format (Figure 3.8(b)), the reduction area can be seen between the x-axis bounds of t_1 and t_2. Integrating this region results in evaluation of the reduction charge (q_r / C):

$$q_\mathrm{r} = -\int_{t_1}^{t_2} i \, dt \tag{3.21}$$

This reduction charge corresponds to one monolayer of the OER-active NiOOH surface, and is proportional to the ECSA.[68] The ECSA can then be calculated for a NiOOH surface by using the equation:

$$\mathrm{ECSA} = \frac{q_\mathrm{r} N_A}{nF\Gamma} \tag{3.22}$$

where N_A is the Avogadro number (mol^{-1}), n is the number of electrons exchanged during the oxidation of Ni(OH)$_2$ to NiOOH (taken to be 1 mol$_{e^-}$ mol^{-1}), F is the Faraday constant (C mol$_{e^-}$), and Γ is the average NiOOH site density (cm^{-2}) calculated using lattice constants.[69] A Γ value of 5.743×10^{14} cm^{-2} was calculated using a lattice constant of 0.283 nm.

When evaluating electrochemical reaction kinetics, a variation of ECSA is used; before

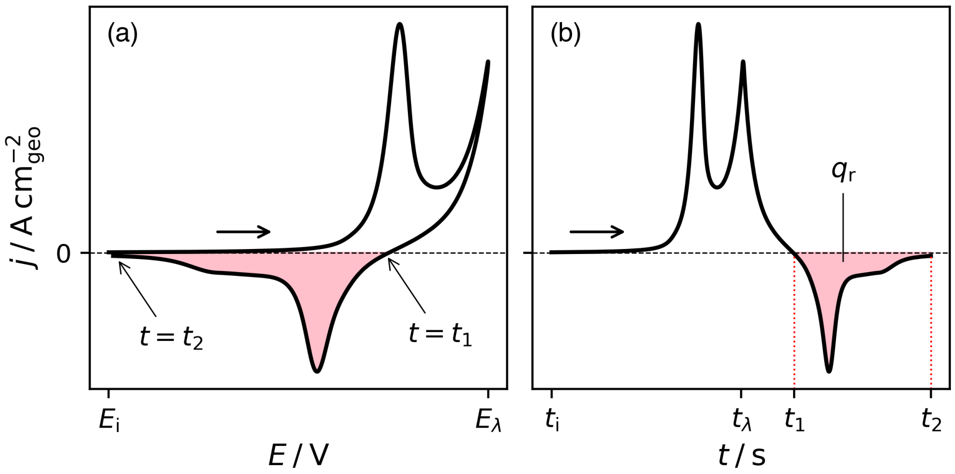

Figure 3.8: Example (a) current-potential and (b) current-time plots, highlighting the evaluated reduction area.

integrating the reduction area, the current is normalized by the geometric surface area (A / cm^2). As a result, the integration results in a reduction charge density (σ_r / C cm^{-2}):

$$\sigma_\mathrm{r} = -\int_{t_1}^{t_2} j \, dt \tag{3.23}$$

The reduction site density (Γ_r / cm^{-2}) is then evaluated using the elementary charge (e / C):

$$\Gamma_\mathrm{r} = \frac{\sigma_\mathrm{r}}{e} \tag{3.24}$$

3.4.3 The "Impedance" Method

In the impedance method, the effective capacitance is first estimated using EIS as previously described. The capacitance — along with the often-used value of specific capacitance (q) for pure Ni (40 μF cm^{-2}) — can be used to estimate the electrochemical surface area through the following equation:[68]

$$\mathrm{ECSA} = \frac{C_\mathrm{eff}}{q} \tag{3.25}$$

Chapter 4

ELECTROCHEMICAL OXIDE DEVELOPMENT OF NICKEL-CHROMIUM-MOLYBDENUM ALLOYS

4.1 Motivation

While nickel has desirable electrocatalytic properties, catalyst stability is of primary concern for practical applications. Pure Ni is prone to crevice corrosion attacks in chloride-containing environments, even in the presence of significant KOH concentrations.[70–72] Chloride ions destroy the $NiO/Ni_3O_4/NiO_2$ passive film at a pitting potential E_{pit}, the value of which decreases with increasing chloride concentration.[72, 73] Studies on Ni-passivity have shown that local breaks and defects in the oxide film provide sites for film breakdown; aggressive chloride ions hinder repassivation at these local sites, the formation of which occurs during the $Ni(OH)_2$ to NiOOH transformation.[74]

Nickel-chromium-molybdenum (NiCrMo) is an attractive alternative to pure nickel electrocatalysts in unfavorable (chloride-containing) electrolyte conditions and they are among the most versatile materials for a wide range of chemical and physical processes including marine environments, chlorination plants, and desulfurization processes.[70, 71, 75, 76] Chromium and molybdenum are added to Ni to improve its degradation resistance through the formation of Cr(III), Mo(IV), and Mo(VI) surface oxide layers.[77, 78] This passive film formation leads to improved breakdown potential and stability in corrosive environments.[77] A study on the role of Cr and Mo during repassivation in chloride-containing solutions showed

---

This is an adapted manuscript version of an article accepted for publication in *The Journal of The Electrochemical Society.* IOP Publishing Ltd is not responsible for any errors or omissions in this version of the manuscript or any version derived from it. The Version of Record is available online at [10.1149/1945-7111/acd7a6].

that oxidizing a NiCrMo alloy would initially break down the Cr(III) barrier layer.[79] After returning to the passive region, the formation of a new passive oxide — with greatly improved corrosion resistance — would occur. For a high Cr:Mo alloy, this improvement was attributed to the reformation of the Cr(III) layer, while an accumulation of Mo(VI) had also occurred for the low Cr:Mo alloy. Consequently, it is clear that the amount of alloying Cr and Mo influences the type of oxide layer that forms.

In addition to their passivating properties, chromium and molybdenum modifiers for Ni-based electrodes have been shown to affect its electrocatalytic properties; NiCr alloys in alkaline electrolyte show improved toward the oxygen evolution reaction [80] and the urea oxidation reaction [81]. The addition of molybdenum to this mix has resulted in electrodes showing promise for both the hydrogen evolution reaction and the oxygen evolution reaction.[82–84] While these preliminary studies have shown that NiCrMo materials are active towards the hydrogen, oxygen, and urea evolution reactions, a firm understanding of their surface oxide has not been established. The presence of Cr and Mo — as well as the range of applied bias — can shift the preferential formation of particular (oxy)hydroxide phases, further complicating the redox pathways presented in the Bode scheme.[85, 86]

In this chapter, cyclic voltammetry is used to elucidate the contributions of Cr and Mo — as expressed in the commercial alloys G35, B3, and C276 — to the development of NiOOH electrocatalyst phases on NiCrMo alloys. The use of commercial alloys was motivated by their potential to serve as reference materials for studies of alkaline electrocatalysis, since their preparation is standardized by the manufacturer and is therefore independent of sample preparation protocols specific to a particular laboratory. Commercial HASTELLOY® alloys with high Cr:Mo (G35), low Cr:Mo (B3), and equal Cr:Mo (C276) ratios were supplied by Haynes International.[87]

4.2 Experimental

4.2.1 Electrode Preparation

Working electrodes were made from alloys G35, B3, and C276, as well as Ni foil (0.254 mm thickness, 99.5% in purity; Alfa Aesar). The three Ni alloys were provided by Haynes International with nominal compositions shown in Table 4.1. Before electrochemical studies, the electrodes were cut to size (1 cm × 1 cm, ca. 2.5 cm^2 total geometric area) using a rotary tool (Dremel 200), followed by mechanical sanding (Buehler Ecomet III). Silicon-carbide sandpaper grits of 400, 600, 800, 1500, 3000, and 5000 were used sequentially, resulting in a smooth surface. A felt-tipped Dremel attachment and polishing compound was then used to buff the surface and remove any remaining blemishes. Finally, the electrodes were hand-polished using 1, 0.5, and 0.3 micron alumina suspension. The electrodes were sonicated in ethanol and deionized water (Millipore-Q water system) for 10 minutes each between each of the sanding and polishing steps. The resulting surfaces had a mirror finish that improved the quality of electrochemical measurements. The counter electrode was a Pt coil (ca. 5 cm^2,

Table 4.1: Nominal compositions (wt.%) for three Ni-based alloys.[87] Elements less than 1% for all alloys were excluded. Italicized elements are listed with their maximum concentrations.

	G35	B3	C276
Ni	58	65	57
Cr	33.2	1.5	16
Mo	8.1	28.5	16
W	0.6	3	4
Co	1	3	2.5
Fe	2	1.5	5
Mn	0.5	3	1

99.99% in purity; Pine Electrochemistry), which was also sonicated in ethanol and DI water for 10 minutes each before submersion in the electrochemical cell. An uncalibrated, single junction mercury oxide (Hg/HgO) reference electrode (4 M KOH, Pine Electrochemistry) was used due to the strong alkaline electrolyte. Subsequent unlabeled half-cell potentials will be reported with respect to the reversible hydrogen reference electrode (RHE), calculated using the following equation:

$$E_{\mathrm{RHE}} = E_{\mathrm{Hg/HgO}} + (0.059)\mathrm{pH} + E^{\ominus}_{\mathrm{Hg/HgO}} \tag{4.1}$$

where $E^{\ominus}_{\mathrm{Hg/HgO}}$ is the standard potential of the mercury oxide reference electrode, taken to be +0.098 V *vs.* the normal hydrogen electrode for a 20% KOH solution at 25°C. [88]

4.2.2 Electrochemical Cell

Aqueous KOH solution was used as the electrolyte for all electrochemical experiments and was prepared using KOH pellets (Fisher Scientific) in DI water ($0.04\,\mu\,\mathrm{S\,cm^{-1}}$). A 0.1 M KOH (pH 13) electrolyte was pre-electrolyzed at –0.54 $\mathrm{V_{RHE}}$ for 1 hour using two Pt electrodes to minimize solution impurities.[89] Argon or nitrogen gas was then sparged through the electrolyte for 20 minutes before each experiment to displace dissolved oxygen and create an inert environment inside the three-electrode cell (Pine Electrochemistry, 150 mL). Studies were conducted in a stagnant electrolyte, and the temperature of the cell was set to 25°C and controlled using a water bath and hot plate (Fisher Scientific), as shown in Figure 4.1.[89]

4.2.3 Oxide Development

A description of the electrochemical techniques used is provided in Chapter 3. Electrochemical experiments were carried out using a Solartron SI 1287 potentiostat and CorrWare® for data acquisition. Once the polishing procedure and electrolyte preparation were completed, the electrode was submerged in 0.1 M KOH and subjected to a reducing potential of –0.54 $\mathrm{V_{RHE}}$ to remove residual oxides and surface contaminants. An electrode in this state is referred to as having an undeveloped oxide layer (UOL). To form an oxide layer, cyclic

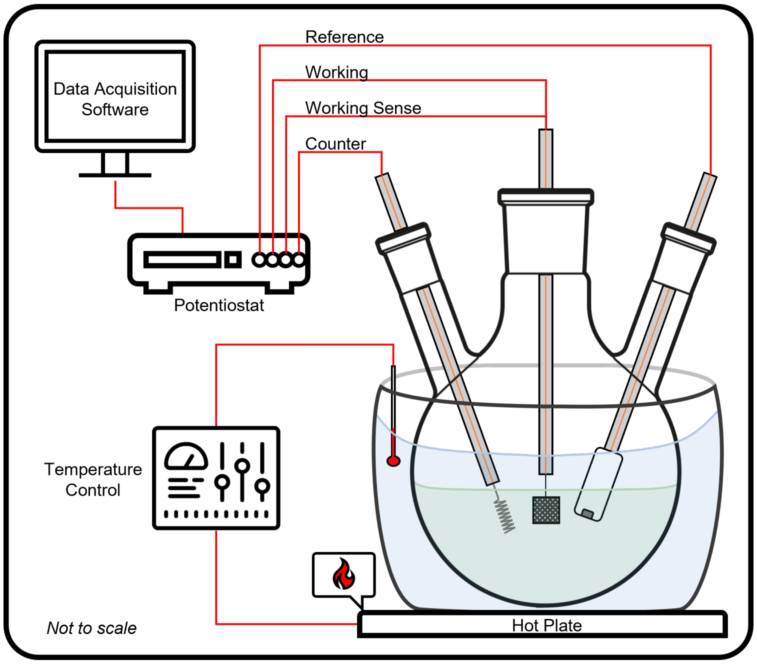

Figure 4.1: Experimental setup including the three electrode cell, working, counter, and reference electrode positions, data acquisition, and temperature control.

voltammograms (CV) were collected by scanning between 0.85 and 1.52 V_{RHE} at 50 mV s^{-1}, 50 times, followed by three scans in the same potential range at 1 mV s^{-1}. After this third scan, the electrode was allowed to discharge until the open circuit potential stabilized ($\sim$ 30 minutes), and the electrochemical surface area procedure was conducted as described in Chapter 3. A single block of scans is summarized as:

1. CV: 0.85–1.52 V_{RHE}, 50 mV s^{-1}, x50
2. CV: 0.85–1.52 V_{RHE}, 1 mV s^{-1}, x3
3. ECSA measurement

This block of scans was repeated 14 times for a total of 700 fast scans, 42 slow scans, and 14 ECSA measurements, leading to a developed oxide layer (DOL).

4.2.4 X-ray Photoelectron Spectroscopy

X-ray photoelectron spectroscopy (XPS) was conducted using a Kratos AXIS Ultra DLD. Samples were removed from the electrochemical cell and stored in DI water before XPS characterization to minimize air exposure. An undeveloped oxide layer was established after submerging an electrode in alkaline electrolyte for 3 hours in order for a hydroxide layer to form. This was done to ensure an undeveloped electrode would have a similar structure to that of a developed electrode before cycling.

4.3 Results

4.3.1 Oxide Layer Development

Figure 4.2 presents the CV profiles obtained at 1 mV s^{-1} and 25 °C in 0.1 M KOH electrolyte during the oxide development procedure for Ni, G35, C276, and B3. The voltammograms are the last scan from each block, as described in the experimental section. The first and final blocks are indicated by blue and orange curves, respectively, while the gray curves show progression of the CV profiles between the first and final blocks. Due to the slow scan rate used, the amount of charging current is minimal, and the measured current can be attributed to Faradaic processes occurring at the electrode-electrolyte interface. To verify this assumption, a calculation of charging current was conducted using the following equation:[48]

$$i_\mathrm{c} = AC_\mathrm{dl}\nu \tag{4.2}$$

In Equation 4.2, A is the geometric surface area of the electrode (2.5 cm^2), C_dl the double layer capacitance (40 μF cm^{-2})[68], and ν the scan rate (1 mV s^{-1}). This gives an i_c value of 0.1 μA, judged insignificant compared to the total measured current.

The behavior of pure Ni (Figure 4.2a) has a single anodic (forward) peak at 1.43 V (A_1^*). This peak is generally attributed to the electrochemical transformation of β-$\mathrm{Ni(OH)_2}$ to β-NiOOH and is present for all electrodes.[18, 20] A rise in current at more positive potentials ($\sim$ 1.45) V marks the start of the OER. During the cathodic (reverse) scan, a cathodic peak

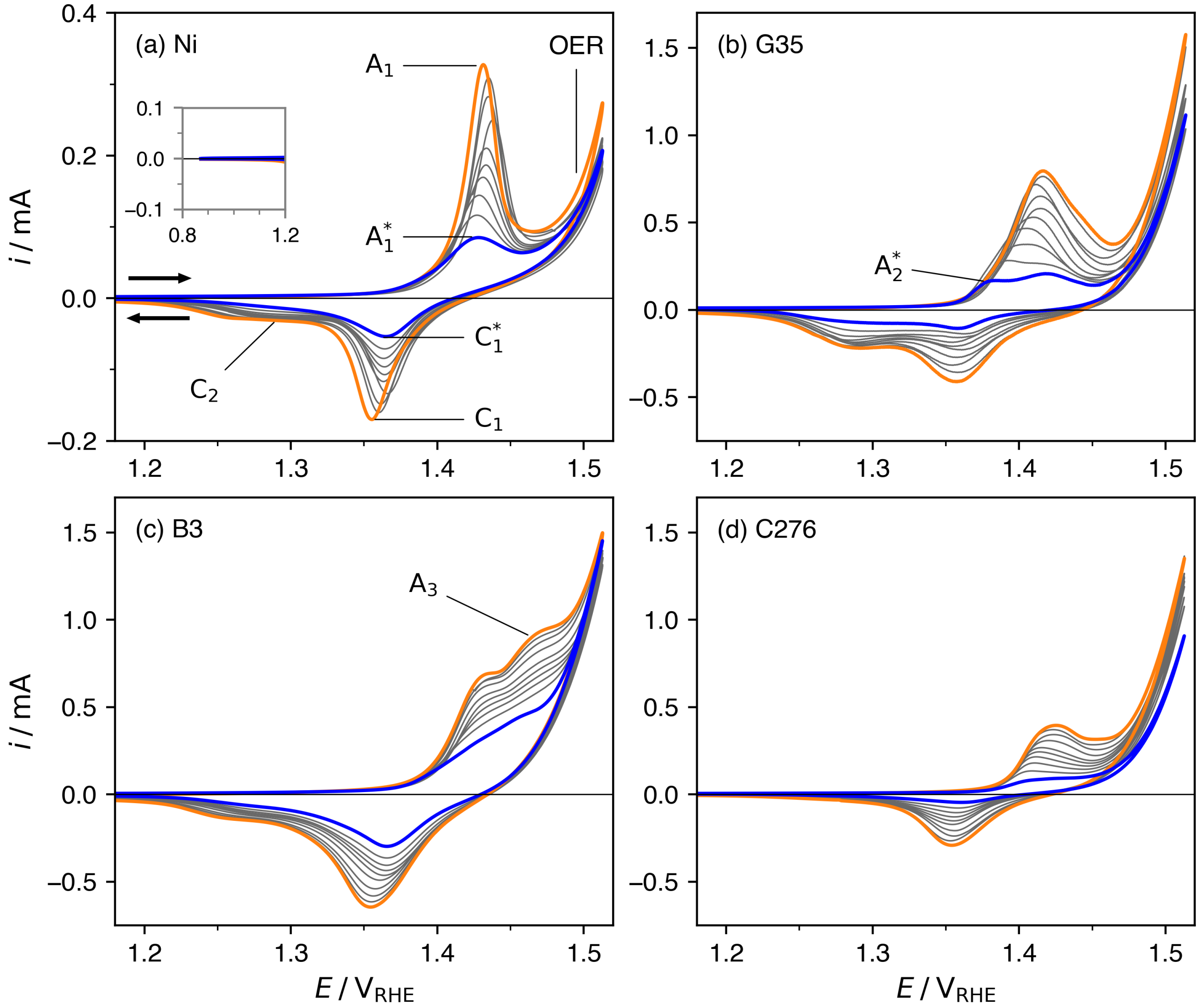

Figure 4.2: Cyclic voltammograms of oxide layer development procedure for (a) pure Ni, alloys (b) G35 (high Cr:Mo), (c) B3 (low Cr:Mo), and (d) C276 (equal Cr:Mo). The first block (blue) is always the smallest voltammogram, while the final block (orange) is the largest. The unlabeled blocks are 2, 3, 4, 5, 6, 8, 10, and 12, and progressively increase. Each block consists of 50 scans at 50 mV s^{-1} and 3 scans at 1 mV s^{-1}, and the third scan at 1 mV s^{-1} is shown. The electrolyte was an unstirred, 0.1M KOH solution held at 25 °C. The inset in (a) shows the current response in the potential range of 0.85–1.2 V.

at 1.36 V (C_1^*) signals the electrochemical reduction of β-NiOOH to β-Ni(OH)$_2$. Throughout the oxide development process, the peak and shoulder potentials for peaks A_1 and C_1 stay relatively constant, while the peak amplitude increases. After development, a wide, trailing shoulder between 1.32 and 1.22 V (C_2^*) of the cathodic scan signals the reduction of γ-NiOOH to β-Ni(OH)$_2$ or α-Ni(OH)$_2$.[17, 85]

Alloy G35 (Figure 4.2b) initially has two conjoined peaks at 1.38 V (A_2^*)and 1.42 V in the anodic scan. The peak at 1.42 V matches that of the β-Ni(OH)$_2$ to β-NiOOH transition seen in pure Ni.[90] As the scans progress and the oxide layer develops, the β-Ni(OH)$_2$ to β-NiOOH peak at 1.42 V becomes the dominant voltammogram feature, fully enveloping the smaller peak by block 6. During the reverse scan, a clear reduction peak (β-NiOOH $\rightarrow$ β-Ni(OH)$_2$) with an $E_{\text{p,c}}$ of 1.36 V and trailing shoulder (γ-NiOOH $\rightarrow$ β-Ni(OH)$_2$ or α-Ni(OH)$_2$) are initially evident. After oxide development, the shoulder has grown into a new peak with a $E_{\text{p,c}}$ of 1.29 V, while the β-NiOOH $\rightarrow$ β-Ni(OH)$_2$ peak potential remains constant at 1.36 V.

Alloy B3 (Figure 4.2c) initially has no discernible peak during the forward scan, but rather a broad shoulder (1.41–1.47 V) on the leading edge of the OER curve. The shape of the reduction curve is initially similar to that of pure Ni, with a $E_{\text{p,c}}$ of 1.37 V and a broad, trailing tail. During oxide development, the forward scan separates into two distinct shoulders on the leading edge of the OER curve that plateau near E = 1.43 and 1.47 V (A_3). Due to the significant overlap of these peaks with each other and the OER curve, it is difficult to discern the exact peak potentials and currents. The reduction peak shifts slightly negatively as the oxide develops, eventually stabilizing near $E_{\text{p,c}} = 1.35$ V. A trailing shoulder on this wave also forms between 1.22 and 1.30 V, indicating the presence of γ-NiOOH on the oxide surface.

Alloy C276 (Figure 4.2d) initially has a broad wave with no discernible peak during the forward scan, but develops into a single peak with a $E_{\text{p,a}}$ of 1.47 V similar to that seen in the pure Ni voltammogram. During the reverse scan, a small cathodic wave develops into a single peak at an approximately constant $E_{\text{p,c}}$ of 1.40 V. Unlike the other electrodes, there is almost no indication of γ-NiOOH on the surface.

4.3.2 Electrochemical Surface Area

Figure 4.3 shows the results of the open-circuit cycling procedure used to estimate the electrochemical surface area. Throughout development, the open circuit potential and charging current increases for all electrodes. The electrochemical response for alloy G35 was consistently noisy, and repetitions of the experimental procedure produced similar results. Consequently, accurate evaluation of the ECSA could not be conducted on alloy G35, and analysis is left out. The open circuit potential and ECSA for the first and last blocks are tabulated in Table 4.2. In general, the charging current increases with block number and scan rate. As a result, the ECSA for these three electrodes increases with block number, albeit at different rates. The ECSA of pure Ni increases logarithmically in the first few blocks, followed by an approximately linear increase in ECSA through the remainder of development. Alloy B3 initially increases linearly with ECSA, but begins to grow exponentially after the 11th development block. Alloy C276 has a small increase in ECSA during the first three blocks, followed by effectively no change during the remainder of development.

Table 4.2: Measured open circuit potential (E_{ocp}) and electrochemical surface area (ECSA) for the first (1) and last (14) blocks of the oxide development procedure.

	E_{ocp} / V		ECSA / cm^2	
	Block 1	Block 14	Block 1	Block 14
Ni	0.751	0.979	4.65	7.96
G35	0.188	0.873	–	–
B3	0.608	1.12	2.89	14.0
C276	0.586	0.770	1.95	2.73

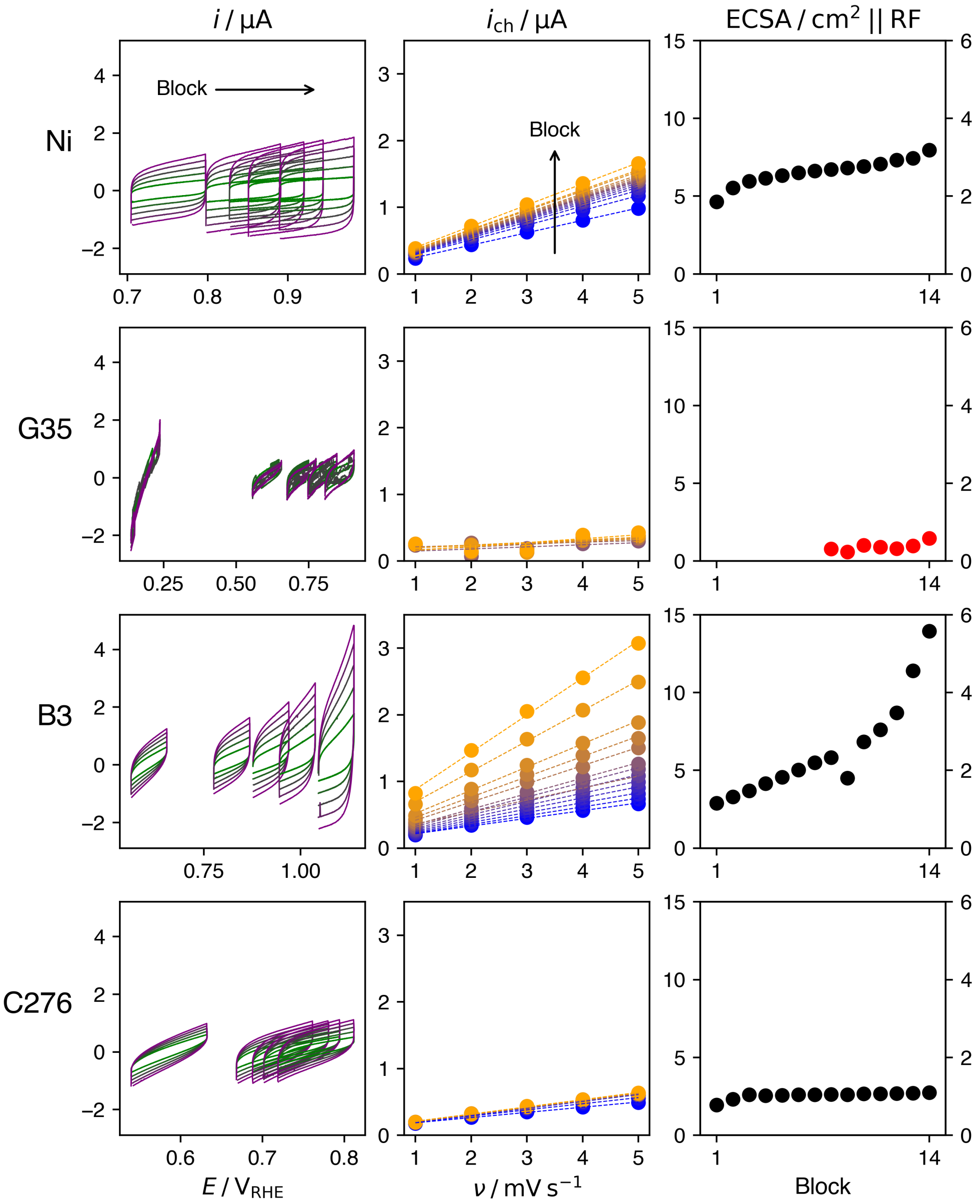

Figure 4.3: (Column 1) The open circuit cycling current response for each block at varying scan rates (increasing from green to purple), (Column 2) the calculated charging current *vs.* scan rate for each block, and (Column 3) the estimated ECSA and roughness factor as a function of block number.

4.3.3 Voltammetry of the Developed Oxide Layer

Figure 4.4 presents the final scan block corresponding to a DOL for each of the electrodes. Values of particular interest are the onset potential (E_{ons}), the peak potentials for the anodic ($E_{\text{p,a}}$) and cathodic ($E_{\text{p,c}}$) scans, and the half-wave potential ($E_{1/2}$). These values are shown in Table 4.3. $E_{\text{p,a}}$ and $E_{1/2}$ could not be precisely calculated for alloy B3 due to peak overlap during the anodic scan; however, it is estimated to be comparable to that of C276 due to their similar leading edges.

The onset potential is a measure of the minimum potential needed to oxidize Ni from $Ni(OH)_2$ to NiOOH. The E_{ons} is negatively shifted for the alloys compared to pure Ni. Alloy G35 is shifted the most, followed by B3 and C276. Alloy G35 also has a larger negative shift of $E_{\text{p,a}}$ as compared with the other electrodes. All the values of $E_{\text{p,c}}$ fall within a 4 mV

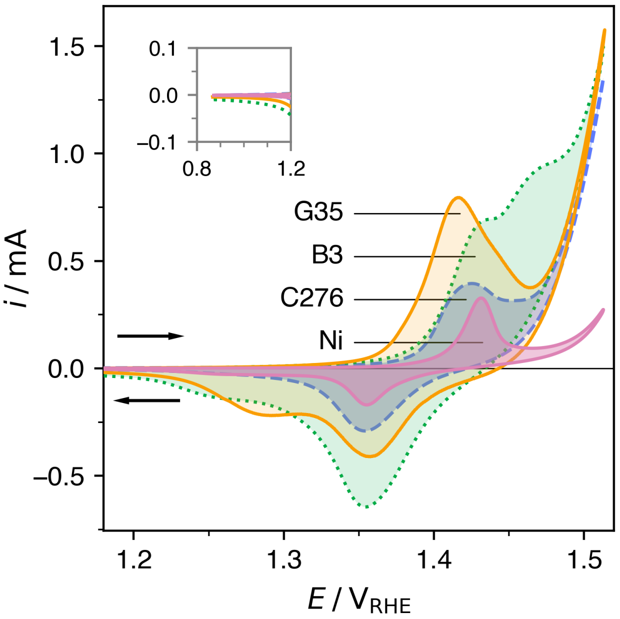

Figure 4.4: Third scan (1 mV s^{-1}) of the final block (14th) of the oxide development procedure for alloys G35 (high Cr:Mo), B3 (low Cr:Mo), C276 (equal Cr:Mo), and pure Ni. The inset shows the current response in the potential range of 0.8 to 1.2 V.

Table 4.3: Primary characteristic voltammogram potentials (V_{RHE}) for a developed oxide layer of Ni-based alloys and pure Ni. Parameters in order are the onset potential, anodic peak potential, cathodic peak potential, and half-wave potential. *Approximated due to significant peak overlap

	Cr:Mo	E_{ons}	$E_{\mathrm{p,a}}$	$E_{\mathrm{p,c}}$	$E_{1/2}$
Ni	NA	1.397	1.431	1.355	1.393
G35	High	1.351	1.417	1.358	1.387
B3	Low	1.367	1.43*	1.355	1.39*
C276	Equal	1.379	1.425	1.354	1.39

range. The calculable values for $E_{1/2}$ have a margin of error of 1.39 V ± 2.45 mV. In the case of all alloys, OER current measured at the switching potential (E_λ) of 1.52 V is 4–5 times larger than pure Ni.

4.3.4 Coulometry

To study changes in the oxide layer growth using coulometry, the “reduction” method — as described in Chapter 3 — was used to evaluate the reduction charge. Figure 4.5a shows the magnitude of cathodic charge passed during the final 1 mV s^{-1} scan of each block. The cathodic charge percent increase (CPI):

$$\mathrm{CPI}\,(\%) = \frac{q_{\mathrm{r},(n+1)} - q_{\mathrm{r},n}}{q_{\mathrm{r},n}} \times 100 \tag{4.3}$$

for each cycle is plotted in Figure 4.5b. To determine the limit of oxide growth, a bounded exponential growth model of the following form was fit to the charge progression from Figure 4.5:[91]

$$q_{\mathrm{r}} = q_{\mathrm{r,lim}} - (q_{\mathrm{r,lim}} - q_{\mathrm{r,0}})e^{-kn} \tag{4.4}$$

In this empirical equation, $q_{\mathrm{r,lim}}$ is the limiting cathodic charge, $q_{\mathrm{r,0}}$ is the initial cathodic charge, k is a growth rate constant, and n is the block number. Fitted values for $q_{\mathrm{r,0}}$, $q_{\mathrm{r,lim}}$,

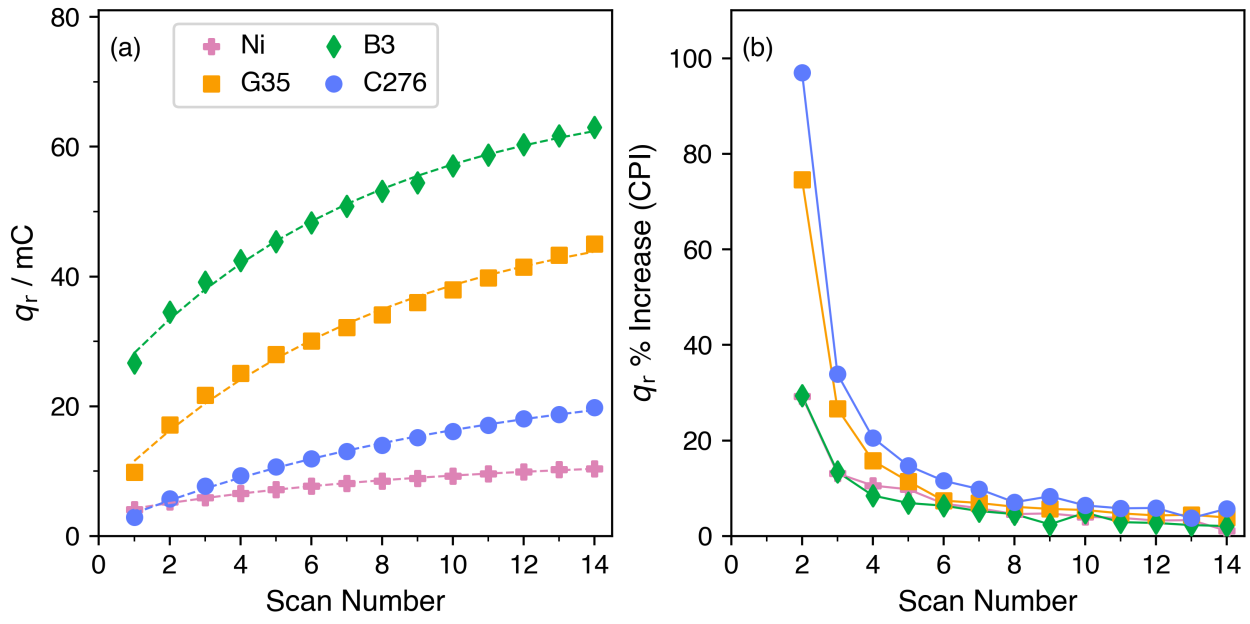

Figure 4.5: (a) Charge passed during the reverse (cathodic) sweep of each cycle, and (b) percent increase in cathodic charge passed from the previous cycle during the oxide layer development procedure. Equation 4.4 was used to fit the data in (a).

Table 4.4: Initial cathodic charge ($q_{\mathrm{r},0}$ / mC), limiting cathodic charge ($q_{\mathrm{r,lim}}$ / mC), and growth rate constant (k), residual standard error (RSE / mC), and number of cycles needed to reach steady state (n_{SS}) for the charge progression presented in Figure 4.5.

	$q_{\mathrm{r},0}$ / mC	$q_{\mathrm{r,lim}}$ / mC	k	RSE / mC	n_{SS}
Ni	3.40	12.4	0.107	0.097	41
G35	7.65	53.8	0.111	0.782	41
B3	22.0	69.4	0.137	0.702	31
C276	1.69	27.6	0.0834	0.229	55

and k are presented in Table 4.4, along with the residual standard error (RSE), used as a goodness-of-fit calculation, and n_{SS}, the number of blocks required to reach steady state. Steady state in this case is defined as the number of cycles needed to reach 99% of the limiting charge.

4.3.5 XPS

Alloy C276 was characterized before electrochemical cycling (undeveloped) as well as after the development procedure (developed) using XPS and is presented in Figure 4.6. Dehydration of the oxide layer between experiment and characterization — as well as the presence of an insulating potassium layer — resulted in noisy XPS data. To ensure the data are not over-analyzed, only the relative peak shapes and positions are discussed here.

The Ni 2p spectra (Figure 4.6a) for an undeveloped and developed oxide layer are effectively identical, having a main Ni $2p_{3/2}$ peak (856 eV), a Ni $2p_{3/2}$ satellite peak (861 eV), a Ni $2p_{1/2}$ main peak (873 eV), and a Ni $2p_{1/2}$ satellite peak (879 eV).[92, 93] The Cr 2p XPS spectrum for an undeveloped electrode (Figure 4.6b) has a Cr $2p_{3/2}$ peak at 577 eV and a

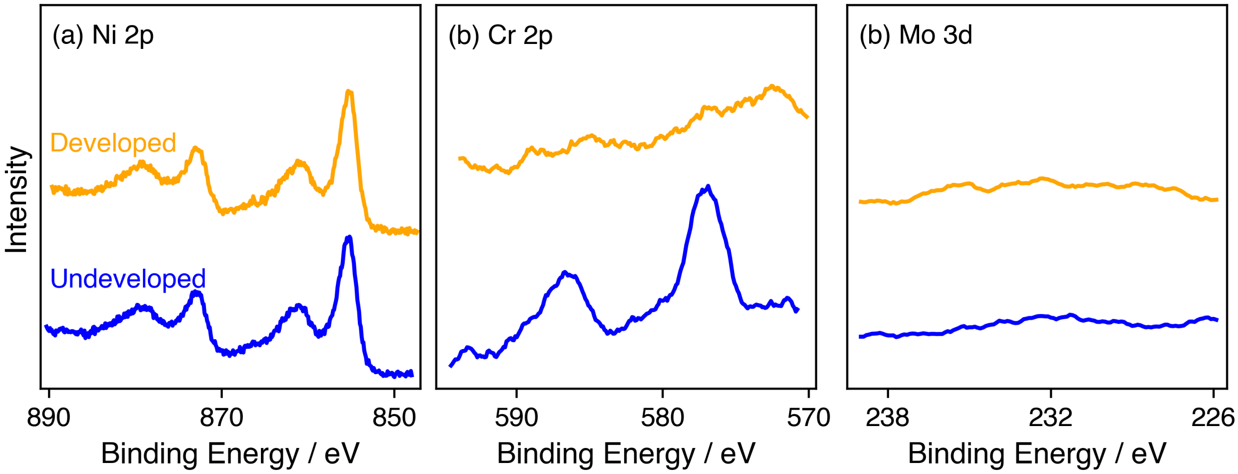

Figure 4.6: XPS spectra for the (a) Ni 2p, (b) Cr 2p, and (c) Mo 3d of alloy C276 before (blue) and after (orange) the oxide development procedure.

Cr $2p_{1/2}$ peak at 587 eV.[94, 95] After oxide development, there are no discernible peaks in the Cr 2p binding energy range. Mo was not detected in the Mo 3d binding energy range before or after the oxide development procedure.

4.4 Discussion

4.4.1 Oxide Layer Development

The voltammetric response of pure Ni (Figure 4.2a) shows that the generation of active β-NiOOH is crucial for OER, as the higher oxidation state assists in forming the necessary oxyhydroxide intermediates.[96] The oxygen evolution reaction has a lower standard equilibrium potential than the β-$Ni(OH)_2$ to β-NiOOH transformation, but its sluggish kinetics require a high overpotential. Throughout the development procedure, an increase in current indicates growth in the number of active, accessible Ni sites and thus a thickening of the oxide layer.

The electrochemical response of alloy G35 (Figure 4.2b) shows an additional peak at 1.38 V during the forward scan, and is attributed to the dissolution of chromium from the electrode; similar double-peaked features have been observed for pure Cr in alkaline solutions, and chromium is well known to oxidize in alkaline media through the following electrochemical process: [51, 77, 90, 97]

$$\mathrm{Cr(OH)_3} + 5\,\mathrm{OH^-} \longrightarrow \mathrm{CrO_4}^{2-} + 4\,\mathrm{H_2O} + 3\,\mathrm{e^-} \tag{4.5}$$

The double-peaked cathodic scans suggest a high concentration of γ-NiOOH in the oxide layer relative to the pure Ni electrode. The formation of γ-NiOOH is generally limited by the ability to intercalate water and cations between the hydroxide layers, but accessible reaction sites may be created due to passive layer dissolution. Consequently, the role of Cr in oxide development can be summarized as follows, and is shown in Figure 4.7:

- The formation of transport pathways due to Cr leaching exposes NiO and α-$Ni(OH)_2$, increasing the electrochemical surface area.

- Fresh α-Ni(OH)$_2$ can oxidize directly to γ-NiOOH, increasing its relative surface concentration throughout development.

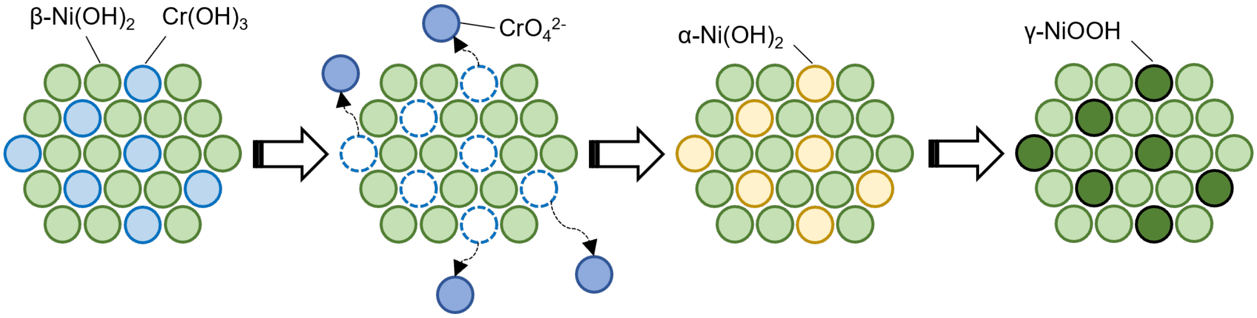

Figure 4.7: Schematic representation of the chromium dissolution reaction as described by Equation 4.5 and the subsequent exposure of available Ni sites.

For alloy B3 (Figure 4.2c), the shoulder at 1.43 V is presumably the β-Ni(OH)$_2$ to β-NiOOH transition, but the second shoulder at 1.47 V is unique to B3 and suggests the presence of an additional oxidation reaction. This feature is attributed to the electrochemical dissolution of Mo species, consistent with the high concentration of Mo in alloy B3. It has been documented that in alkaline conditions and under positive electrochemical bias, MoO_2 – the predominant Mo(IV) barrier species – will oxidize to form soluble Mo(VI) species:[76, 78, 98, 99]

$$\mathrm{MoO_2 + 2\,H_2O \longrightarrow HMoO_4{}^{-} + 3\,H^{+} + 2\,e^{-}} \tag{4.6}$$

Metallic Mo will also form (oxy)hydroxides, which can further oxidize to soluble Mo(VI) species:

$$\mathrm{Mo + 3\,OH^{-} \longrightarrow Mo(OH)_3 + 3\,e^{-}} \tag{4.7}$$

$$\mathrm{Mo(OH)_3 + 5\,OH^{-} \longrightarrow MoO_4{}^{2-} + 4\,H_2O + 3\,e^{-}} \tag{4.8}$$

Freshly exposed Mo sites on the electrode may continue to oxidize and reduce, thereby contributing to the high currents seen in alloy B3. Similar to the Cr-dissolution process shown in Figure 4.7, the dissolution of alloying elements may lead to an increase in accessible sites, improving the formation of γ-NiOOH.

Alloy C276 (Figure 4.2d) has 16% Cr and Mo, and one would expect to see the formation of γ-NiOOH due to leaching, as with the other alloys. This is not the case, however, and an explanation for this peculiarity lies in the high Cr and Mo concentrations; according to Klapper *et al.*, chromium has a strong influence on passive film formation by increasing the crevice corrosion initiation potential (breakdown potential) and temperature, but has little effect on the repassivation behavior.[70, 76] This means that even with a high Cr content, once corrosion begins a runaway dissolution mechanism will occur. Conversely, the repassivation potential of NiCrMo alloys is determined to be a stronger function of Mo content than Cr content.[70, 100] A critical concentration of both elements (11% for Cr and 13% for Mo) is required for complete passivation to occur.[100] Of the alloys studied here, only C276 meets these criteria. The implication here is that C276 undergoes less dissolution than the other alloys due to the high Cr and Mo concentrations, potentially preventing the formation of transport pathways and inhibiting the growth of γ-NiOOH.

The electrochemical surface area is an additional method for tracking oxide layer development, and is shown in Figure 4.3. In general, the ECSA increased with potential cycle, and the amount of increase varied greatly with electrode. For pure Ni and alloy C276, the most significant changes in ECSA happened during the early cycles of development. The likely explanation for this is due to the irreversible oxidation of the larger, hydrated α-Ni(OH)$_2$ layers (8 Å) to the more compact β-Ni(OH)$_2$ layers (4.6 Å), leading to surface roughening through lattice expansion and contraction. The final ECSA of pure Ni is 7.96 cm^2, corresponding to a roughness factor of approximately 3.2, calculated using the ratio of ECSA to geometric surface area. Conversely, alloy C276 has effectively no change in ECSA over the majority of development, reaching 2.73 cm^2 — a roughness factor of 1.1 — by the final block; the implication here is that the similarly high Cr and Mo concentrations inhibit dissolution, creating a stable oxide layer that does not significantly roughen in the examined potential window and time period. The rate of ECSA increase is greatest for alloy B3. The linear increase through the first 8 development blocks is presumed to be due to a mix of Ni-phase changes and molybdenum dissolution. It is hypothesized that given enough potential cycles, the stability of the oxide layer breaks down, resulting in a period of rapid Mo dissolution and oxide growth. As a result, an exponential ECSA increase is seen in development blocks 9 and onward.

The electrochemical responses of pure Ni, G35, B3, and C276 can be summarized as follows:

- Electrochemical dissolution of Cr and Mo occurs throughout the cycling process and is most prevalent during the oxidation of $Ni(OH)_2$ to NiOOH.
- Freshly exposed Cr and Mo sites on the electrode contribute to the overall higher current seen in alloys G35 and B3.
- Alloying element dissolution leads to an increase in transport pathways through the oxide layer, roughening the surface and increasing the ECSA. Direct oxidation of α-$Ni(OH)_2$ sites and improved intercalation of cations and water also increase the formation of γ-NiOOH.
- The dissolution of alloying elements and formation of γ-NiOOH is more pronounced for electrodes with dissimilar concentrations of Cr or Mo (G35 and B3). At similar concentrations of Cr and Mo (C276), a more stable surface layer consisting primarily of β-NiOOH is formed upon oxidation.

4.4.2 Voltammetry of the Developed Oxide Layer

To further analyze the NiCrMo electrodes, characteristic potentials and features for a developed oxide layer were evaluated (Figure 4.4 and Table 4.3). A negative shift in onset potential is often attributed to improved electrical conductivity of the electrode or electrolyte, as well as cation intercalation and lattice structural differences between the alloys.[101] It has been reported that the intercalation of alkali metal ions such as K^+ and Na^+ between layers of

$Ni(OH)_2$ during the charging process can cause a negative shift in onset potential.[102] This may lead to stabilization of α-$Ni(OH)_2$, suppressing its transformation to β-$Ni(OH)_2$ and favoring the formation of γ-NiOOH.[26] An increase in transport pathways due to Cr and Mo leaching may lead to improved K^+ intercalation, driving the formation of γ-NiOOH and negatively shifting the $Ni(OH)_2$ to NiOOH redox onset potential through α-$Ni(OH)_2$ stabilization.

Chromium and molybdenum oxidation at potentials near the $Ni(OH)_2$ to NiOOH redox peaks may affect the measurement of onset potential. To account for this, examination of the peak and half-wave potentials can provide a better estimate of the characteristic Ni redox features. In this case, $E_{\mathrm{p,a}}$ acts as a marker for the overall $Ni(OH)_2$ to NiOOH oxidation reactions and is comparable for all the electrodes. The E^{o} value for the α-$Ni(OH)_2 \rightleftharpoons \gamma$-NiOOH reaction is reported to be between 30 and 50 mV less than that of the β-$Ni(OH)_2 \rightleftharpoons \beta$-NiOOH reaction, meaning that the formation of even small amounts of γ-NiOOH can cause negative shifts in the peak potentials.[26] For alloy G35, increased formation of γ-NiOOH— caused by Cr dissolution — leads to a shift in peak potential as well as an increase in current and electrochemical surface area. The cathodic peak potential, $E_{\mathrm{p,c}}$, is a useful benchmark for the β-NiOOH reduction reaction as there is less overlap with the γ-NiOOH peak. The values of $E_{\mathrm{p,c}}$ fall within a 4 mV range, indicating that, while exposed Cr and Mo may contribute to increased reduction current, there is little effect on the reduction potential of β-NiOOH.

The half-wave potential $E_{1/2}$ is often used to fingerprint reversible electrochemical reactions as it is an excellent estimate of E^{o}.[66] For all electrodes, the values of $E_{1/2}$ are similar and in good agreement with reported values.[26] It should be noted that that $E_{1/2}$ values presented in Table 4.3 are calculated using the $E_{\mathrm{p,a}}$ values from the combined oxidation peak, which will lead to some discrepancy with other sources.

4.4.3 Coulometry

The coulometry data presented in Figure 4.5 were used to estimate and track growth of the oxide layer. Before electrochemical cycling, the electrode surface will consist primarily of α-Ni(OH)$_2$ due to its spontaneous formation in alkaline environments, even when non-polarized.[25] When positively polarized, α-Ni(OH)$_2$ is irreversibly and rapidly transformed to β-Ni(OH)$_2$, leading to significant oxide growth (20%+ CPI/cycle) during the early stages of oxide development (blocks 1-3). α-Ni(OH)$_2$ also directly forms γ-NiOOH, leading to the characteristic double-peaks seen in the early scans of Figure 4.2. During the middle cycles (blocks 4-7), oxide growth begins to slow (10-20% CPI/cycle) as the amount of surface α-Ni(OH)$_2$ decreases and the more-stable β-Ni(OH)$_2$ $\rightleftarrows$ β-NiOOH redox pair becomes the dominant surface process. By block 8, the CPI is less than 10%, and by block 13, is under 5% for all electrodes. This region has little change in the characteristic voltammogram shape, suggesting the surface composition stays relatively uniform. Consequently, oxide layer thickening through charge/discharge cycling is presumed to be the primary electrochemical process occurring in this region.

From the fitting parameters shown in Table 4.4, the cathodic charge limit $q_{\mathrm{r,lim}}$ is of particular interest as it can be used to estimate the relative, steady-state oxide thickness. For a given number of cycles, alloys B3 and G35 — containing the Mo and Cr extremes, respectively — pass more charge than a balanced Cr-Mo electrode. Pure Ni passes the least charge of all examined electrodes. It is unlikely that the difference in charge is due to an improvement in electrical or ionic conductivity as previously discussed, suggesting a mechanical or structural improvement is responsible. Alloy C276 has the lowest k value out of the electrodes, emphasizing the alloy's stability under polarizing conditions. In all cases, the RSE is less than 1.5% of $q_{\mathrm{r,lim}}$, indicating the empirical equation is a good fit for the presented data.

4.4.4 XPS

To verify the claim that Cr and Mo dissolution contribute to the formation of transport pathways, XPS was conducted on alloy C276 before and after oxide development, and the resulting spectra are shown in Figure 4.6. The Ni $2p_{3/2}$ main peak is a singlet, indicating the presence of $Ni(OH)_2$ or NiOOH. Considering XPS was conducted ex-situ, any NiOOH would likely discharge to $Ni(OH)_2$ in the time between experiment completion and characterization, and . The "flattened" Ni $2p_{1/2}$ peak indicates a multiplet-split peak, suggesting the presence of NiO in the oxide layer.[92, 93] As a result, a mixed NiO-$Ni(OH)_2$ oxide is believed to make up the bulk of the outer layer. The undeveloped Cr 2p spectra shows two singlet peaks at 577 and 587 eV. In both cases, however, the width of these peaks suggests multiple overlapping peaks, indicating a mixed oxide-hydroxide layer.[94, 95] Consequently, the oxide layer of an undeveloped electrode in alkaline electrolyte is believed to contain chromium primarily in the Cr(III) form, present as both $Cr(OH)_3$ and Cr_2O_3. Molybdenum was not present in either of the XPS spectra in the Mo 3d binding energy range. Considering alloy C276 has 16% Mo, it is likely that Mo is simply not present in the outer layer of the oxide structure.

The results here support the claim that dissolution of Cr is occurring, even if the cyclic voltammograms do not show a corresponding current response. The implication here is that the dissolution of Cr may occur by both electrochemical or chemical dissolution, depending on the electrode. Regarding Mo, the lack of peaks both before and after electrochemical cycling clouds analysis, and the results here neither confirm nor deny that this metal is leaching during the cycling process. Consequently, a more in-depth XPS characterization should be conducted, and the results here are simply an exploratory analysis. Conducting XPS on the remaining alloys — in a more controlled environment — and using XPS spectra fitting software would provide more conclusive evidence of metal dissolution.

4.5 Conclusions

Electrochemical oxidation and development of the oxide layer of Ni and NiCrMo alloys in alkaline electrolyte was studied as a function of potential cycling. Voltammetry and XPS were used to characterize and compare the behavior of the electrodes, from which the following conclusions can be drawn:

- Varying the concentration of alloying elements led to preferential formation of different Ni(III) phases, but the characteristic potentials of the α-Ni(OH)$_2$ $\rightleftarrows$ γ-NiOOH and β-Ni(OH)$_2$ $\rightleftarrows$ β-NiOOH reactions were unaffected.
- Leaching of alloying elements led to an increase in transport pathways and electrochemical surface area, improving the formation of the γ-NiOOH phase.
- Alloys with dissimilar Cr:Mo ratios (G35, B3) had significantly higher oxidation and reduction currents than the alloy with a similar Cr:Mo ratio (C276) or pure Ni. This may be due to exposed Cr and Mo that do not dissolve, but rather continuously oxidize and reduce alongside Ni during the cycling process.

Chapter 5

NICKEL-CHROMIUM-MOLYBDENUM MATERIALS FOR THE ELECTROCHEMICAL HYDROGEN EVOLUTION, OXYGEN EVOLUTION, AND UREA OXIDATION

5.1 Motivation

In Section 4.1, the electrochemically formed oxide layer was investigated using a variety of electrochemical and materials characterization. It was determined that the presence of Cr or Mo led to preferential formation of different NiOOH phases, the active species towards oxygen evolution and urea oxidation. To assess the viability of NiCrMo materials as alkaline electrocatalysts for these reactions, kinetic benchmarks should be measured. In this chapter, potential-step and cyclic voltammetry are used to investigate the electrocatalytic activity of NiCrMo alloys towards the HER, OER, and UOR. Tafel analysis and turnover frequency are the electrochemical benchmarks used to quantify the electrocatalytic activity.

5.2 Experimental

5.2.1 Electrochemical Procedures

After forming a DOL as described in 4.2, the electrolyte KOH concentration was increased to 1 M, and a potential-step experiment was conducted with 10 mV steps between 1.47–1.62 V_{RHE}, each step held for 15 minutes at which an approximately steady-state current was reached. The final 3 minutes (1800 data points) for each step were averaged to reduce noise. The OER overpotential at pH 14 was calculated using an E^{o} of 1.23 V_{RHE}.

Following the potential step experiment, the electrode was cycled in 1M KOH between 1.12–1.62 V_{RHE}, 75 times at 15 mV s^{-1} to open the potential window of the electrode. Two slow scans (1 mV s^{-1}) were then conducted in the same range. Subsequently, urea was added to the electrolyte to create a 1 M KOH + 0.01 M urea electrolyte, and the 1.12–1.62 V_{RHE} cycling procedure was repeated. Finally, the urea concentration of the electrolyte was increased to 0.33 M and the cycling procedure repeated.

In a separate experiment, an electrode with an undeveloped oxide layer was submerged in 1 M KOH. The electrode was cycled 30 times between 0 and –0.46 V_{RHE} at 30 mV s^{-1} to reduce the air-formed oxide layer. Finally, a single scan between 0 and –0.46 V_{RHE} was conducted at 1 mV s^{-1}. The HER overpotential at pH 14 was calculated using an E^o of 0 V_{RHE}.

5.3 Results

5.3.1 Oxygen Evolution

Figure 5.1 shows (a) polarization curves and (b) Tafel plots for each of the electrodes. Char-

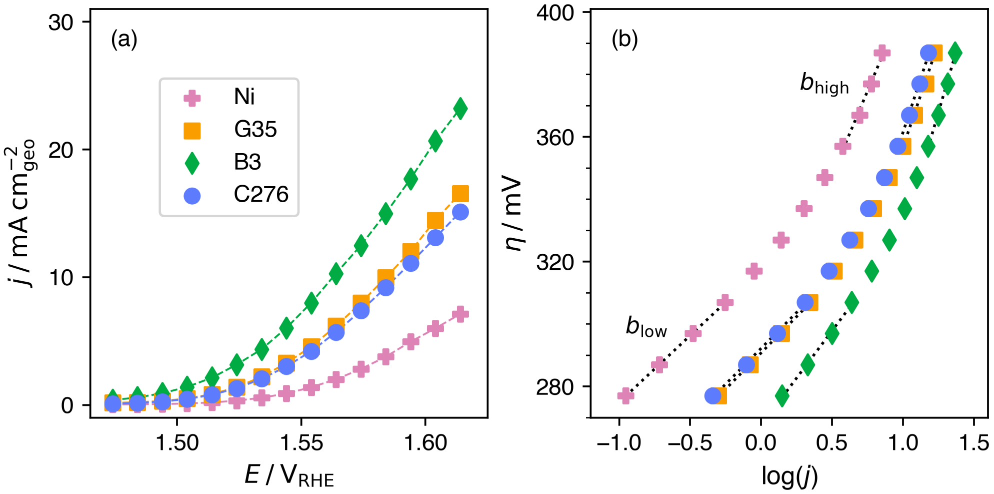

Figure 5.1: (a) Polarization curves and (b) Tafel plots for Ni, G35 (high Cr:Mo), B3 (low Cr:Mo), and C276 (equal Cr:Mo). Data extracted from potential step experiments. The electrolyte is 1 M KOH and stirred using a magnetic stir-bar at 200 RPM to improve mass-transfer.

acteristic values for these plots, including the OER overpotential required to produce 10 mA $\text{cm}_{\text{geo}}^{-2}$ of current (η_{10}) and Tafel (b) slopes, are presented in Table 5.1. Two overpotential ranges are designated: a low range of 270–310 mV (b_{low}) and a high range of 350–390 mV (b_{high}).

The polarization curves show an OER onset potential in the range of 1.49 to 1.52 V for all electrodes. The η_{10} values for alloys G35, B3, and C276 were 58, 80, and 54 mV lower than that for pure Ni. In the low overpotential range, alloys G35, C276, and Ni have comparable Tafel slopes. In the high overpotential range, all alloys have noticeably higher Tafel slopes than pure Ni. The Tafel slope of alloy B3 is noticeably higher than for the other electrodes in both overpotential ranges.

The third kinetic benchmark used for OER is the turnover frequency (TOF), presented in Figure 5.2 and evaluated using the equation:[103]

$$\text{TOF} = \frac{jN_A}{nF\Gamma_{\text{r}}} \tag{5.1}$$

where j is the OER current density, N_A is the Avogadro number, n is the number of electrons exchanged during OER (4), F is the Faraday constant, and Γ_{r} is the reduction site density. The TOF evaluated here is based on the amount of available sites as determined by the reduction charge in the voltammograms from Figure 4.4, calculated as described in Chapter 3.

Table 5.1: Overpotential (η_{10} / mV) required to reach 10 mA $\text{cm}_{\text{geo}}^{-2}$ and Tafel slopes (b / $\text{mV}\,\text{dec}^{-1}$) for the polarization curves presented in Figure 5.1. Tafel slopes were calculated using data points in the overpotential ranges of 270-310 mV (b_{low}) and 350-390 mV (b_{high}).

	Cr:Mo	η_{10}	b_{low}	b_{high}
Ni	NA	415	42.7	108
G35	High	357	46.4	134
B3	Low	335	60.6	156
C276	Equal	361	45.9	138

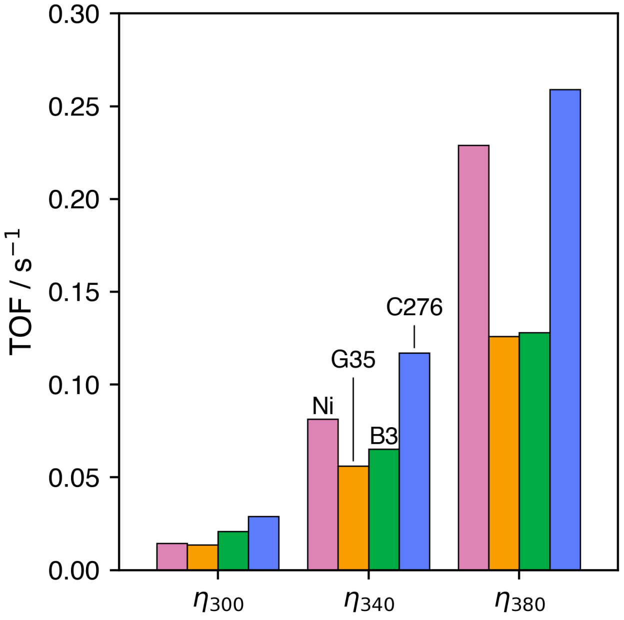

Figure 5.2: Calculated TOF values at overpotentials of 300, 340, and 380 mV. Bars from left to right are as follows: Pure Ni (pink), G35 (orange, high Cr:Mo), B3 (green, low Cr:Mo), and C276 (blue, equal Cr:Mo).

The majority of reduction current is attributed to the reduction of β-NiOOH and γ-NiOOH, as the characteristic half-wave and cathodic peak potentials are approximately the same for the alloys and pure Ni. The reduction of other alloy-specific species cannot be ruled out, however, and would require further quantitative investigation. Turnover frequencies were calculated for three overpotentials (300, 340, and 380 mV), which encompass the range of Tafel slope measurements. In the low overpotential range (η_{300}), TOF values are highest for alloys C276 and B3, followed by pure Ni and G35. At η_{340}, the TOFs increase by a factor of three or more; the value for C276 is greatest, followed by pure Ni, B3, and G35. In the highest overpotential region, η_{380}, the TOFs for Ni and C276 are similar and markedly greater than those for G35 and B3.

5.3.2 Urea Oxidation

Figure 5.3 shows the current response in the potential window of 1.12 – 1.62 V for electrodes in (a) 1 M KOH, (b) 1 M KOH + 0.01 M urea, and (c) 1 M KOH + 0.33 M urea. In 1 M KOH (Figure 5.3a), the characteristic NiOOH peaks are different from those observed in Section 4.1; pure Ni has a peak at 1.395 V, followed by a trailing shoulder. Alloy G35 has two clear peaks at 1.39 and 1.42 V, alloy B3 has a wide plateau between 1.40 and 1.45 V, and alloy C276 has a peak at 1.39 V and a plateau between 1.42 and 1.45 V. At higher oxidation potentials (>1.5 V), the oxygen evolution reaction is the dominant electrochemical process.

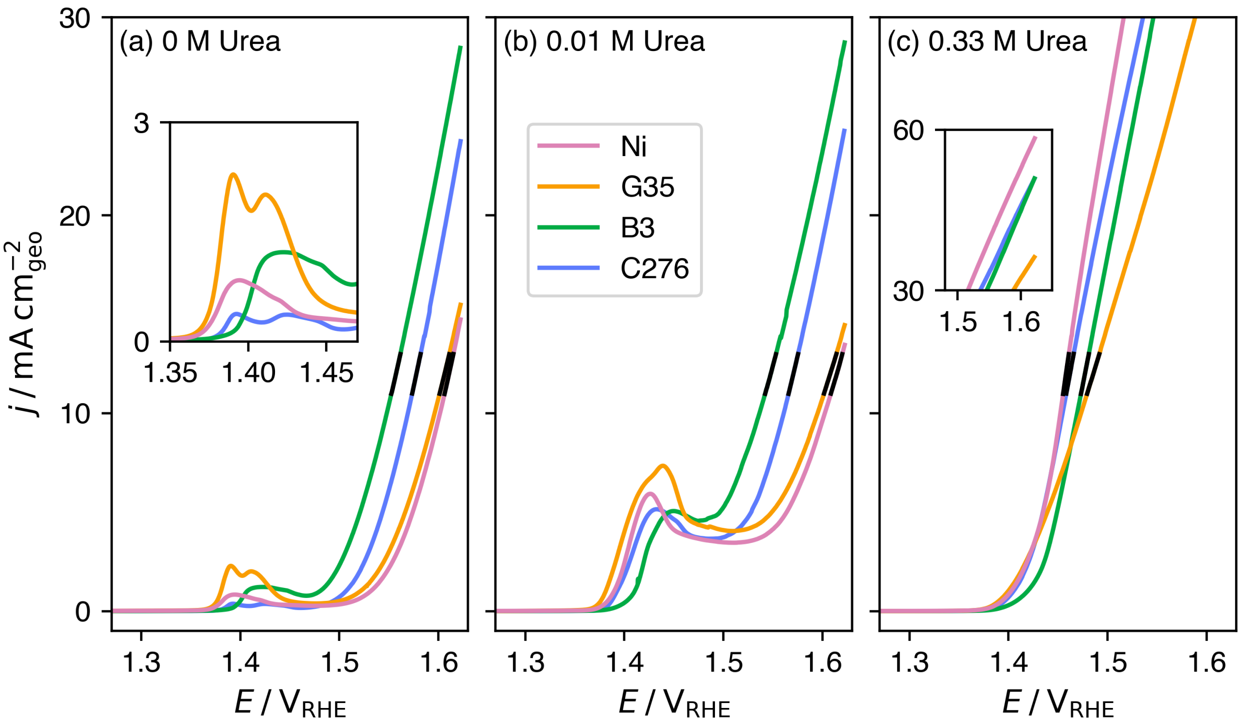

Figure 5.3: Linear sweep voltammograms for the examined electrodes in 1 M KOH and (a) 0 M urea, (b) 0.01 M urea, (c) 0.33 M urea. The inset in (a) is a zoomed view of the Ni(II) to Ni(III) oxidation peak, while the inset in (c) shows the extent of the current response at the highest potentials

When a small amount (0.01 M) of urea is added (Figure 5.3b), new electrochemical features are visible; in the potential range of 1.37–1.45 V, the NiOOH peaks increase by a factor of up to 9 for all the examined electrodes. Between approximately 1.45 V and 1.53 V, all electrodes have varying degrees of a current plateau. At higher potentials, the oxygen evolution reaction is the dominant electrochemical process.

When a high concentration (0.33 M) of urea is added to the electrolyte (Figure 5.3c), the current response is markedly different from the previous cases; mainly, the electrochemical onset potential is approximately the same as (a) and (b), but there is no peak visible in the range of 1.37–1.45 V. Near potentials between 1.47 and 1.50 V, the current response shows a slight "bend" before increasing semi-linearly at higher potentials.

5.3.3 Hydrogen Evolution

Kinetics of the hydrogen evolution reaction were estimated by cycling in a reducing potential range (0 to –1.46 V). A slow scan rate of 1 mV s^{-1} was used to minimize the effect of capacitive current on the calculated Tafel slopes. The final scan for this procedure is presented in Figure 5.4, along with the calculated Tafel slopes for each electrode. Generally, cyclic voltammetry is not used to measure Tafel slopes due to the inherent unsteady-state value of current. To ensure the activity was measured equivalently for all electrodes, Tafel slopes were evaluated at a set current range, rather than at a set overpotential. The elected current range was between –1 and –2 mA cm_{geo}^{-2}, roughly equivalent to the onset potential of each voltammogram.

Pure Ni had a noticeably lower onset overpotential for the HER; the onset overpotential was approximately 157, 65, and 58 mV less than alloys G35, B3, and C276, respectively. Tafel slopes were also evaluated; the slopes for alloys G35 and C276 (95.4 and 97 mV dec^{-1}) were markedly lower than the identical Tafel slopes of pure Ni and alloy B3 (121 mV dec^{-1}). As the exact electrochemical surface area could not be readily determined in the reducing potential range of the HER, turnover frequency was not calculated.

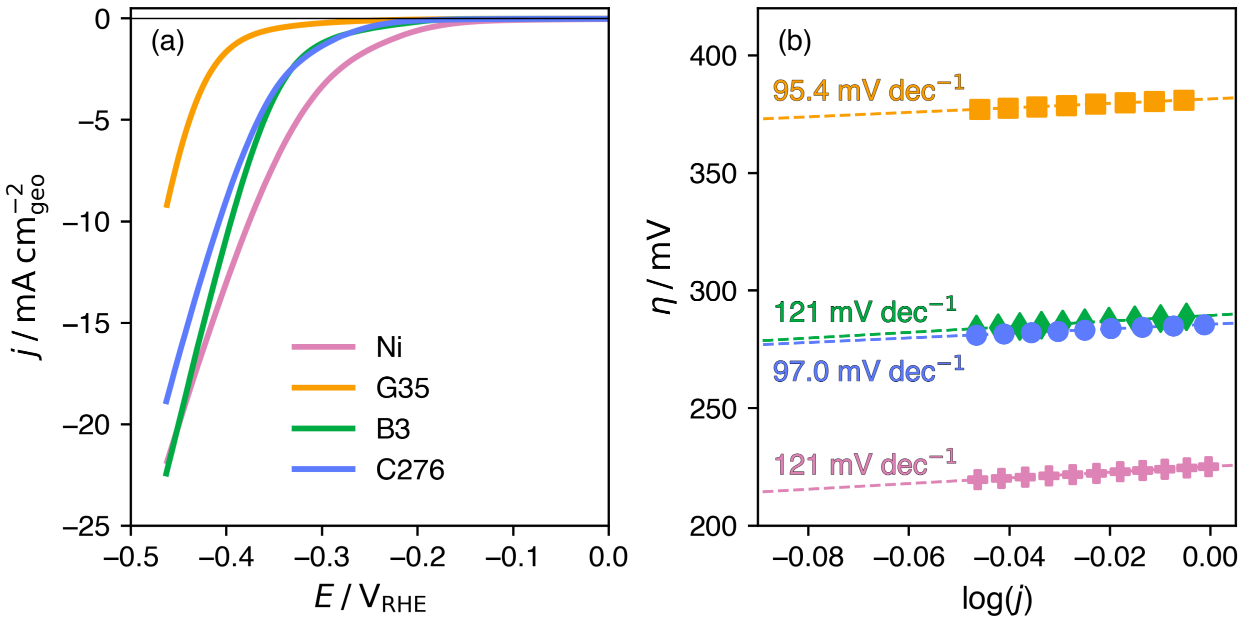

Figure 5.4: (a) Linear sweep voltammogram in the hydrogen evolution region for the examined materials. (b) Tafel plot for the corresponding electrodes, evaluated in the –1 to –2 mA cm_{geo}^{-2} region, along with the calculated Tafel slopes

5.4 Discussion

5.4.1 Oxygen Evolution — Tafel Analysis

The overpotential required to produce 10 mA cm_{geo}^{-2} is one common benchmark used to evaluate the kinetics of the OER reaction, and is shown in Table 5.1. The results here indicate that alloys G35, B3, and C276 all have improved OER kinetics, as their values of η_{10} are 58, 80, and 54 mV lower than that of pure Ni. Due to the likelihood of Cr or Mo dissolution occurring during this potential range, however, the measured current may not be completely due to the OER. As a result, additional kinetic benchmarks should be used to evaluate the electrochemical performance. Tafel slopes in two overpotential ranges are calculated for the electrodes and shown in Table 5.1. For Ni, the values of b_{low} and b_{high} of 42.7 and 108 mV dec^{-1} are reasonably close to values of 40 and 120 mV dec^{-1} derived from a microkinetics model of OER by Shinagawa *et al.*[28] This particular combination of Tafel slopes results from two possible rate-determining steps:[28]

$$\text{RDS-1:} \quad \mathrm{MO + OH^- \rightleftarrows MOOH + e^-} \tag{5.2}$$

$$\text{RDS-2:} \quad \mathrm{MOO^- \rightleftarrows M + O_2 + e^-} \tag{5.3}$$

Distinguishing the exact rate-determining step (RDS) would require a more thorough investigation of reaction mechanisms than presented here. Comparing these possible reactions to the mechanism discussed in 2, however, indicates that the RDS may be the formation of a NiOOH site, a claim corroborated by Lyons & Brandon.[104] The implication here is that the type of NiOOH species formed may have considerable impact on the overall kinetics of the OER.

In the low overpotential range, alloys G35, C276, and Ni have comparable Tafel slopes, suggesting similar OER mechanisms and rate-determining steps. In the high overpotential range, Tafel slopes for pure Ni, G35, and C276 fall in a range encompassing the value of 120 $\mathrm{mV\,dec^{-1}}$ expected for an ideal, one-electron transfer reaction.[28] The Tafel slope of alloy B3 is noticeably higher than for the other electrodes in both overpotential ranges, however, indicating a possible change in reaction mechanism or at least a different rate-determining step within the same mechanism. Molybdenum oxidation may also contribute to the discrepancy in Tafel slopes for alloy B3; as seen in Figure 4.2c, there is significant non-OER current at potentials greater than 1.5 V, overlapping with the OER feature.

5.4.2 Oxygen Evolution — Turnover Frequency

The turnover frequency is defined as the number of catalytic cycles per unit time, and is a measure of the intrinsic activity of a catalyst. In Figure 5.2, it is clear that the TOF values for pure Ni and alloy C276 are comparable and considerably higher than alloys G35 and B3. One explanation for this is the relationship between Cr:Mo ratio and γ-NiOOH formation; the electrodes with dissimilar Cr:Mo ratios (G35 and B3) have lower TOF, yet form higher concentrations of γ-NiOOH than those with similar Cr:Mo ratios (or no Cr/Mo).

The implication here is that the γ-NiOOH phase has a lower TOF relative to the β-NiOOH phase, corroborating a report that the β-NiOOH phase is more active towards OER than the γ-NiOOH phase.[105]

One final point regards the results for OER kinetics based on geometric surface area (Figure 5.1) *vs.* density of active sites (Figure 5.2). Specifically, Ni and C276 require higher overpotentials for a given current density, yet exhibit higher TOFs compared to alloys G35 and B3. We interpret this along the line of total accessible surface area *vs.* accessible oxyhydroxide sites. While exposed Cr and Mo contribute to the high electrochemical surface area of alloys G35 and B3, these alloying elements are inactive towards OER in the measured potential range.[34, 106] As a result, the TOF values for G35 and B3 are lower than those for Ni and C276, the electrodes with less total electrochemical surface area but higher concentrations of active NiOOH sites.

5.4.3 Urea Oxidation

Using a wide potential window, the electrochemical oxidation of urea was examined at low (0.01 M) and high (0.33 M) concentrations in 1 M KOH, and the voltammetric response is shown in Figure 5.3. In the “blank” electrolyte (0.5 M KOH only), all the electrodes had NiOOH oxidation features with multiple peaks. There are two likely contributing factors to this occurrence: increased electrochemical formation of the γ-NiOOH phase and the dissolution of alloying element, the latter having been previously discussed in Section 4.1. Due to the higher switching potential used here (1.62 *vs.* 1.56 V_{RHE}), an increase in oxygen evolution — and consequently overcharge — will lead to an increase in γ-NiOOH formation. This is caused by surface place-exchange mechanisms occurring in parallel with the OER at high potentials, leading to structural rearrangement and surface roughening.[107–109] The results here indicate that how an oxide layer forms — and the corresponding relative composition of β-NiOOH and γ-NiOOH— is dependent on the potential window used.

When 0.01 M urea is added to the electrolyte and the cycling procedure is repeated, the electrochemical response changes. In the potential range of 1.35–1.45 V, the current magnitude of the NiOOH peaks increases by a factor of 2–9 depending on the electrode. The increase in current is due to the electrochemical oxidation of urea through the direct Equation 5.4 and/or indirect Equation 5.5 mechanisms.[12, 47]

$$\text{Direct:} \qquad \mathrm{CO(NH_2)_2 + OH^- \longrightarrow N_2 + CO_2 + 5\,H_2O + 6\,e^-} \tag{5.4}$$

$$\text{Indirect:} \qquad \mathrm{CO(NH_2)_2 + 6\,NiOOH + H_2O \longrightarrow N_2 + CO_2 + 6\,Ni(OH)_2} \tag{5.5}$$

Due to the catalytic nature of these reactions, it is difficult to directly isolate and quantify the decomposition rate of urea separate from current due to $Ni(OH)_2$ oxidation. One method often used is to examine the region following the NiOOH peak, but before significant urea oxidation begins. In Figure 5.3, this would be at approximate 1.47 V. For all electrodes, this point corresponds to a current plateau, estimated to be the mass-transfer limited urea oxidation reaction. At 1.47 V, the current ranges from 5.5 mA (pure Ni and alloy C276) to 7.0 mA (alloys G35 and B3), a 24% difference. The likelihood of Cr and Mo dissolution in this potential range may explain the difference, but additional experimentation and data is required.

Increasing the urea concentration to 0.33 M results in another significant change in current response. The oxidation peak usually seen between 1.37–1.45 V is no longer visible. The higher concentration of urea changes the system from mass-transfer limited to kinetically limited, hiding the current plateau seen in Figure 5.3(b). Moreover, there is a slight increase in onset potential of the combined $Ni(OH)_2$ and urea oxidation wave as compared to the 0.01 M urea electrolyte. While urea is considered a small organic molecule, its presence in a high concentration may act as an inhibitor for the $Ni(OH)_2$ oxidation reaction, resulting in a slight decrease in kinetics. At higher potentials, (> 1.55 V), large currents indicate parallel OER and UOR.

Benchmarking the urea oxidation kinetics is difficult due to its overlap with both the $Ni(OH)_2$ oxidation reaction and the oxygen evolution reaction. When parallel reactions are occurring, an “effective” Tafel slope is measured; the fastest reaction will dictate the Tafel slope magnitude, but the rate is influenced by the presence of other reactions. The effective

Table 5.2: Effective Tafel slopes (b) and potential required to generate 10 mA $\mathrm{cm}_{\mathrm{geo}}^{-2}$ of current (E_{10}) evaluated for electrodes in 1 M KOH plus 0 M, 0.01 M, or 0.33 M urea

	b / mV dec^{-1}			E_{10} / V		
	0 M	0.01 M	0.33 M	0 M	0.01 M	0.33 M
Ni	121	160	78.5	1.62	1.62	1.46
G35	134	173	170	1.61	1.61	1.49
B3	124	150	108	1.56	1.55	1.48
C276	116	131	102	1.58	1.58	1.47

Tafel slopes for the data presented in Figure 5.3 are shown in Table 5.2. As an additional benchmark, the potential required to generate 10 mA $\mathrm{cm}_{\mathrm{geo}}^{-2}$ of current (E_{10}) is also calculated.

The Tafel slopes here are evaluated not at the onset potential, but rather in a constant current range (17–19 mA) to ensure equivalent reaction rates for all urea concentrations, as indicated by the black lines in Figure 5.3. When no urea is included in the system, the Tafel slopes range from 116–134 mV dec^{-1}, bracketing the expected, limiting 120 mV dec^{-1} value for the OER seen in a microkinetics study and Table 5.1.[28] When urea is added to the system at a concentration of 0.01 M, all Tafel slopes increase by 15–39 mV dec^{-1} depending on the electrode. The potential range where this is measured, however, is effectively identical to that of 0 M urea. This indicates that the OER is still the dominant electrochemical reaction being measured, and the increase in Tafel slope is due to an inhibition of the OER reaction kinetics. The presence of urea in a low concentration will occupy some active NiOOH sites, reducing accessible electrochemical surface area for the OER. When the urea concentration is increased to 0.33 M, the trends in Tafel slope change; for pure Ni, alloy B3, and alloy C276, the Tafel slopes decrease to values lower than the 0 M or 0.01 M systems. Here, it is suggested that — when at a high enough concentration — urea oxidation is a faster electrochemical process than the OER, resulting in a significant decrease in Tafel slope. This claim has been recently corroborated by Li *et al.*, who came to the conclusion that the UOR was more facile than the OER by examining Ni-based layered double hydroxides in 1 M KOH and 0.5 M urea.[110] Alloy G35 does not follow this trend, however, having approximately the same, higher Tafel slope for 0.01 M and 0.33 M urea. One possible explanation for this occurrence is simply that G35 is less active towards UOR than the other electrodes. Considering that alloy G35 had a considerably higher γ-NiOOH percentage than the other electrodes, it would suggest that β-NiOOH is the more active phase towards the UOR.

When using urea oxidation for hydrogen production, an important benchmark is the potential required to generate 10 mA $\mathrm{cm}_{\mathrm{geo}}^{-2}$ of current. As seen in Table 5.2, when no urea is in the system and the OER is the anodic process, potentials between 1.56–1.62 $\mathrm{V}_{\mathrm{RHE}}$ are required. The addition of 0.01 M urea does not lead to a significant shift in E_{10}, as the OER is still the dominant anodic process. At 0.33 M urea, however, the potential required for 10 mA $\mathrm{cm}_{\mathrm{geo}}^{-2}$ is 80 to 160 mV less than 0 M urea; due to NiOOH's affinity for the UOR, a considerably lower overpotential — and electrical input — is needed. The values for all electrodes are comparable, but follow the same trend as the Tafel slopes for 0.33 M urea.

5.4.4 Hydrogen Evolution

The hydrogen evolution reaction was examined for each electrode and is shown in Figure 5.4. Pure Ni had the lowest onset overpotential out of all the examined electrodes, followed by alloys B3 and C276, and then alloy G35. This trend is not matched by the Tafel slopes, which are low for alloys G35 and C276 (95.4 and 97.0 $\mathrm{mV\,dec^{-1}}$), and high for pure Ni and alloy B3 (121 $\mathrm{mV\,dec^{-1}}$). A likely explanation for this occurrence is the presence of chromium on alloys G35 and C276, and the relationship between the HER Tafel slope, overpotential, and Cr-content is summarized in Figure 5.5.

In the reducing potential range of HER, Cr dissolution does not occur, and instead leads to the formation of Cr_2O_3, a passivated Cr(III) layer. This oxide component acts as a stabilizing agent towards NiO_x, the active species towards the HER, by preventing it from

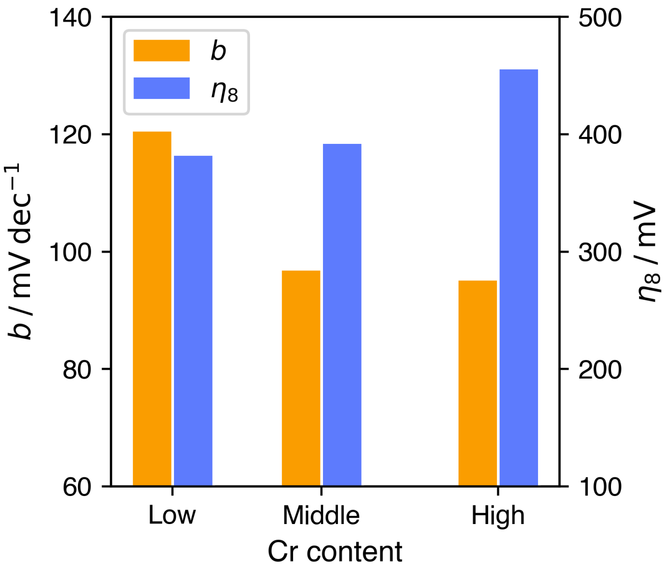

Figure 5.5: The Tafel slope (b, orange) and overpotential required to generate 8 mA cm^{-2} of HER current (η_8, blue) for the three Cr-containing alloys

reducing to metallic Ni.[111] The comparably low Tafel slopes for the Cr-containing alloys is evidence for this synergistic relationship. The variance in the HER overpotential may also be caused by the differing chromium concentrations, as Cr_2O_3 is an insulating oxide component. By reducing the electrical conductivity of the electrode, a higher overpotential would be required to overcome the activation barrier for the HER, reducing the kinetics of the HER. Alternatively, as seen in alloy C276, the addition of Mo helps maintain the low HER overpotential while also reducing the Tafel slope.

5.5 Conclusions

Through the electrochemical studies described in this chapter, the characteristics and viability of NiCrMo alloys as oxygen evolution, hydrogen evolution, and urea oxidation catalysts have been examined. From these results, the following conclusions have been drawn:

- NiCrMo electrodes show increased OER kinetics per geometric area relative to pure

Ni, although Ni and C276 have higher and similar TOFs compared to those of G35 and B3. The difference in OER activity can be attributed to the differing electrocatalytic properties of β-NiOOH and γ-NiOOH.

- Pure Ni has a lower Tafel slope than all NiCrMo alloys, indicating it has faster UOR reaction kinetics. All electrodes require similar overpotentials, however.
- Hydrogen evolution overpotentials and Tafel slopes appear to be a strong function of the electrode's Cr content, and that formation of an insulating Cr_2O_3 oxide layer may contribute to higher HER overpotentials and lower HER Tafel slopes.

The β-NiOOH and γ-NiOOH concentrations had a strong influence on the OER — and to a lesser degree, the UOR — kinetics. It is clear that understanding the electrochemical characteristics of each of these phases is necessary to understand the Ni-oxide layer, and an in-depth investigation of this phenomenon is conducted in chapter 4. Regarding urea oxidation, it is clear that all the Ni-based catalysts are electrochemically active. In 0.33 M urea, specifically, a significant reduction in overpotential required to generate 10 mA $\mathrm{cm}_{\mathrm{geo}}^{-2}$ of current for all electrodes highlights how wastewater or urine can be used to generate lower-cost hydrogen. Moreover, the Tafel slopes indicate that the viability of NiCrMo electrodes as urea oxidation electrocatalysts depends on the system conditions. For urine and wastewater streams (0.33 M urea), a pure Ni is the catalyst of choice.[112] In 0.01 M urea — the approximate concentration of urea in dialysate fluid — both alloys C276 and B3 have improved UOR kinetics (∼10–20%) over pure Ni.[113] For dialysis and other low urea concentration applications, using a high Cr or high Mo will improve reaction kinetics. Finally, the HER kinetics appeared to be related to the Cr and Mo concentrations. The inclusion of Cr led to a decrease in Tafel slope, while also including Mo resulted in a lower overpotential than just Cr.

Chapter 6

SELECTIVE DEVELOPMENT OF NICKEL OXYHYDROXIDES THROUGH ELECTROCHEMICAL CYCLING TECHNIQUES

6.1 Motivation

In Section 4.1, oxide development and electrochemical analysis was conducted on a series of nickel-chromium-molybdenum alloys. It was determined that the relative concentration of β-NiOOH and γ-NiOOH were directly tied to the oxygen evolution, hydrogen evolution, and urea oxidation electrocatalytic properties. While the relationship between these NiOOH phases is well-described by the expanded Bode diagram (Figure 2.1), practical electrochemical control of these surface species has not been extensively studied. Pissinis *et al.* devised special potential-scan techniques to increase the growth of γ-NiOOH species, while Dose *et al.* used targeted electrochemical aging protocols to control capacity loss in nickel-rich lithium-ion batteries.[85, 114] The reaction mechanisms are suggested to differ between the oxyhydroxide phases, as indicated by respective Tafel slops of 89 and 104 $\mathrm{mV\,dec^{-1}}$ for β-NiOOH and γ-NiOOH, though this is presumably not the case for all redox reactions.[105, 115] In general, electrochemical techniques are more often used as diagnostic and characterization tools, but these studies indicate that specific cycling techniques can be used to target desirable electrochemical properties.

In this chapter, the relationship between potential and surface NiOOH phases is examined through the application of cyclic voltammetry, chronoamperometry, and electrochemical impedance spectroscopy. Characteristic electrochemical parameters are estimated using coulometry, peak fitting, and equivalent circuit fitting. Differing oxyhydroxide phases are imaged by scanning electron microscopy (SEM). These methods make it possible to quantify changes in the catalyst surface as a function of electrochemical cycling and switching potential, influence the relative surface concentrations of NiOOH phases, and observe the relationship between surface state and reaction kinetics.

6.2 Experimental

6.2.1 Electrodes

The working electrode was prepared by sanding a 99.995% Ni disk (ESPI Metals) using 240 and 600 grit sandpaper until planar, followed by polishing with 9, 3, and 1 micron diamond suspensions (Buehler) until a mirror surface was obtained. The geometric surface area of the polished region was calculated to be 0.709 $\mathrm{cm}^2_{\mathrm{geo}}$. After polishing, the working electrodes were sonicated in deionized water and dichloromethane (99.5 wt.%, Fisher Scientific) for 15 minutes each to remove remaining surface contaminants. A Pt coil (ca. 5 cm^2) was used as the counter electrode, while an uncalibrated, double-junction mercury oxide electrode (Hg/HgO, 4.24 M KOH, Pine electrochemistry) was used as the reference electrode. All reported voltages are with respect to the reversible hydrogen electrode (RHE), calculated using Equation 4.1.

6.2.2 Electrochemical Apparatus

All electrochemical experiments were performed in a glass 150 mL, three-electrode cell (Pine electrochemistry). The cell was filled with concentrated H_2SO_4 ($>$ 51 wt.% , Mallinckrodt Chemicals) for at least an hour before experimentation to remove trace amounts of iron and other metal solutes in the glass. The electrolyte was an unstirred, 0.5 M potassium hydroxide (KOH) solution created using KOH pellets (87.4 wt.%, Fisher Scientific) and DI water (0.04 $\mu\mathrm{S\ cm}^{-1}$). A 25 °C water bath (Fisher Scientific) was used to maintain a constant cell temperature. A Solartron 1287 potentiostat paired with a Solartron 1252A frequency response analyzer was used to collect electrochemical data.

The working electrode was first heated by electron bombardment in vacuum to temperatures greater than 600 °C.[116] As seen in Figure 6.1, the vacuum chamber was connected to the electrochemical cell through a gate valve and a ConFlat-to-glass connection. The ConFlat connection had a gas port used to replace the cell headspace with argon gas (Linde, 99.998 %). Once heated and cooled under vacuum, the working electrode was lowered into the three electrode cell under argon flow to prevent oxygen exposure. When the electrolyte's surface tension was broken, the electrode was raised to form a meniscus on the surface. This prevented reactions from occurring on the sides and top of the electrode and improved the removal of gaseous products from the electrolyte. Electrochemical experiments were initiated immediately upon exposure of the working electrode to the alkaline electrolyte.

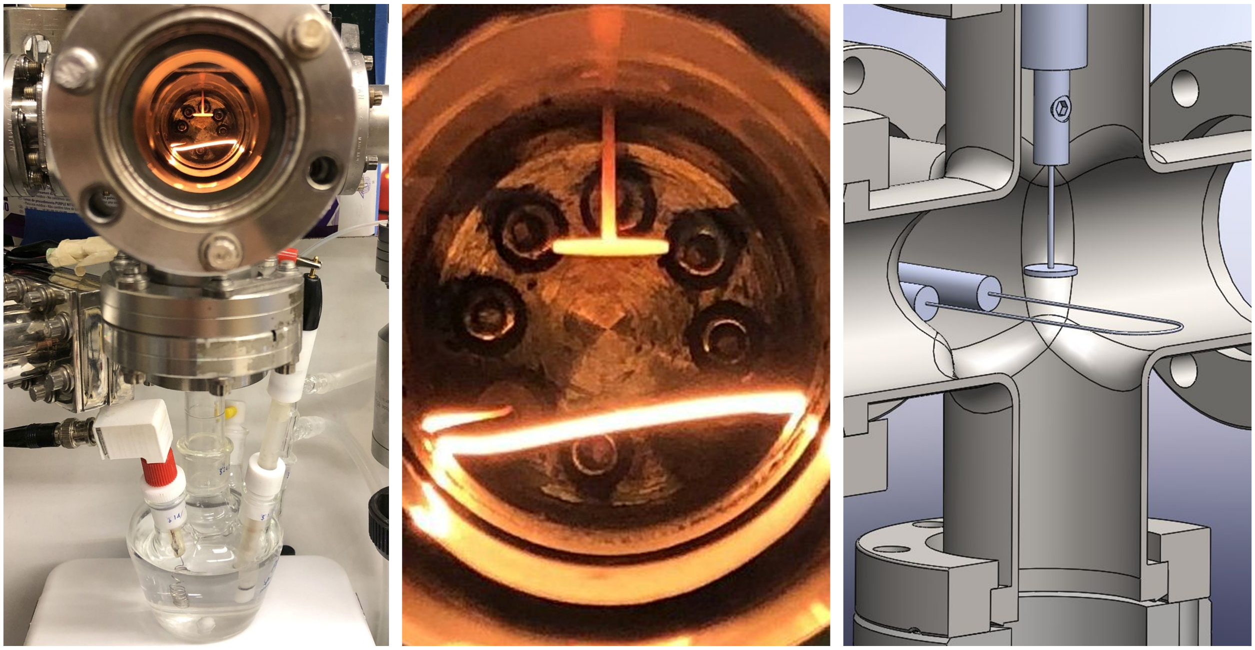

Figure 6.1: Left: vacuum chamber and three electrode cell. Center: close-up of the vacuum chamber where the working electrode was heated to thermally desorb oxides. Right: 3D-rendered cross-section of vacuum system showing the filament and electrode position during heating

6.2.3 Electrochemical Methods

A 600-cycle oxide development procedure was performed using cyclic voltammetry (CV) for switching potentials (E_λ) between 1.51 and 1.61 V in 0.02 V increments per 600-cycle set. The starting potential was 0.90 V, and the scan rate was 10 mV s^{-1}. Following oxide development, EIS was conducted every 10 mV between 1.51 and 1.66 V using an amplitude of 5 mV and a frequency range of 100 kHz to 0.1 Hz. Overpotentials were calculated using the standard equilibrium potential of 1.23 V_{RHE} for OER in 0.5 M KOH at 25 °C.

6.2.4 Scanning Electron Microscopy

The morphology of electrodes after thermal annealing in vacuum and after oxide development for switching potentials of 1.51 and 1.61 V was analyzed by scanning electron microscopy (SEM) *via* a ThermoFisher Scientific Apreo-Symmetry with Ultimax 100 at 2kV with 65x–25,000x magnification. Electrodes were placed in ethanol (95 wt. %, Fisher-Scientific) post-heating or post-electrochemical treatment and were sampled immediately.

6.3 Results

To electrochemically activate Ni electrodes and develop an oxide layer in alkaline medium, potential cycling was conducted up to varying switching potentials, as presented in Figure 6.2. During the forward (anodic) scan, current response is minimal until an oxidation wave forms at potentials greater than 1.36 V (A^*). The peak potential for this wave is initially between 1.37 and 1.38 V, shifting positively and increasing in magnitude throughout oxide development and stabilizing between 1.40 and 1.43 V (peak A) depending on E_λ. An exponential current response corresponding to the oxygen evolution reaction is observed at potentials greater than 1.46 V. The magnitude of OER current increases with scan number, denoted by a vertical arrow. During the reverse (cathodic) scan, a single peak between 1.28 and 1.32 V is initially observed (C^*). As the number of cycles increases, this feature either remains a single peak (Figure 6.2a), splits into multiple peaks (Figure 6.2b-e), or forms a

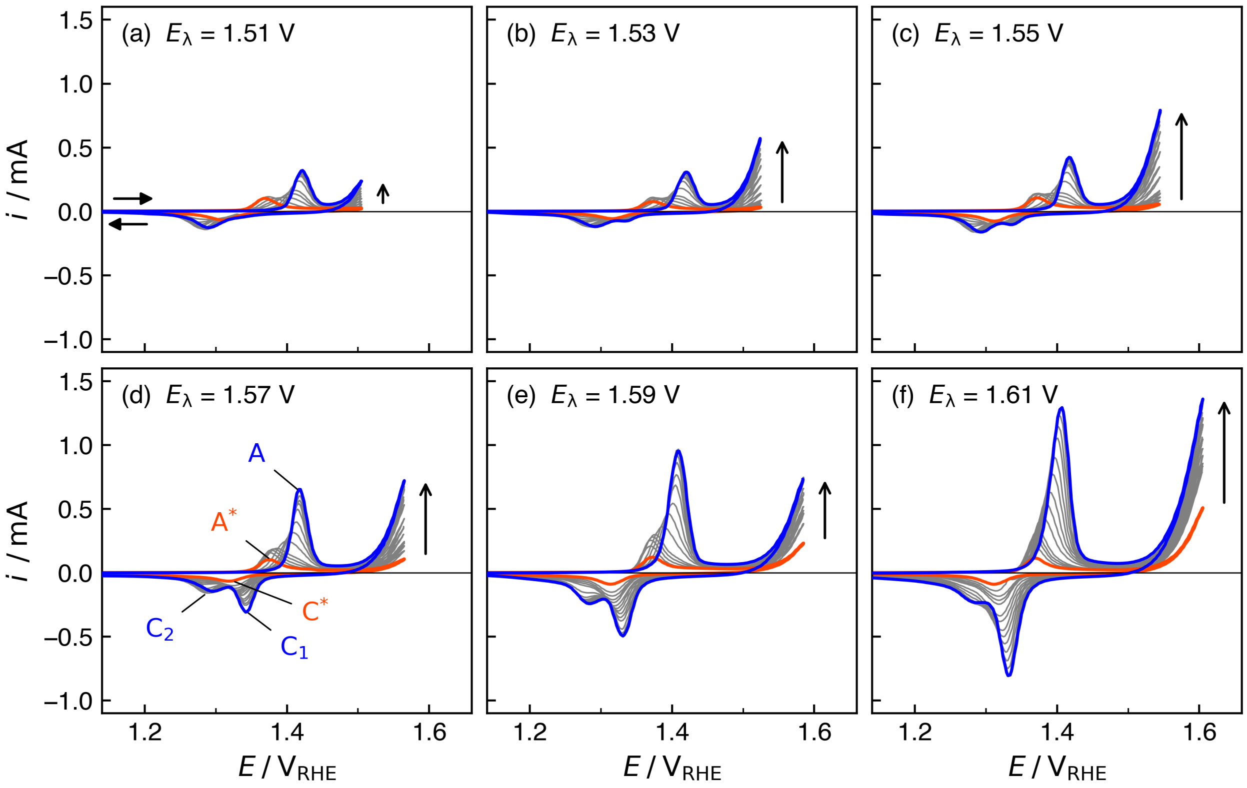

Figure 6.2: Oxide development cyclic voltammograms for switching potentials of (a) 1.51, (b) 1.53, (c) 1.55, (d) 1.57, (e) 1.59, and (f) 1.61 V_{RHE}. The initial scan is orange, while gray lines indicate every 60th scan up to the final (blue), 600th scan. The scan direction is denoted by the horizontal arrows, while the vertical arrow shows the change in maximum OER current over the course of oxide development

peak with a shoulder (Figure 6.2f). Reduction peak and shoulder potentials are between 1.29 and 1.35 V (peaks C_1 and C_2). The reduction current magnitude increases with cycle number, more notably for the higher E_λ values. This increase in current corresponds to a thickening of the Ni oxide layer.

Figure 6.3a shows the anodic current normalized by ECSA using Equation 3.22 The magnitude of the Ni oxidation wave is approximately constant, when normalized according to ECSA, while the onset potential undergoes a slight negative shift at the two highest

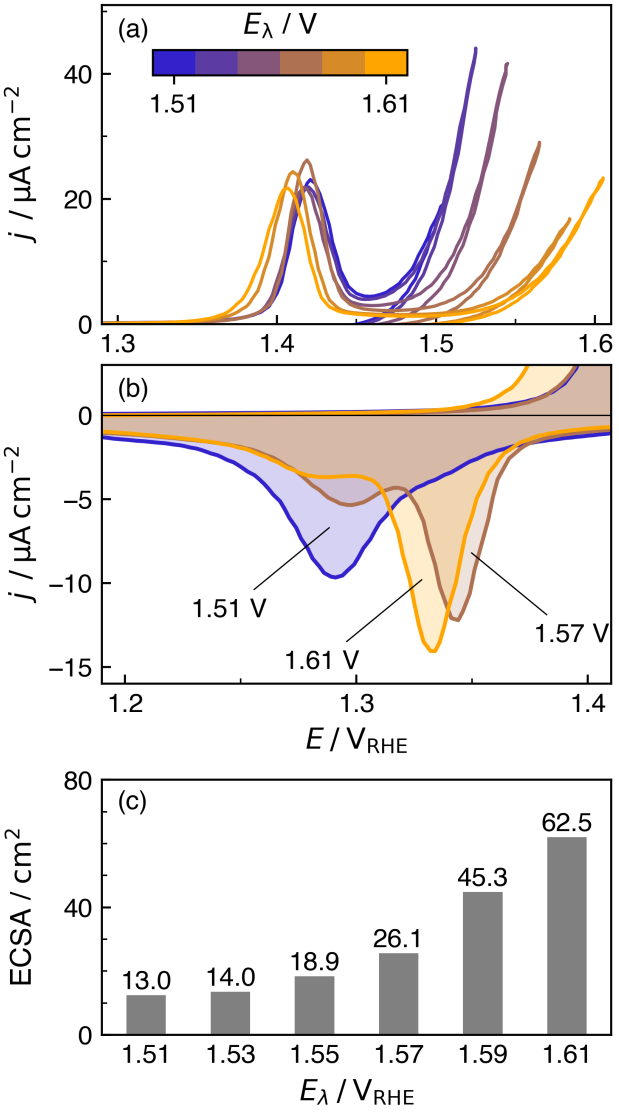

Figure 6.3: (a) The final (600th), forward oxide development sweep for each E_λ potential, presented as ECSA-normalized current. (b) The corresponding reverse sweep for selected switching potentials. (c) ECSA, calculated using Equation 3.22

switching potentials. The OER feature at potentials greater than 1.46 V shifts positively with switching potential. The ECSA-normalized reduction waves for switching potentials of 1.51, 1.57, and 1.61 V are shown in Figure 6.3b. Here, the reduction peak between 1.29 and

1.30 V is the most pronounced for a E_λ of 1.51 V, followed by those at 1.57 V and 1.61 V. The peak between 1.33 and 1.35 V is most pronounced for a E_λ of 1.61 V followed closely by the peak at 1.57 V, while only a small shoulder is visible for a E_λ of 1.51 V. The values of ECSA used to normalize the data are shown in Figure 6.3c.:

6.3.1 Potentiostatic Hold

Figure 6.4 shows a 10-hour potential hold at 1.61 V conducted after oxide development for switching potentials of 1.53 and 1.61 V. After the initial step to 1.61 V, the current for the electrode with a switching potential of 1.53 V is approximately 3x higher than that of the electrode developed with a switching potential of 1.61 V. Both currents initially decay, reaching a minimum after $\sim$ 1 hour. Both currents then increase over the remaining 9 hours, with final values of 4.9 and 2.9 mA for switching potentials of 1.53 and 1.61 V, respectively.

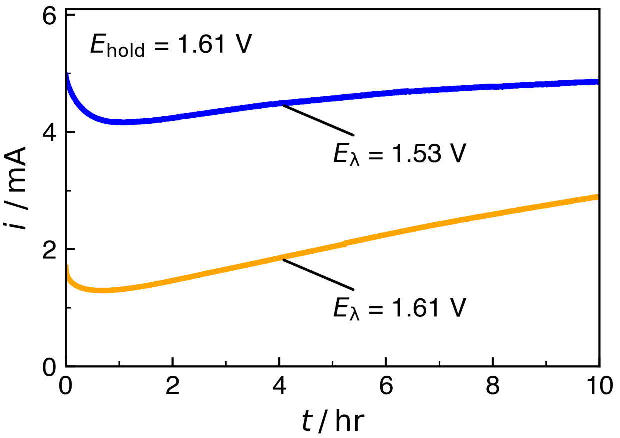

Figure 6.4: Current response for a 10 hour potentiostatic hold at 1.61 V after 600 cycles up to 1.53 V (blue) and 1.61 V (orange)

6.3.2 Electrochemical Impedance Spectroscopy

A Nyquist plot for EIS conducted at 1.61 V for electrodes developed with different switching potentials is shown in Figure 6.5. A simplified Randles circuit — inset in Figure 6.5 — is used for equivalent circuit fitting, and the resulting parameters are tabulated in Table 6.1. Nyquist plots for other biases are shown in Figure B.6 and Figure B.7. With increasing switching potential, both the charge transfer resistance and the constant phase element (CPE) parameter increase. The capacitance was estimated for each curve fit and is presented along with the remaining fitting parameters in Figure B.8. The ohmic resistance stays approximately constant with switching potential, while the charge transfer resistance increases. All values for the CPE exponent are within a range of 0.946–0.972. The effective capacitance trends upwards with switching potential, and this value was used to estimate the ECSA using the 'Impedance Method' as described in Chapter 3.

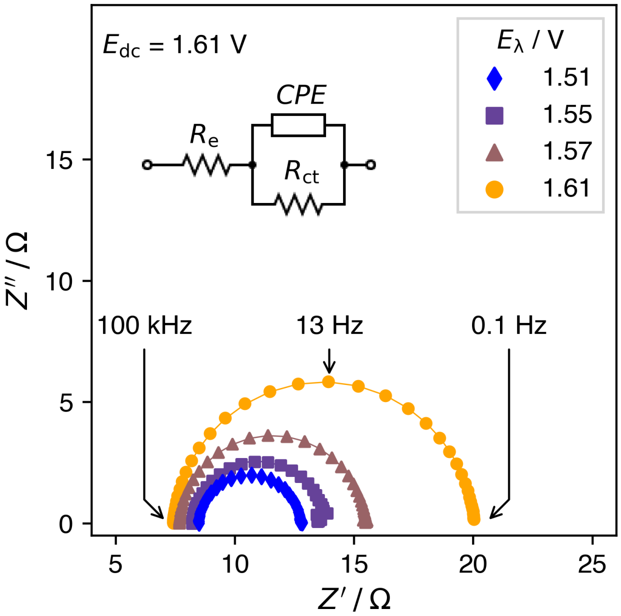

Figure 6.5: Impedance spectroscopy conducted at a bias of 1.61 V for a series of electrodes developed with different switching potentials

Table 6.1: Equivalent circuit fitting parameters for EIS data presented in Figure 6.5. Values from left to right are the switching potential (E_λ), ohmic resistance (R_e), charge-transfer resistance (R_ct), CPE parameter (Q_o), CPE exponent (n), the effective capacitance (C_eff), and the electrochemical surface area (ECSA)

E_λ/ V	R_e / Ω	R_ct / Ω	Q_o / mS $\mathrm{s}^{-\alpha}$	n	C_eff / mF	ECSA / cm^2
1.51	8.47	4.3	0.762	0.951	0.555	13.9
1.53	7.61	4.18	0.704	0.946	0.493	12.3
1.55	8.24	5.37	0.721	0.972	0.608	15.2
1.57	7.65	7.84	0.884	0.95	0.656	16.4
1.59	10.1	13	1.14	0.949	0.873	21.8
1.61	7.4	12.6	1.21	0.95	0.919	23.0

6.3.3 SEM

SEM images of electrodes before and after oxide development using switching potentials of 1.51 V and 1.61 V are shown in Figure 6.6. The undeveloped electrode (Figure 6.6(a)) exhibited grain structures similar to those of electrodes annealed in vacuum as reported in the literature.[117, 118] The electrode developed with a switching potential of 1.51 V had larger facet planes and fewer grain boundaries than the electrode developed with a switching potential of 1.61 V. The larger facets in Figure 6.6(b) showed large, uniform planes with length scales greater than 250 μM, while smaller facets showed broken planes with mottled texture and sizes ranging from 10–200 μM, as seen in Figure 6.6(c).

6.4 Discussion

6.4.1 Oxyhydroxide Development

Before electrochemical cycling, the Ni working electrode was subjected to a thermal desorption preparation procedure at temperatures greater than 600 °C to remove surface oxides

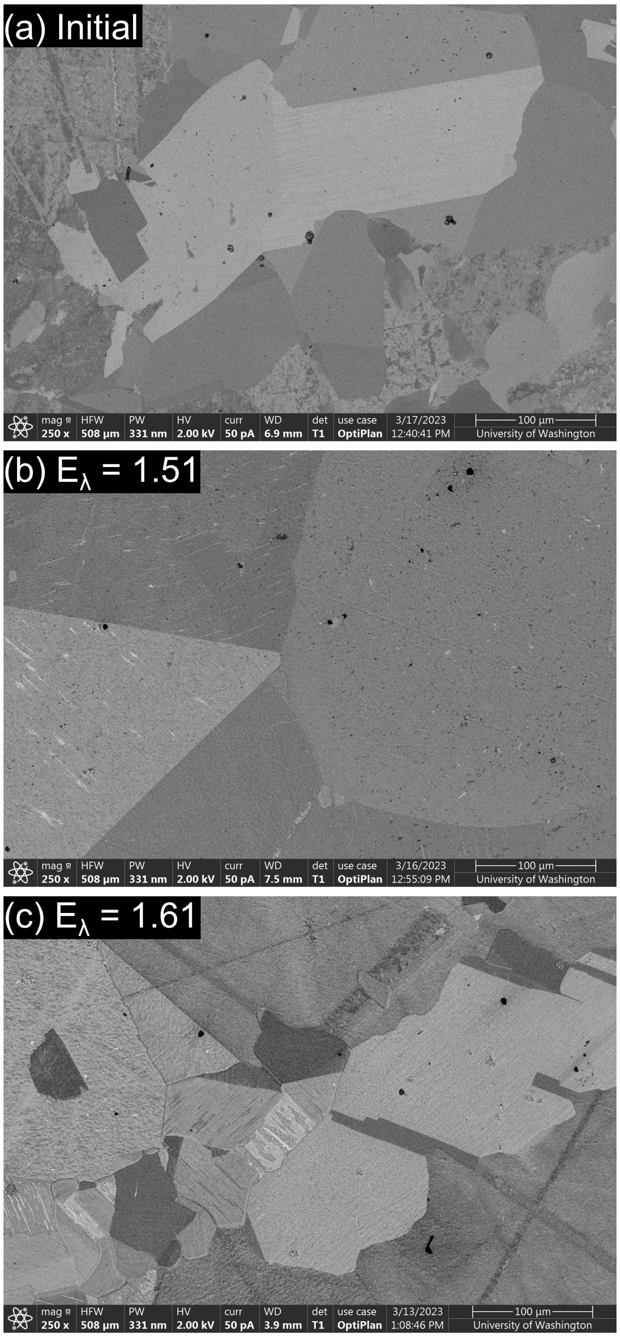

Figure 6.6: 250x scanning electron microscopy images of nickel electrodes with (a) initial and post-oxide growth procedures for (b) 1.51 V and (c) 1.61 V switching potentials.

and contaminants. According to Alsabet *et al.*, α-Ni(OH)$_2$ is the predominant Ni phase to form after high-temperature annealing and exposure to alkaline media, which is attributed to the low standard equilibrium potential of the Ni to α-Ni(OH)$_2$ reaction (0.256 V_{RHE}).[25] A primarily α-Ni(OH)$_2$ surface will oxidize to both β-Ni(OH)$_2$ and γ-NiOOH, forming a high concentration of the latter. In Figure 6.7, the anodic peak near 1.37 V (A^*) corresponds to the α-Ni(OH)$_2$ to γ-NiOOH oxidation reaction, with a matching reduction peak near 1.32 V (C^*). As the electrode is cycled, peak A^* shrinks while a new, larger anodic peak forms (A) with a peak potential of 1.42 V. Peak A is almost universally attributed to the β-Ni(OH)$_2$ to β-NiOOH oxidation reaction.[25, 36, 119] During the cathodic sweep, the reduction of γ-NiOOH appears as a peak near 1.34 V (C_1), while the reduction of β-NiOOH to β-Ni(OH)$_2$ appears as a peak near 1.29 V (C_2).[85] As γ-NiOOH reduces to both α-Ni(OH)$_2$ and β-NiOOH, it is difficult to identify which species is preferentially formed during the reduction reaction. Considering β-Ni(OH)$_2$ the more thermodynamically stable phase, the reduction of γ-NiOOH to β-Ni(OH)$_2$ would seem preferred.[22]

When the cycling process is repeated at different switching potentials, the electrochemical

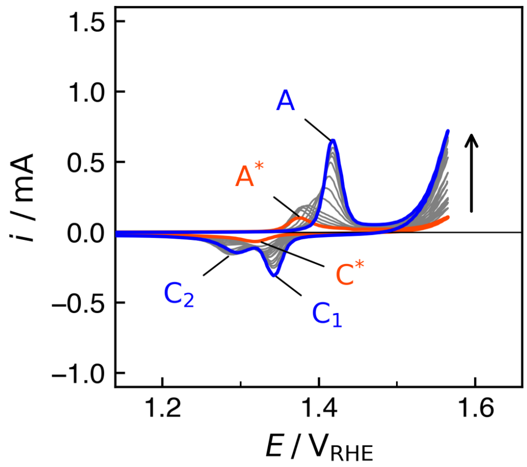

	Phase Transitions
A^*	$\alpha\text{-Ni(OH)}_2 \cdot H_2O \longrightarrow \gamma\text{-NiOOH} \cdot H_2O$
A	$\beta\text{-Ni(OH)}_2 \longrightarrow \beta\text{-NiOOH}$
C^*	$\gamma\text{-NiOOH} \cdot H_2O \longrightarrow \alpha\text{-Ni(OH)}_2 \cdot H_2O$
C_1	$\gamma\text{-NiOOH} \cdot H_2O \longrightarrow \beta\text{-Ni(OH)}_2$
C_2	$\beta\text{-NiOOH} \longrightarrow \beta\text{-Ni(OH)}_2$

Figure 6.7: Summary of phase transitions referenced in this work and their corresponding peaks. Cyclic voltammogram is a reprint of the data presented in Figure 6.2(d)

responses change, as shown in Figure 6.2. The β-redox pair is the dominant surface process for electrodes with a low switching potential (1.51, 1.53, and 1.55 V).[22] At switching potentials of 1.57 V or higher, the C_2 peak corresponding to γ-NiOOH develops considerably more than the β-NiOOH peak, indicating that higher switching potentials lead to preferential formation of the γ-NiOOH phase. The process of overcharging an electrode is proposed to drive the transformation of β-NiOOH to γ-NiOOH, corroborating this claim.[23]

For all switching potentials, a net increase in the maximum OER current (occurring at the switching potential) was seen, as indicated by the vertical arrow in each plot of Figure 6.2. The improvement in OER current with cycle number can be explained by an increase in ECSA caused by roughening of the surface, as well as varying activities between the different β-NiOOH phases. The act of cycling a Ni electrode between the various (oxy)hydroxide phases induces lattice expansion and contraction.[22] The mechanical stress leads to cracks and faults in the oxide layer, exposing fresh, active Ni sites.[114] Moreover, it is suggested that place-exchange processes will occur in parallel with the OER at high potentials, leading to structural rearrangement and surface roughening.[107–109]

In Figure 6.3a, the cyclic voltammogram data is normalized by the ECSA to more readily compare the wave features. Here, the onset potential of the Ni oxidation reaction is approximately constant for switching potentials up to 1.57 V. For E_λ of 1.59 and 1.61 V, there is a negative shift in onset potential. The increased formation of γ-NiOOH that occurs at higher switching potentials provides more γ-NiOOH upon reduction, leading to a decrease in onset potential.[26] The area of the oxidation wave is approximately constant, indicating that system reversibility is similar for all switching potentials. In Figure 6.3b, two major peaks are identified: the reduction of β-NiOOH to β-Ni(OH)$_2$ at 1.30 V and the reduction of γ-NiOOH to either β-Ni(OH)$_2$ or α-Ni(OH)$_2$ near 1.35 V. The ratio of γ-NiOOH to β-NiOOH increases with switching potential, consistent with electrode overcharge.

6.4.2 Oxygen Evolution

To examine the effect of switching potential on electrocatalytic properties, oxygen evolution kinetics were measured using three benchmark parameters: Tafel slope (b), overpotential (η), and turnover frequency (TOF). The first benchmark, Tafel slopes, were evaluated using EIS data, along with the following equation:[120]

$$\log\left(\frac{1}{R_{\mathrm{ct}}}\right) = \frac{\eta}{b} + \log\left(\frac{2.303 i_0}{b}\right) \tag{6.1}$$

A plot of the inverse log of charge-transfer resistance vs. overpotential yields a slope equal to the inverse of the Tafel slope. In Figure 6.8, Nyquist plots for a range of biases along with a Tafel plot are presented for an electrode developed with a switching potential of 1.51 V. The Tafel slopes for all switching potentials are also tabulated. Although decreasing slightly from 44.2 to 39.1 mV dec^{-1} with increasing switching potential, the Tafel slopes are approximately constant, indicating that a change in mechanistic rate-determining step is unlikely.[115, 121] As discussed in Chapter 5 an OER Tafel slope of $\sim$ 40 mV dec^{-1} can arise from one of two

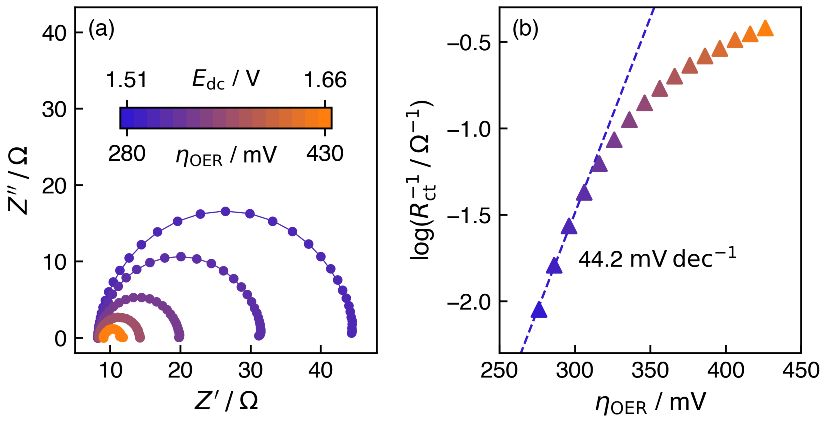

E_λ/ V	b / mV dec^{-1}
1.51	44.2
1.53	43.2
1.55	40.7
1.57	38.2
1.59	38.7
1.61	49.1

Figure 6.8: (a) Nyquist plots for EIS conducted between 1.51 and 1.61 V (select plots shown) and (b) Tafel plot constructed using R_{ct} from equivalent circuit fits for an electrode developed with a switching potential of 1.51 V. (Table) Tafel slopes evaluated using the same procedure for the remaining switching potentials.

possible rate-determining steps:[28]

$$\mathrm{MO} + \mathrm{OH}^- \rightleftarrows \mathrm{MOOH} + \mathrm{e}^- \tag{6.2}$$

$$\mathrm{MOO}^- \rightleftarrows \mathrm{M} + \mathrm{O}_2 + \mathrm{e}^- \tag{6.3}$$

While identification of the exact step is outside the scope of this work, the results presented here show good agreement with Tafel slopes estimated in the microkinetics analysis conducted by Shinagawa *et al.*, as well as the data presented in Chapter 5.[28]

To further quantify the OER kinetics as a function of switching potential, overpotentials were calculated for two conditions and are presented in Figure 6.9(a); the first, η_{ons}, corresponds to the onset overpotential of OER, measured at 0.5 mA $\mathrm{cm}_{\mathrm{geo}}^{-2}$ tangent, as described in Chapter 3. The second, η_{10}, is the overpotential required to generate 10 mA $\mathrm{cm}_{\mathrm{geo}}^{-2}$ of OER current, an often-used metric for water splitting devices.[38] To estimate η_{10}, the charge-transfer coefficient was first calculated from the Tafel slope:

$$\alpha = \frac{RT}{nFb} \tag{6.4}$$

The current-potential data was then fit to the anodic Butler-Volmer equation:

$$j_{\mathrm{a}} = j_0 \cdot \exp\left(\frac{(1-\alpha)nF}{RT}\eta\right) \tag{6.5}$$

and extrapolated to the overpotential corresponding to 10 mA $\mathrm{cm}_{\mathrm{geo}}^{-2}$. Both overpotentials generally increase with switching potential; the value of η_{ons} increases from 260 to 322 mV, while η_{10} trends from 322 to 399 mV.

Turnover frequency (TOF) is presented for each switching potential in Figure 6.9(b), evaluated using the site densities shown in Figure 6.9(c). The TOF values were calculated at potentials of 1.56 and 1.66 V after a hold of 3.5 minutes. In the low switching potential range (1.51–1.53 V), TOF values were high, ranging between 10–18 s^{-1}. As the switching potential increased, TOF values decreased. At switching potentials of 1.59 and 1.61 V, the TOF values were only between 0.57–3.5 s^{-1}.

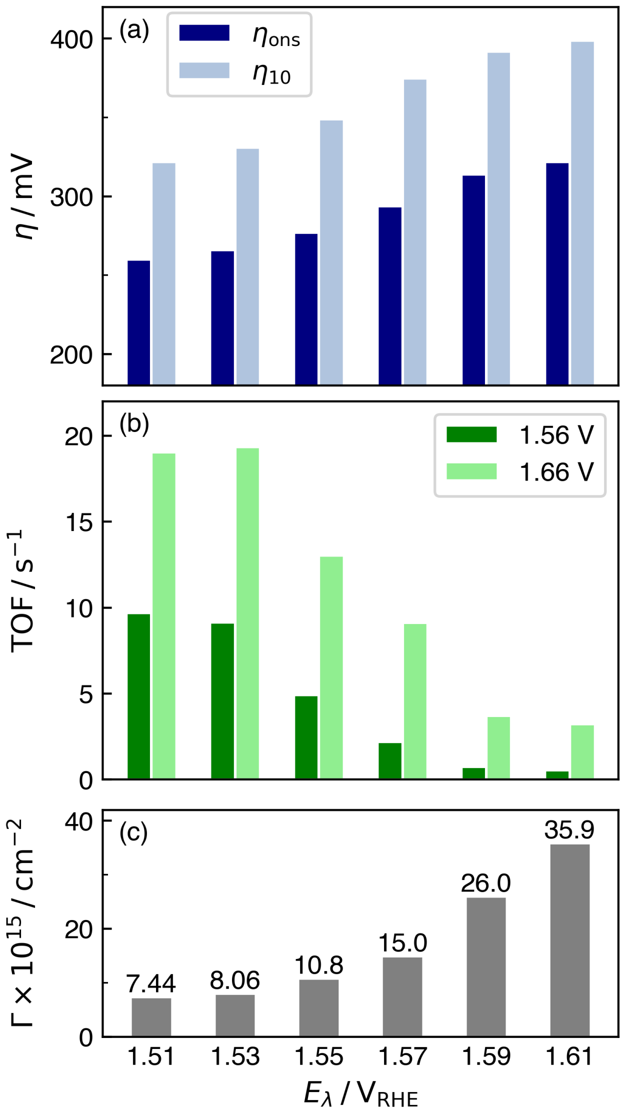

Figure 6.9: (a) The OER onset overpotential and theoretical overpotential required to reach 10 mA cm_{geo}^{-2} of OER current as a function of E_λ. (b) TOF evaluated at 1.56 and 1.66 V as a function of E_λ using Equation 5.1. (c) Site density of NiOOH.

In conjunction with the potentiostatic hold data of Figure 6.4, the TOF values indicate that the OER occurs at much shorter time scales compared with the duration of the potentiostatic hold data. For example, the initial decay in current in Figure 6.4 has a time constant of approximately 10 minutes, while the long-term rise occurs on the order of 4 hours or longer. With OER turnover frequencies of 9.2–19 s^{-1} for $E_\lambda = 1.53$ V and 0.57–3.7 s^{-1} for $E_\lambda = 1.61$ V, it is clear that, for even the lowest TOF, OER active sites are turned over at least 600 times during the 10-minute time constant for the short-term decrease and at least 10,000 times for the time constant of the long-term increase. The interpretation here is that OER kinetics are much faster than those for the processes responsible for the potentiostatic hold features in Figure 6.4. We conclude, therefore, that changes in surface structure brought about by potential cycling remain in the OER region, by which OER current can serve as a measure of the activity of these surfaces. Thus, the higher OER current in Figure 6.4 for the β-NiOOH surface formed at $E_\lambda = 1.53$ V reflects a higher OER activity than that of the β-NiOOH surface formed at $E_\lambda = 1.61$ V.

Moreover, the current increase after the initial decay indicates an improvement of the catalyst surface over time, presumably due to an increase in active sites. Alternatively, an additional electrochemical reaction made more favorable by the constant bias application may be occurring. The formation of alternative Ni-species at higher potentials has been suggested, including a β-phase that forms through the direction oxidation of Ni sublayers, as well as a higher oxidation state β-phase that is not equivalent to γ-NiOOH.[122] At this time, there is little evidence to support an additional electrochemical reaction and the simplest explanation supported by these results is an increase in active sites.

6.4.3 Electrochemical Impedance Spectroscopy

From the Nyquist plots shown in Figure 6.5 and the extracted parameters in Table 6.1, it is clear that the switching potential has a direct impact on the electrode's behavior. The value of R_{ct} increases by almost a factor of 3 with switching potential. As the charge-transfer resistance measures the ratio of overpotential to current, making it a convenient index of a reaction's kinetics.[48] For a given overpotential, a low value of R_{ct} — as seen for a switching potential of 1.51 V — indicates a higher resulting Faradaic current and a more active surface. The results here support the original claim that the β-NiOOH surface is the more-active phase for the OER due to its lower charge-transfer resistance.

The effective capacitance (C_{eff}), is an estimation of an electrode's double layer capacitance and its corresponding capacity for charge-transfer.[48, 64, 65] In general, a larger effective capacitance indicates a higher electrochemical surface area. From the values shown in Table 6.1, the electrochemical surface area increases from 13.9 cm^2 (R_{f} = 19.6) to 23.0 cm^2 (R_{f} = 32.4), an increase by a factor of approximately 1.7. These results are consistent with the proposed surface-roughening process that occurs at higher switching potentials.

6.4.4 Morphology

The distribution of facet sizes and number of grain boundaries changed between the initial and developed oxide layers, as seen in Figure 6.6. A mixture of roughened (jagged) and faceted (straight) boundaries was observed before oxide development (Figure 6.6a).[117, 123] The oxide growth procedure altered the surface *via* growth of dominant facets and formation of grain boundaries. During the growth of a dominant facet, the surface energy level reached a minimum as lower-energy crystals covered the surface. [33, 124] The dominant facet growth explains the large facet planes seen in Figure 6.6b. However, the oxide-growth procedure introduced roughening of the surface by forming more grain boundaries at a higher switching potential, as seen by the differences between Figure 6.6b and c. The increase in grain boundaries may also explain the increase in surface sites during oxide growth among different E_λ, as seen in Figure 6.2. Thus, the oxide growth procedure was able to decrease or increase the density of grain boundaries by allowing the surface to minimize its surface energy or by roughening the surface, respectively.

6.5 Conclusions

The electrochemical development of NiOOH species through potential cycling in alkaline media was studied as a function of switching potential. The influence of switching potential on oxide composition and oxygen evolution kinetics was quantified using EIS and Tafel analysis, while the surface morphology was studied using SEM. From these results, the following conclusions were drawn:

- At high switching potentials, increased overcharge and surface roughening leads to an increase in electrochemical surface area and number of NiOOH sites.
- Switching potential can be used to control the formation of β-NiOOH (low E_λ) and γ-NiOOH (high E_λ), enabling their effect on OER to be probed.
- The β-NiOOH phase has improved OER kinetics compared to the γ-NiOOH, as the overpotentials are lower and turnover frequencies are higher. Furthermore, the improved kinetics last over a prolonged period when compared to γ-NiOOH.
- Increasing the switching potential from 1.51 to 1.61 $\mathrm{V_{RHE}}$ decreases facet size and increases the number of grain boundaries.

Chapter 7

FLOW FIELD PATTERN OPTIMIZATION FOR DIALYSATE REGENERATION USING COMPUTATIONAL FLUID DYNAMICS

7.1 Context

While the kinetics of the urea oxidation reaction are primarily researched for wastewater treatment and direct urea fuel cell applications, the UOR is also of great interest to the medical field; the electrochemical oxidation of urea provides an attractive improvement to the current state of dialysis. Currently, over two million people worldwide suffer from end stage renal disease (ESRD), with almost 750,000 of those patients residing in the United States alone. Comprising 7.2% of overall Medicare-paid claims, treatment for ESRD can cost a patient up to $72,000 per year.[125]

The physical and psychological hurdles that come with dialysis are often cited as being a more influential factor than the financial burden when determining treatment; while the cost of treatment was ranked ninth in importance during a study of dialysis outcomes, the ability to travel was ranked second.[126] The dialysis process occurs three to four times a week for four hours at a time, and requires the patient to be present at a dialysis center. Due to this intermittent treatment, rapid fluctuations of toxins in the body and consistent buildup of waste materials between sessions are common.[126] Consequentially, patients often report fatigue, anemia, and cramps after standard hemodialysis treatment. While the rate of new ESRD cases has declined due to advancements in kidney failure prevention and postponement, the quality of life improvements for those already on hemodialysis leaves much to be desired. One study on the high morbidity and mortality rates of ESRD reports that “an average patient would be willing to give up 10 years of life on dialysis in exchange for

4 years with normal kidney function".[125] Some studies have indicated that more frequent - but shorter - treatments improve overall patient quality of life. A major improvement in the field of hemodialysis is home-use devices, which can be run overnight and allow improved recovery times and patient outcomes. The ultimate goal for dialysis devices, however, is one that does not tether the patient to any particular location.

Hemodialysis is currently the most common treatment method for ESRD, where a patient's blood is filtered past a semi-permeable membrane to remove waste products that the patient's body is incapable of removing on its own, as shown in Figure 7.1(left). On the other side of the membrane passes dialysate fluid, which carries waste products away from the patient and is ultimately discarded. In typical hemodialysis, between 300 and 900 liters of water are spent as dialysate fluid per week, per patient, depending on the severity of renal disease.

The concept of a portable dialysis device relies on the ability to regenerate dialysis fluid. To "clean" dialysate fluid for continuous use, major toxins need to be removed. The primary component of spent dialysate fluid is urea, which builds up in the body due to decreased kid-

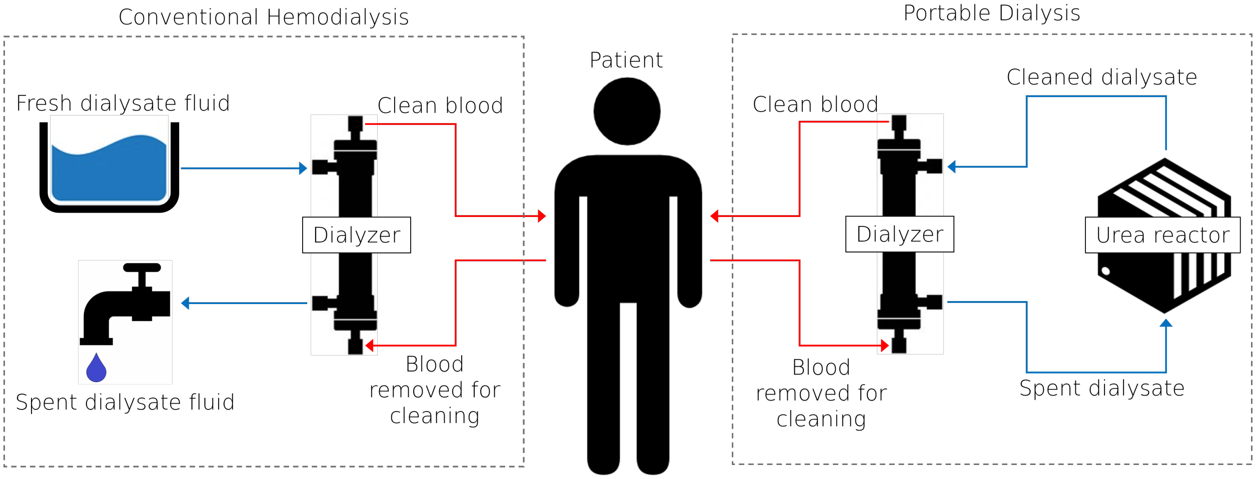

Figure 7.1: Comparison of (left) conventional hemodialysis and (right) a proposed portable dialysis system.

ney function. While only mildly toxic, urea is the largest constituent of urine, and significant buildup during kidney failure leads to uremia.[127] Electrochemical oxidation is an attractive option for urea removal in a portable dialysis system because of its small form factor, low-energy cost, and manageable byproducts.[12, 43, 47, 113] In a regenerative system, spent dialysate is pumped from the dialyzer to the urea reactor, as shown in Figure 7.1(right). Here, urea and other organics such as creatinine and glucose are oxidized to form nitrogen and carbon dioxide, with hydrogen as a potential byproduct. These gaseous products can be removed using a degasser, and the now cleaned dialysate fluid can be returned to the dialyzer in a closed-loop system. With efficient toxin removal, only a small amount of dialysate fluid would be needed, allowing for a portable system that could be transported in a suitcase or backpack.

A schematic of a urea removal device (URD) is shown in Figure 7.2. From left to right, the components are the anode flow field plate ($\mathrm{FFP_a}$), the anode gas diffusion layer ($\mathrm{GDL_a}$), the anion exchange membrane (AEM), the cathode gas diffusion layer ($\mathrm{GDL_c}$), and the cathode flow field plate ($\mathrm{FFP_c}$). During operation, urea-containing dialysate fluid is fed to the anode side of the URD, where it is distributed by a flow field plate (FFP). Each FFP has a pattern etched into the surface, providing channels for solution to flow across the gas diffusion layer (GDL). The GDL is generally a porous, high surface area material such as carbon cloth or carbon paper with an electrocatalyst deposited on the surface. When urea comes in contact with the electrocatalyst, it is chemically oxidized:

$$\mathrm{CO(NH_2)_2} + 6\,\mathrm{OH^-} \longrightarrow \mathrm{N_2} + \mathrm{CO_2} + 5\,\mathrm{H_2O} + 6\,\mathrm{e^-} \tag{7.1}$$

The product N_2 and CO_2 are removed from the system using a degasser, and the dialysate fluid is either returned to the dialyzer or fed back into the URD. On the cathode side, either water or humidified O_2 (not shown) can be fed to the URD. When water is fed, the URD acts as an electrolyzer, forming H_2:

$$2\,\mathrm{H_2O} + 2\,\mathrm{e^-} \longrightarrow \mathrm{H_2} + 2\,\mathrm{OH^-} \tag{7.2}$$

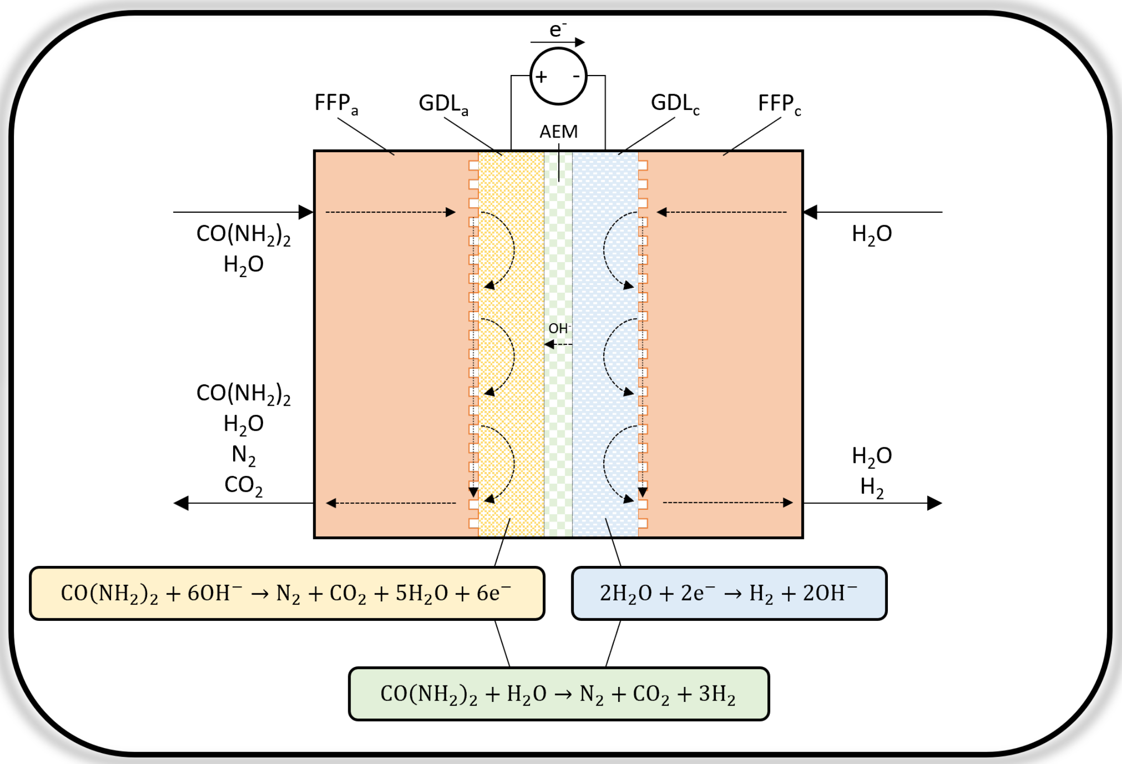

Figure 7.2: Schematic of the urea removal device.

The overall chemical equation for the URD in this configuration is:

$$\mathrm{CO(NH_2)_2 + H_2O \longrightarrow N_2 + CO_2 + 3\,H_2} \tag{7.3}$$

When humidified O_2 is fed to the cathode, the URD acts as a fuel cell with the following cathode half-cell and overall reactions:

$$\mathrm{O_2 + 2\,H_2O + 4\,e^- \longrightarrow 4\,OH^-} \tag{7.4}$$

$$\mathrm{2\,CO(NH_2)_2 + 3\,O_2 \longrightarrow 2\,CO_2 + 2\,N_2 + 4\,H_2O} \tag{7.5}$$

There are a considerable number of challenges with dialysis-focused urea oxidation, and research has been ongoing since the early 1970s [43]. The sluggish reaction rate of the UOR limits the rate of urea decomposition, and the low urea concentration in the dialysate fluid (∼0.01 M) makes efficient removal all the more difficult. One approach to increase the removal rate is by improving the mass transfer of urea molecules to the electrocatalyst surface through use of specialized flow field patterns. In this chapter, the effect of flow field design on the efficiency of urea oxidation is investigated using the computational fluid dynamics (CFD) software COMSOL Multiphysics®.

7.2 Experimental

7.2.1 Model Representation

A 3-D representation of a flow field plate with an example serpentine pattern is shown in Figure 7.3(left). Here, solution flows into the channel with flow rate v_o and concentration $c_{0,\text{r}}$ at the top left, winds through the serpentine flow pattern, and exits at the bottom right. The

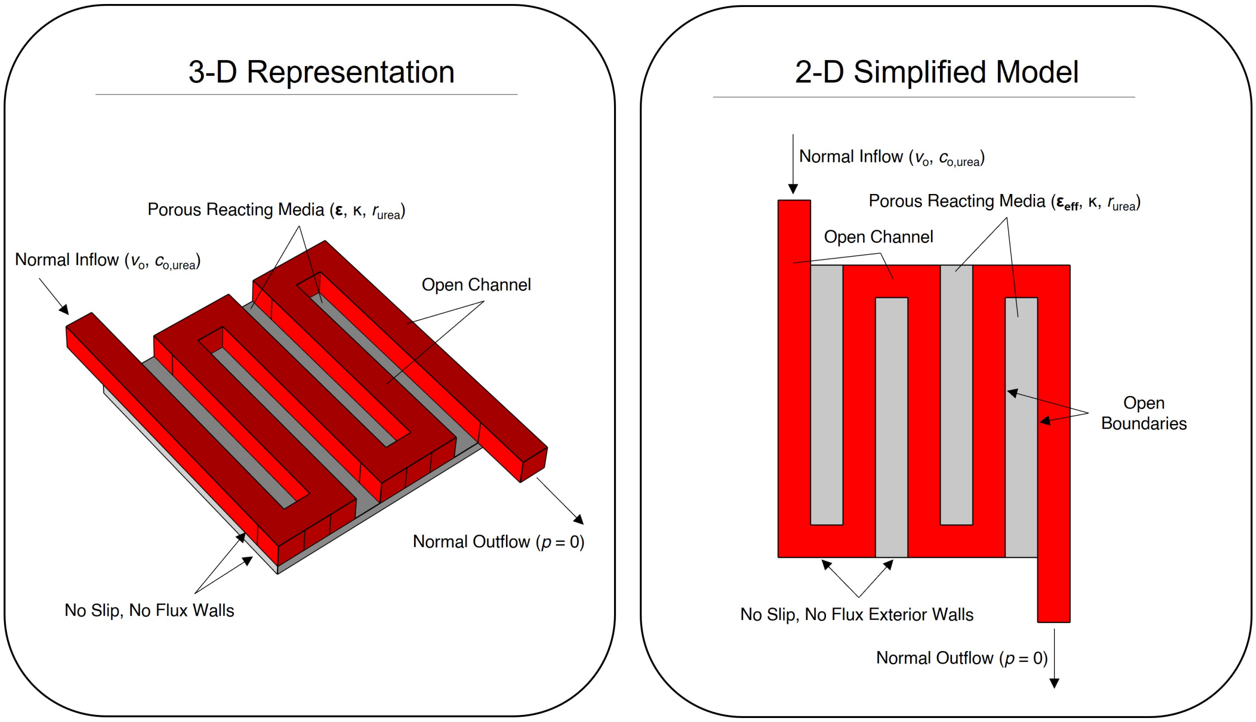

Figure 7.3: A (left) 3-D and (right) 2-D representation of a serpentine flow field pattern including the relevant boundary, flow, and reaction conditions

side and top walls for this chamber have no-slip and no-flux conditions, while the bottom of the chamber is an open boundary condition. Solution can leave through this open boundary and enter the porous reacting media (GDL). The GDL has a set porosity (ϵ), permeability (κ), and homogenized urea reaction rate (r_{u}).

In general, a 3-D representation will result in the most accurate simulation due to its ability to simultaneously model reactant flow in the direction of the flow channel and perpendicular to the flow channel (into the GDL). The number of finite elements needed to simulate an accurate 3-D model, however, will be orders of magnitude higher than a 2-D simulation, resulting in a computationally expensive process. For that reason, a 2-D depth-averaged model was developed to reduce simulation time, as shown in Figure 7.3(right). For the 2-D simplified model to be possible, a number of assumptions have to be made:

- The interior boundaries — where the red channels meet the gray porous media — are open boundaries such that fluid can flow between them.

- An effective porosity is used (ϵ_{eff}) — calculated by scaling the actual porosity by the ratio of GDL height to total height — to correct for the differing heights of the flow channel and the GDL.

- The porous reacting media volume that is present below the flow channels in the 3-D representation is neglected in the 2-D representation. The majority of electrochemical oxidation is assumed to occur in the ribs separating the channel, and thus the neglected volume will have minimal impact on the simulation results.

In previous studies, these assumptions have been shown to minimally impact the simulation's accuracy, as seen in Figure 7.4.[128] According to Zhang *et al.*, a 2-D, depth-averaged model using similar flow field deigns and flow conditions will result in similar pressure drops as an equivalent 3-D model and in experiments. The 2-D results tended to differ from experimental data at high flow rates for the interdigitated design and at low flow rates for the serpentine design, suggesting the 2-D depth averaged model may have a valid range, however.

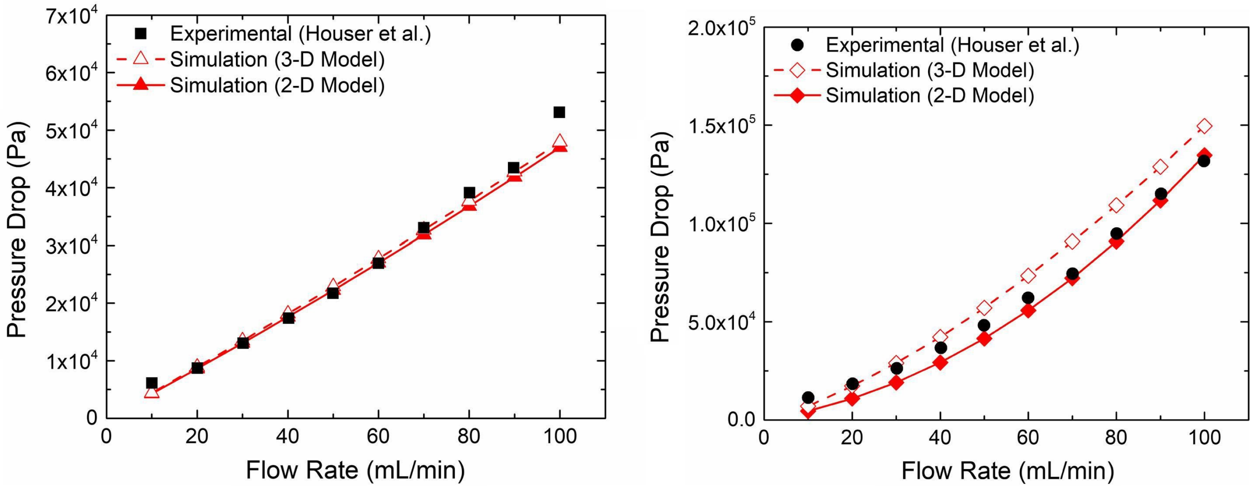

(a) Interdigitated (b) Serpentine

Figure 7.4: Comparison of simulated 3-D and 2-D pressure drops with experimental data for an (a) interdigitated and (b) serpentine flow field pattern†

7.2.2 Mathematical Methods

In both the channel and porous media, the continuity equation is expressed as:

$$\rho \boldsymbol{\nabla} \cdot \mathbf{u} = 0 \tag{7.6}$$

where ρ is the fluid density ($\mathrm{kg\,m^{-3}}$) and $\mathbf{u}$ is the velocity vector ($\mathrm{m\,s^{-1}}$). The single-phase, laminar fluid velocity and pressure gradient are solved using the Navier-Stokes and Brinkman equations for channel flow and porous media flow, respectively:

$$\text{Channel:} \qquad \rho(\mathbf{u}\cdot\nabla)\mathbf{u} = \boldsymbol{\nabla}\cdot[-p\mathbf{I} + \mu(\nabla\mathbf{u} + (\nabla\mathbf{u})^T)] \tag{7.7}$$

$$\text{GDL:} \qquad \frac{\rho}{\epsilon^2}(\mathbf{u}\cdot\nabla)\mathbf{u} = \boldsymbol{\nabla}\cdot[-p\mathbf{I} + \frac{\mu}{\epsilon}(\nabla\mathbf{u} + (\nabla\mathbf{u})^T) - \frac{2}{3}\frac{\mu}{\epsilon}(\boldsymbol{\nabla}\cdot\mathbf{u})\mathbf{I}] - \frac{\mu}{\kappa}\mathbf{u} \tag{7.8}$$

where p is the pressure (Pa), μ is the dynamic viscosity of the fluid ($\mathrm{kg\,m^{-1}\,s^{-1}}$), ϵ is the porosity of the gas diffusion layer, and κ is the permeability of the gas diffusion layer ($\mathrm{m^{-2}}$).

---

†Reprinted from *International Journal of Heat and Mass Transfer*, Vol 135, Zhang, Lei, Bai & Zhao, *A two-dimensional model for the design of flow fields in vanadium redox flow batteries*, 460-469, Copyright

The mass conservation equation is used to model the diffusive and convective transport of a chemical species (i) in the channel and porous media:

$$\text{Channel:} \qquad \boldsymbol{\nabla} \cdot (-D_{\mathrm{i}} \nabla c_{\mathrm{i}}) + \mathbf{u} \cdot \nabla c_{\mathrm{i}} = 0 \tag{7.9}$$

$$\text{GDL:} \qquad \boldsymbol{\nabla} \cdot (-\epsilon^{4/3} D_{\mathrm{i}} \nabla c_{\mathrm{i}}) + \mathbf{u} \cdot \nabla c_{\mathrm{i}} = r_{\mathrm{i}} \tag{7.10}$$

where D is the diffusion coefficient ($m^2\ s^{-1}$), c is the concentration ($\mathrm{mol\,m^{-3}}$), and r is the reaction rate expression ($\mathrm{mol\,m^{-3}\,s^{-1}}$).

The electrochemical reaction rate was estimated using a Tafel kinetics model of the following form:[129]

$$j_{\mathrm{i}} = j_{0,\mathrm{i}}\,(c_{\mathrm{i}})^{a} \exp{(bE)} \tag{7.11}$$

where j is the current density ($\mathrm{A\,m^{-2}}$), j_0 is the exchange current density ($\mathrm{A\,m^{-2}}$), a is the concentration dependence order, b is the potential response constant ($\mathrm{V^{-1}}$), and E is the applied potential ($\mathrm{V_{SHE}}$). The current density was converted to a homogenized, porous-medium chemical reaction rate using the following equation:

$$r_{\mathrm{i}} = \frac{j_{\mathrm{i}}}{nF} \times SSA \tag{7.12}$$

where n is the number of electrons exchanged (6), F is the Faraday constant (96485 $\mathrm{C\,mol_{e^-}^{-1}}$), and SSA is the specific surface area of the gas diffusion layer ($\mathrm{m^{-1}}$), estimated using the following equation:[130]

$$SSA = \sqrt{\frac{\epsilon^3}{2\kappa}} \tag{7.13}$$

A summary of the relevant geometries, flow conditions, and electrochemical parameters are presented in Table 7.1.

7.2.3 Flow Field Patterns

Many of the flow patterns in this study are commonly used in industry and research and generally fall into one of four flow channel groups: single, split, interdigitated, or mixed.[131–135] The designs used during the initial computational studies are presented in Figure 7.5.

2019, with permission from Elsevier.

Table 7.1: Mathematical constants and variables used for computational modeling of flow fields.

Parameter	Variable	Value	Unit
Width of Gas Diffusion Layer	w_{gdl}	22	mm
Height of Gas Diffusion Layer	h_{gdl}	0.4	mm
Width of Flow Channel	w_{ch}	1	mm
Height of Flow Channel	h_{ch}	1	mm
Porosity of Gas Diffusion Layer	ϵ	0.5	
Permeability of Gas Diffusion Layer	κ	3.0×10^{-12}	m^2
Specific Surface Area	SSA	1.44×10^{-5}	m^{-1}
Reference Temperature	T_{ref}	293.15	K
Reference Pressure	P_{ref}	1	atm
Fluid Density	ρ	1000	$\mathrm{kg\,m}^{-3}$
Fluid Dynamic Viscosity	μ	1.01×10^{-3}	$\mathrm{kg\,m}^{-1}\,\mathrm{s}^{-1}$
Diffusion Coefficient of Urea in Water	D_{u}	1.382×10^{-9}	m^2
Inlet Concentration of Urea	$c_{0,\mathrm{u}}$	0.010	M
Exchange current density of the UOR[129]	$j_{0,\mathrm{u}}$	0.028	$\mathrm{A\,m}^{-2}$
Reaction Order of the UOR[129]	a	0.216	
Potential Response Constant[129]	b	3.25	V^{-1}
Number of electrons	n	6	$\mathrm{mol}_{\mathrm{e}^-}$
Volumetric Flow Rate	$\dot{V}$	10	$\mathrm{mL\,min}^{-1}$
Applied Potential	E	1.5	$\mathrm{V}_{\mathrm{RHE}}$

Single flow channels including the serpentine, multi-serpentine, and spiral patterns consist of a single, unbroken channel (red) that extends from the inlet (top left) to the outlet (bottom

(a) Serpentine (b) Multi-Serpentine (c) Spiral

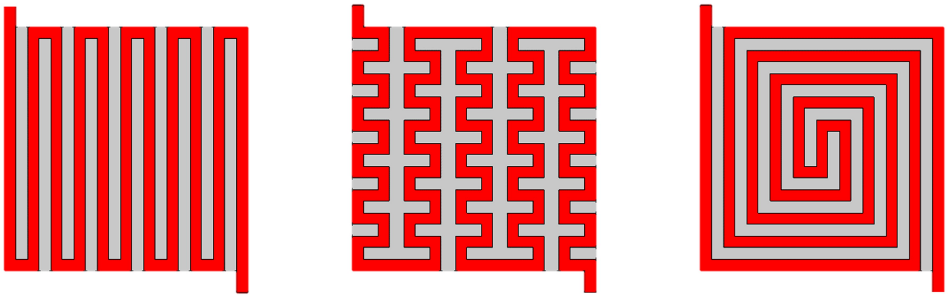

(d) Parallel (e) Murray-Parallel (f) Grid

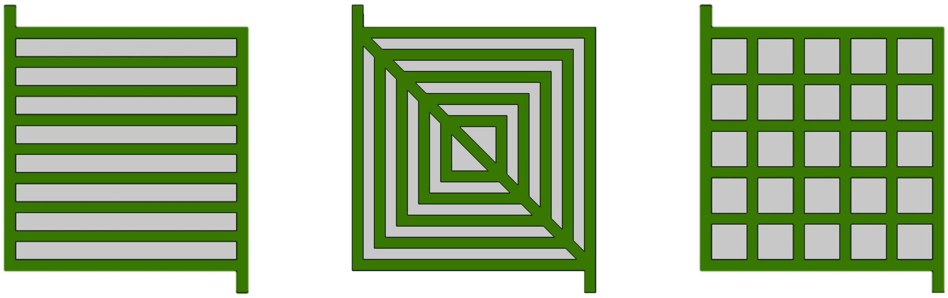

(g) Interdigitated (h) Leaf (i) Constructal

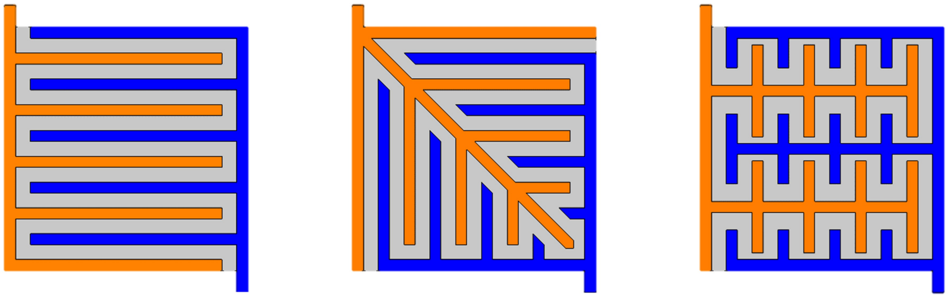

(j) Parallel-Serpentine (k) Interdigitated Spiral (l) Interdigitated-Serpentine

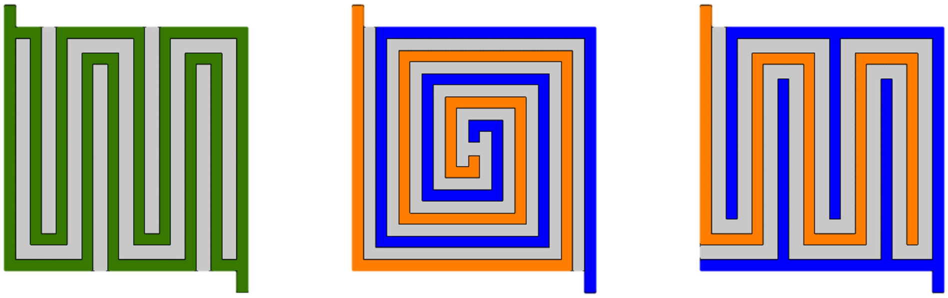

Figure 7.5: Flow field patterns modeled during initial analysis.

right). The serpentine style channel (Figure 7.5(a)) is an industry standard due to its robust performance and product removal.[133] The single, winding channel maximizes coverage of the GDL. While this causes a high pressure-drop across the active area and an increase in pumping requirements, the pressure drop is necessary for good under-rib (porous-media) flow, and generally results in good overall performance. The single channel, however, leads to poor reactant distribution across the GDL. Other single-channel designs are often used for specific applications; the multi-serpentine design (Figure 7.5(b)) increases the number of channel bends, improving reactant distribution, while spiral channels (Figure 7.5(c)) have been shown to generate local, secondary vortices that help distribute heat and mass across the GDL.[133, 136]

Split flow channels such as the parallel, Murray-parallel, and grid patterns also directly connect the inlet and outlet points, but do so through numerous channels (green). The parallel design is another industry standard for applications where high pressure-drops are not acceptable; less flow-per-channel reduces the pressure drop of the FFP and also provides a more uniform reactant distribution.[137] Low pressure-drops will reduce the amount of under-rib flow, however, reducing cell performance. Additionally, blockages occurring in a parallel design channel will cause a redistribution of flow to the other channels, resulting in the formation of a dead zone. Additional types of split flow designs are the Murray parallel and grid patterns. Similar to the standard parallel, these designs trade performance for a reduced pressure drop, but the two-dimensional directions of the channels results in a more robust plate that is less affected by blockages.[133]

Interdigitated patterns (Figure 7.5(g-i)) are defined by a disconnected inlet (orange) and outlet (blue) channels. These types of flow patterns can take on a number of designs, but generally have a series of alternating inlet-outlet branches that dead-end. The traditional interdigitated design (Figure 7.5(g)) has a single inlet manifold with “fingers” that stretch away perpendicularly towards the outlet manifold. The interlocking fingers force reactant flow through the GDL, resulting in efficient conversion and product removal. While the forced under-rib leads to sharp increases in pressure-drop, the use of relatively short channels results in values similar to that of a serpentine design. Interdigitated plates often mimic biological systems through the use of fractal designs, including the leaf pattern (Figure 7.5(k) and constructal pattern (Figure 7.5(i)). These patterns replicate the flow conduction systems that organically develop in the lungs, plants, and other biological structures. In general, the defining forced under-rib flow characteristic of interdigitated type patterns makes their efficacy significantly dependent on the physical characteristics of the GDL.[133]

Mixed patterns (Figure 7.5(j-l)) combine aspects of the flow groups to compensate for weaknesses in a specific design. Parallel-serpentine patterns (Figure 7.5(j)) have multiple channels that wind side-by-side from inlet to outlet. The resulting FFP sacrifices performance for a reduced pressure drop (compared to a traditional serpentine), but performs better than the standard parallel pattern. The interdigitated-spiral and interdigitated-serpentine combine disconnected inlet-outlet channels with the spiral and serpentine channel patterns, respectively. As with the traditional interdigitated patterns, the parameters of the GDL will dictate the efficacy of these designs, but generally result in a better distribution of reactants over the surface of the GDL.[133]

7.2.4 Mesh

A customized mesh was used for the CFD simulations, as shown in Figure 7.6. The base sizing for the elements was COMSOL's predefined "Extra Fine" sizing for a fluid dynamics physics, with element sizes ranging from 0.0033 mm to 0.286 mm. A free triangular mesh was used for the entire domain based on the previously defined element sizing. A corner refinement node was added to decrease the element size by a factor of 0.25 at sharp corners (vertices). Finally, a boundary layer node was added to create a dense element distribution along all boundaries in the channel and GDL domains. This node creates a 5-layer quadrilateral mesh on either side of the channel/GDL interface, the thickness of each stretched by a factor of 1.2 moving away from the boundary. The resulting mesh had 86 vertex elements, 1872 boundary elements, and 31810 total elements.

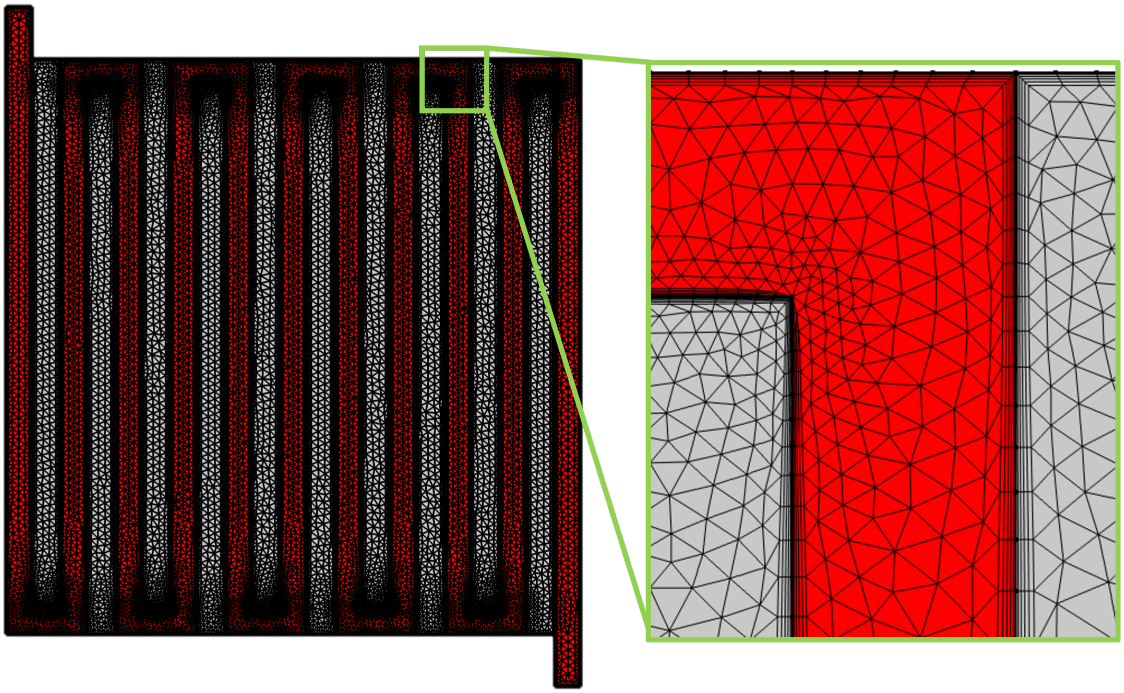

Figure 7.6: Meshing of (top) overall flow field pattern and (bottom) zoomed corner and boundary mesh.

7.3 Results and Discussion

As an initial test, a selection of flow field patterns were screened using the parameters listed in Table 7.1 and the patterns shown in Figure 7.5.

7.3.1 Single Channel Designs

The velocity, pressure, and concentration profiles of the single flow channel patterns are presented as streamline, contour, and surface plots, respectively, in Figure 7.7. The fluid velocity is roughly constant throughout the channel for all flow patterns. The exception is the spiral pattern, where the fluid velocity is low in the center of the flow field and increasing radially outward. Fluid velocity is lowest in the GDL for all patterns due to the low permeability and porosity, and generally flows in the same direction as the nearby

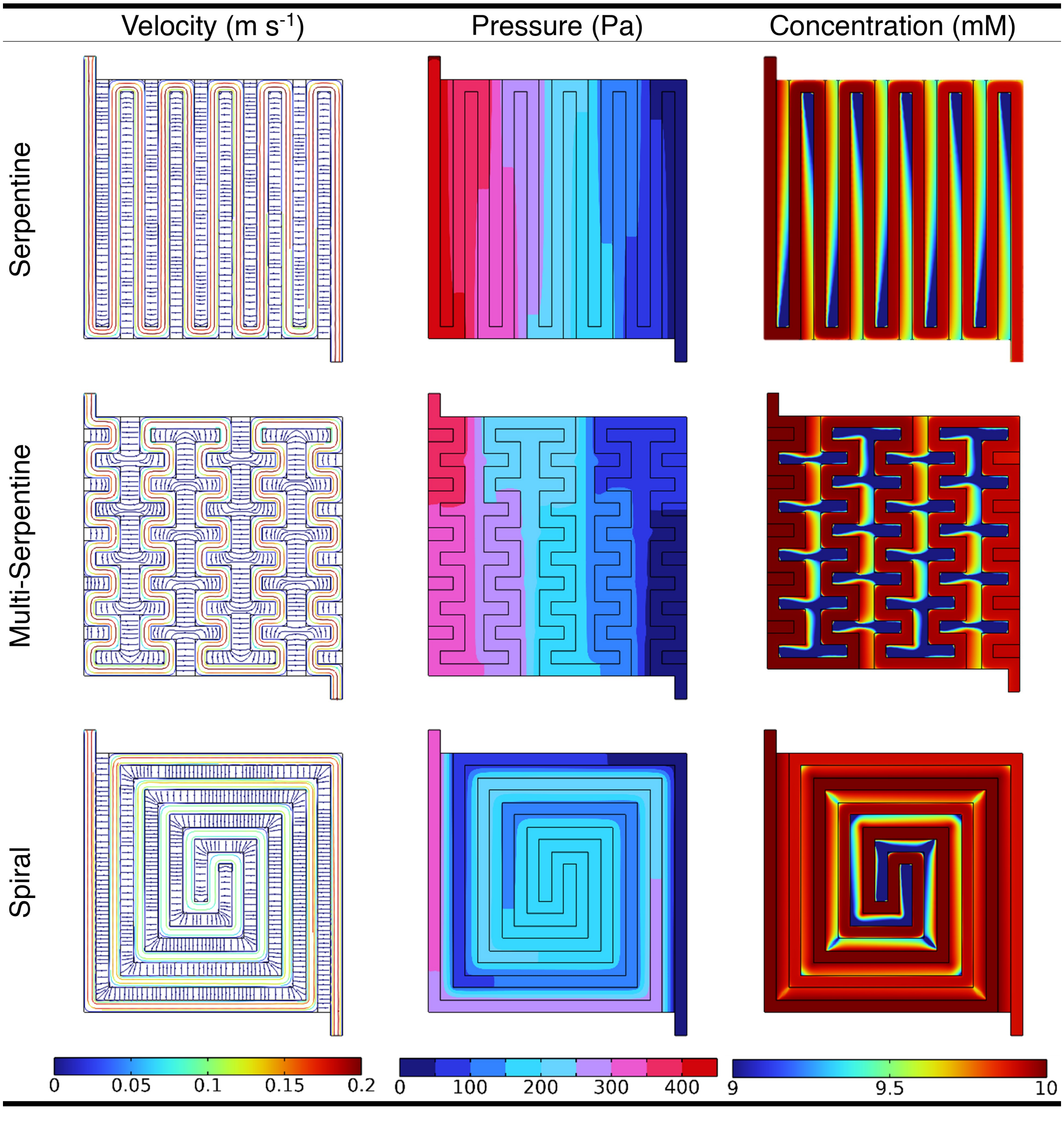

Figure 7.7: Velocity, pressure, and concentration profiles of the single flow patterns.

channels. Near sharp bends in the channels, local vortices form in the GDL due to the bidirectional channel flow. Subsequently, there is an increase in fluid residence time, and it is in these bends that the majority of electrochemical conversion of urea occurs. In the serpentine channels, for example, the lowest concentration of urea can be seen at the top and bottom of the ribs separating each channel. For the multi-serpentine flow, vortices form in the 4-way intersections between up-down and left-right flow, resulting in a curved urea concentration gradient. Of the single flow channels studied here, the spiral design results in the most even distribution, with just a small reactant “dead zone” at the center of the spiral. For all single flow channels, the pressure drops roughly follow the channel direction.

7.3.2 Split Channel Designs

Profiles for the parallel, Murray-parallel, and grid patterns are presented in Figure 7.8. For all the split flow designs, velocity is highest near the inlet and outlet manifolds, but slows considerably as the fluid is distributed throughout the split pathways across the active area. Correspondingly, the pressure drop is considerably lower than that of the single channel designs. The contours of the pressure drop also decrease from top-left to bottom-right in the direction of flow. Fluid flow inside the GDL is effectively unidirectional from inlet to outlet. The lower overall plate pressure provides less of a driving force for under-rib flow, resulting in what is effectively creeping flow from inlet to outlet. The concentration profiles of the split channel designs show that the GDL “pockets” are roughly symmetric across the flow field; a concentration gradient tends to form in the direction of flow, and the steepest gradient is present at the channel-GDL boundary. The lower flow rate of the split channel designs results in a significantly higher fluid residence time within the GDL. Consequently, reactant is depleted in the GDL, causing the formation of dead zones.

7.3.3 Interdigitated Channel Designs

Velocity, pressure, and concentration profiles for the interdigitated channel designs are shown in Figure 7.9. Similar to the split channel designs, the flow velocity is highest at the inlet and outlet manifolds, but drops as fluid is directed into the distribution branches. Due to the disconnected inlet and outlet branches, fluid is forced into the GDL. Unlike the split de-

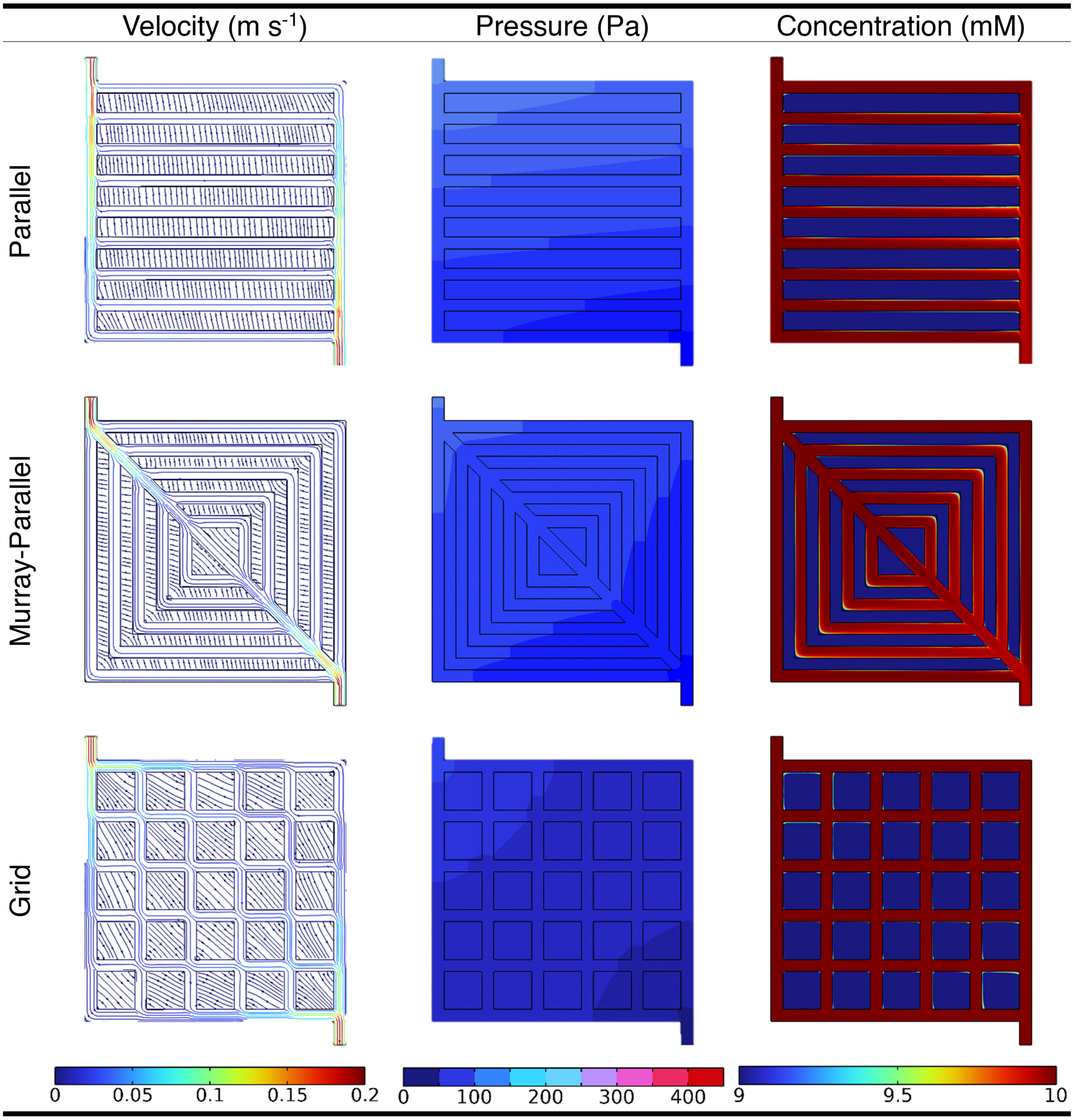

Figure 7.8: Velocity, pressure, and concentration profiles of the split flow patterns.

sign channels, however, fluid in an interdigitated design will generally take the shortest path through the GDL from inlet to outlet. Consequently, streamlines generally trend perpendic-

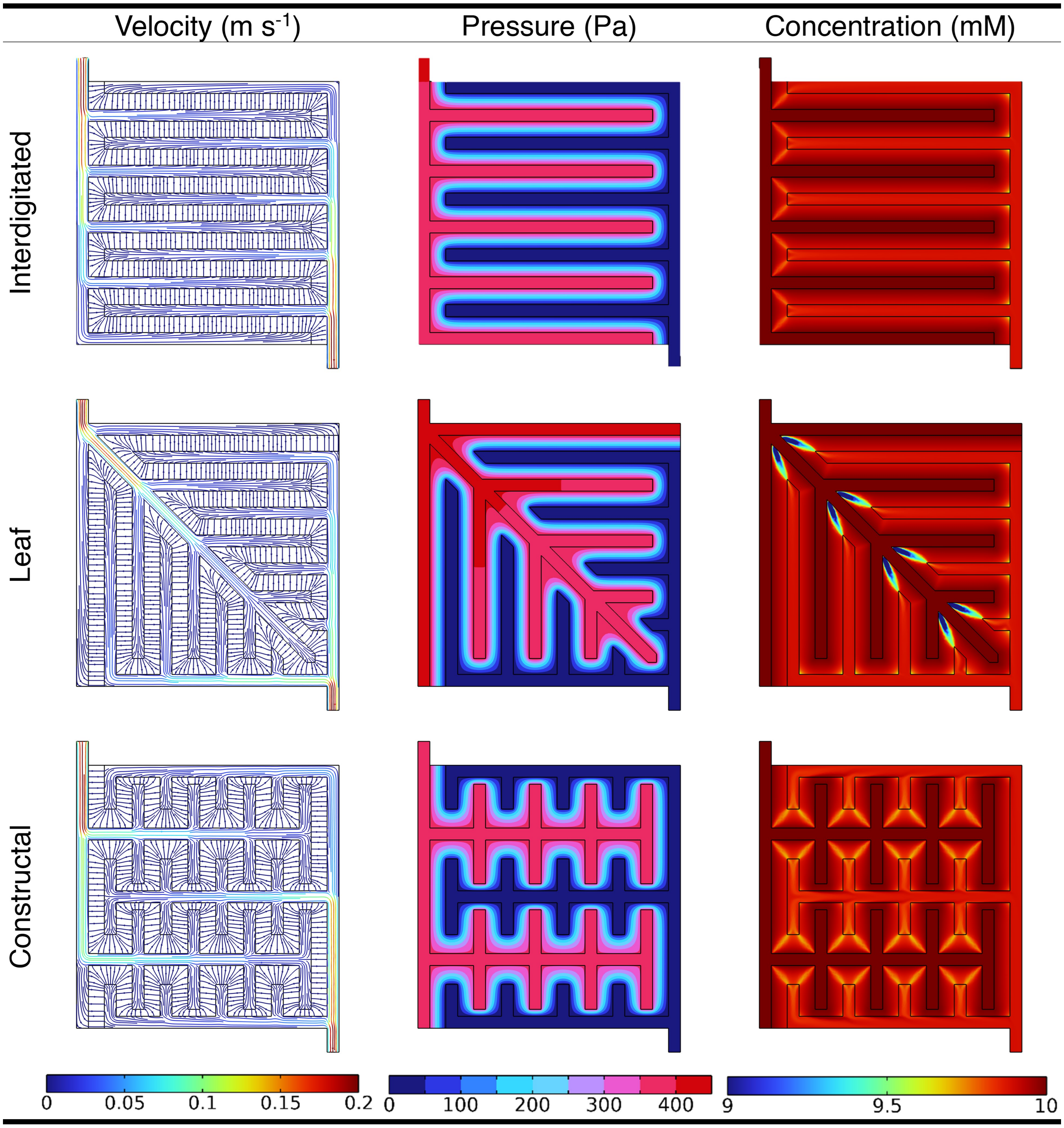

Figure 7.9: Velocity, pressure, and concentration profiles of the interdigitated flow patterns.

ularly from the inlet branches to the outlet branches. The exception to this is when fluid is near bends and corners of the branches; the longer diagonal distance between inlet and outlet branches causes curved streamlines to form in bends of the GDL. The disconnected inlet and outlet branches of the interdigitated design also results in a high pressure-drop. Much of the pressure-drop occurs within the GDL, resulting in an even flow velocity throughout the GDL. As a result, the urea concentration gradient is less a function of the streamlines or pressure drop, but rather the distance fluid travels through the GDL. As can be seen in Figure 7.9, concentration gradients form primarily at the diagonals between the concave inlet channel corners and the convex outlet corners. For the interdigitated and constructal design patterns, this distance is equivalent throughout the active area. For the leaf design, however, the GDL lengths at the 45 °C are longer and result in a noticeably larger concentration gradient.

7.3.4 Mixed Channel Designs

By design, mixed channel patterns take on characteristics of the parent designs, as shown in Figure 7.10. The parallel-serpentine pattern has two side-by-side winding channels along the length of the GDL. Compared to the parallel design, however, the fluid velocity in the channels is not equal. One explanation for this phenomenon is the orientation of the fluid inlet, supported by the presence of a sharp pressure spike at the corner where the two channels diverge. The velocity profile in the bends of this design shows that fluid vortices form due to the multi-directional flow. Similar to the traditional serpentine design, the pressure-drop follows the channel direction. The concentration profile for this design shows an overall high amount of reactant utilization. Due to the parallel channels, two effective concentration profiles can be seen. The first is a single, serpentine-shaped area residing in between the channels. Here, the concentration gradient resembles that of the split channel designs with evenly utilized GDL utilization. The second concentration profile can be seen in the individual “digits” that the channels serpentine around. These profiles strongly resemble that of the traditional serpentine pattern due to the bidirectional flow. Both of the mixed-interdigitated designs studied here have the same characteristics of the

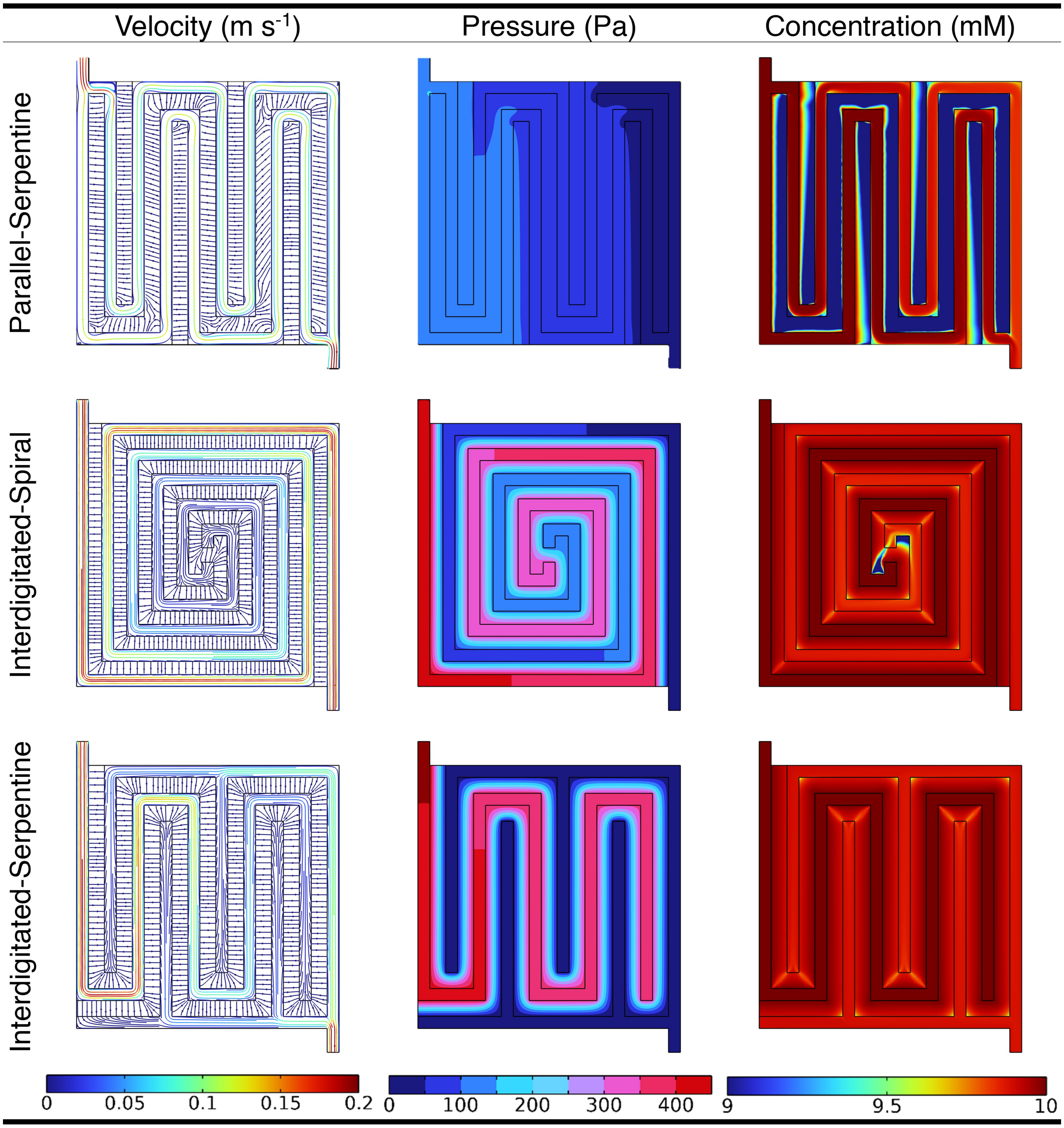

Figure 7.10: Velocity, pressure, and concentration profiles of the mixed flow patterns.

traditional interdigitated designs. The exception to this rule is that the longer channels result in a more noticeable pressure drop in the channels. The majority of the drop, however, still occurs in the GDL due to the disconnected inlet-outlet branches. The diagonal corners of the GDL develop a larger concentration gradient than other areas of the pattern.

7.3.5 Design Comparison

To quantify and compare the overall performance of the flow field patterns, values of particular interest are shown in Table 7.2. These values are the conversion (X / %), the pressure drop (Δp / Pa), the scaled conversion to pressure drop ratio ($X : \Delta p$), the area of the porous reacting media (A_{gdl} / cm^2), and the conversion per unit area (X_{A} / % cm^{-2}). The continuous conversion was evaluated by averaging the concentration of urea along the outlet line ($c_{\mathrm{u,out}}$) and using the following equation:

$$X = \frac{c_{0,\mathrm{u}} - c_{\mathrm{u,out}}}{c_{0,\mathrm{u}}} \tag{7.14}$$

The pressure drop is an important parameter for any type of portable, small form-factor device such as the URD as it dictates the accessory power loading of the stack.[133] Consequently, a low value is desired. From the patterns examined in this study, the parallel (36.9 Pa), Murrey-parallel (24.5 Pa), and grid (27.5 Pa) designs have significantly lower pressure drops than the other patterns by about an order of magnitude. The highest pressure drops were for the serpentine (452 Pa), spiral-interdigitated (451 Pa), and serpentine-interdigitated (460 Pa) designs, although all the non split-design patterns were comparably high. The exception here is the parallel-serpentine design, which only has a pressure drop of 160 Pa. The conversion to pressure drop ratio was evaluated by dividing the actual conversion by the pressure drop and applying a scaling factor (1000) to compare the relative performance of the flow field patterns. While the actual conversion of the split-channel designs is by far the lowest, these designs have a considerably higher ratio of conversion to pressure. For a system limited by form factor, using a design with a high conversion to pressure value results in a

Table 7.2: The conversion (X / %), pressure drop (Δp / Pa), conversion to pressure drop ratio ($X : \Delta p$), area of the porous reacting media (A_{gdl} / cm^2), and conversion per unit area (X_{A} / % cm^{-2}) for each of the flow field patterns shown in Figure 7.5, evaluated using the parameters from Table 7.1. Green cells are used to highlight the desirable values in each column, while the red are undesirable. Blue cells are used to show consistency.

Pattern	X / %	Δp / Pa	$X : \Delta p$	A_{gdl} / cm^2	X_{A} / % cm^{-2}
Serpentine	1.23	452	2.73	2.31	0.533
Multi-Serp.	0.979	399	2.45	2.4	0.407
Spiral	1.08	337	3.20	2.31	0.466
Parallel	0.496	36.9	13.4	2.6	0.191
Murray-Parallel	0.487	24.5	19.9	2.08	0.235
Grid	0.273	27.5	9.92	2.56	0.106
Interdigitated	1.18	405	2.91	2.53	0.465
Leaf	1.15	416	2.77	2.51	0.460
Constructal	1.14	387	2.93	2.45	0.463
Parallel-Serp.	1.28	160	8.01	2.51	0.512
Spiral-Interdig.	1.06	451	2.35	2.32	0.456
Serp.-Interdig.	1.17	460	2.55	2.53	0.463

lower auxiliary power cost. Out of the remaining designs, only the parallel-serpentine design had a comparable conversion to pressure value.

The tradeoff one makes by using a split design is the number of plates needed to remove the biologically relevant amount of urea (15 g day^{-1}).[113] While less auxiliary power may be needed, flow field plates make up over 60% of the weight of an electrolyzer stack.[133] Consequently, a portable device such as the URD also relies on the electrochemical cell having a high conversion per unit area (X_A / % cm^{-2}). Due to the channel width and GDL dimension constraints, it was not possible to have identical active areas for every pattern. As a result, the spacing between channels and the number of channels were varied to minimize differences in the GDL area, and the values ranged from 0.208 to 0.260 cm^2. When normalizing the conversion by the A_gdl, both the serpentine (5.33% cm^{-2}) and parallel-serpentine (5.12% cm^{-2}) patterns had the highest performance. The split channel designs were the lowest performing due to their low conversion rate.

It is also worth noting that, while performing at about 90% of the potential of a serpentine-design, all interdigitated channel designs have decidedly similar values of X_A; the margin of error was 4.61 ± 0.0351 % cm^{-2}. These results indicate that, using the model developed here, the pattern of an interdigitated type plate is not significant. Rather, the conversion is directly related to the active area, dictated by the number of channels and spacing between channels; when plotting the conversion *vs.* active area of the GDL (gray) for two types of interdigitated designs (Figure 7.11), it is clear that the active area — and not the arrangement of branches — is directly proportional to the calculated conversion. This is important to note, as it suggests the 2-D depth-averaged model may be oversimplifying the

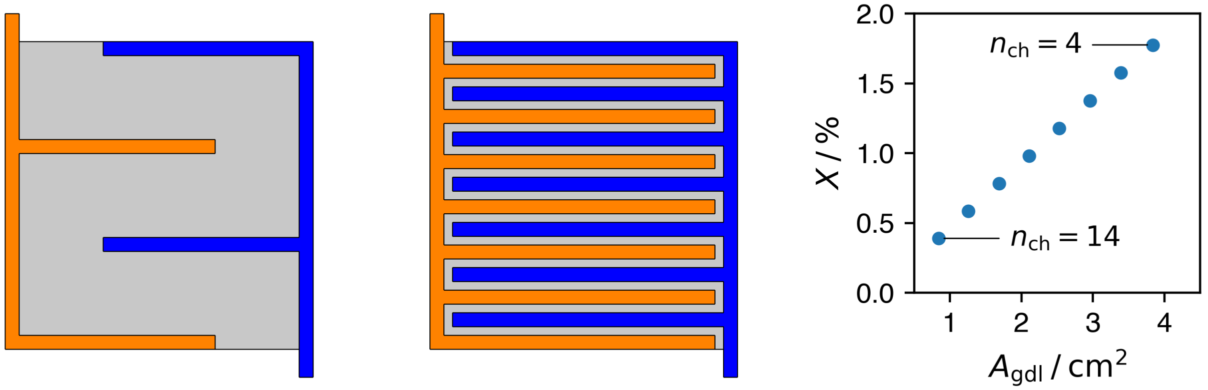

Figure 7.11: Flow field patterns for a (left) $n_\mathrm{ch} = 4$ and (middle) $n_\mathrm{ch} = 14$ layout. (Right) The resulting linear relationship between conversion and active area

relationship between interdigitated design and electrochemical conversion. Consequently, a more robust, 3-D model may be needed to properly investigate the role of channel geometry for interdigitated-type flow field plates.

7.4 Conclusions

In this section, computational fluid dynamics was used to evaluate the relative performance of different flow field patterns on the electrochemical oxidation of urea. A 2-D, depth-averaged model was used to expedite simulation times and allowed for rapid computational iterations. Three of each single, multi, interdigitated, and mixed-type channel designs were investigated, and practical parameters including the conversion and pressure drop used as benchmarks. It was determined that for the given flow conditions, a low urea concentration electrolyte, and the given electrochemical UOR parameters, a parallel-serpentine design provided the best overall performance. The parallel-serpentine pattern had the highest overall conversion, the second highest area-normalized conversion, and less than half the pressure drop of the other non-split channel designs.

Chapter 8

CONCLUSIONS AND PERSPECTIVES

The primary objective of this work was to advance our understanding of a developed oxide layer's role in the hydrogen evolution, oxygen evolution, and urea oxidation performance of nickel and nickel-chromium-molybdenum materials. Motivated by the need for advanced energy storage and production materials, we used a range of electrochemical methods to elucidate changes in oxide structure over 600 or more potential cycles and the resulting electrocatalytic surfaces in alkaline media.

8.0.1 Nickel-Chromium-Molybdenum Electrocatalysts

In Section 4.1, NiCrMo alloys were electrochemically cycled, and changes in the oxide layer were identified through voltammetry, coulometry, and materials characterization. In Chapter 5, the HER, OER, and UOR performance of these oxide structures were benchmarked using Tafel slope, turnover frequency, and overpotentials. It was determined that the dissolution of alloying elements was the cause of unique voltammogram features for each of the electrodes. While Cr and Mo leaching from Ni-based materials in alkaline media is not a novel finding, the study conducted here uncovered its role in the preferential formation of NiOOH phases; alloys with dissimilar amounts of Cr and Mo were more prone to electrochemical dissolution, increasing the electrochemical surface area and driving the formation of transport pathways through the outer oxide layer. The improved intercalation of cations and water molecules through these pathways enhanced formation of the γ-NiOOH phase.

During electrocatalytic benchmarking, it was determined that the dissimilar Cr:Mo alloys have lower OER turnover frequencies than pure Ni or the similar Cr:Mo alloy. Moreover, similar rate-determining steps and characteristic $Ni(OH)_2 \rightleftarrows NiOOH$ potentials implied that Cr and Mo as additives do not directly affect the OER and UOR kinetics. Differences in these benchmarking values are instead attributed to the varying β-NiOOH:γ-NiOOH concentrations, and each of these phases has significantly different electrocatalytic properties for each of the OER, HER, and UOR.

8.0.2 Nickel Phase Development

As a result of the studies conducted on NiCrMo alloys, it was apparent that a better understanding of the β-NiOOH and γ-NiOOH phases was necessary for development of Ni-based materials as HER, OER, and UOR electrocatalysts. In Chapter 6, selective cycling procedures were developed to target formation of the individual NiOOH phases. The resulting oxide structures were characterized using cyclic voltammetry and scanning electron microscopy, and their electrocatalytic properties benchmarked using impedance spectroscopy, Tafel analysis, and overpotentials.

The switching potential was used to control NiOOH formation, and it was shown that γ-NiOOH can be preferentially formed at higher potentials (1.61 V) due to enhanced oxygen evolution, while the more stable β-NiOOH phase formed at lower potentials (1.51 V). The NiOOH facets were captured using SEM, and a clear increase in grain boundaries was seen for the γ-NiOOH-developed electrode. Consequently, it was concluded that increased OER at higher switching potentials drives place-exchange mechanisms at the electrode-electrolyte interface, leading to surface roughening and jagged facet borders. A kinetics analysis of the NiOOH phases indicated that the β-NiOOH phase was considerably more active towards the OER as evidenced by lower overpotentials and higher turnover frequencies. Moreover, the improved kinetics of the β-NiOOH phase lasted for an extended time period compared to the γ-NiOOH phase.

8.0.3 CFD Modeling

In Chapter 7, a computational fluid dynamics study was conducted to determine the role of flow field pattern on the performance of a urea removal device. By using biologically relevant conditions and electrochemical parameters, a 2-D, depth-averaged models was used to screen three of each single, split, interdigitated, and mixed flow patterns. The low flow rate of the split designs resulted in a low pressure-drop, but the lack of under-rib flow prevented significant oxidation of urea from occurring. The interdigitated patterns had approximately the same conversion per area, suggesting that in these flow conditions, the pattern is insignificant compared to the total active area. Overall, the simulation results indicate that the traditional serpentine design and the parallel-serpentine design result in the highest urea conversion overall and on a per-area basis. Of these two designs, the parallel-serpentine pattern has a lower pressure drop, making it the most optimal design studied here.

8.0.4 Perspectives

In this work, the field of nickel-based alkaline catalysis has been advanced through the use of electroanalytical and materials characterization. Nickel-chromium-molybdenum alloys can be used to create high surface area electrodes with varying NiOOH-electrocatalytic properties by adjusting the Cr and Mo concentrations. The overpotentials of the HER, OER, and UOR were improved for certain Cr:Mo concentrations, indicating that more research into these alloying elements will yield a worthwhile electrocatalyst. Moreover, evidence for the rate-determining step of OER being the formation of NiOOH sites is shown through Tafel analysis, laying the foundation for studies on RDS-improvement. An additional finding of note is that the distinctions between these NiOOH phases are not evident until a substantial number of potential cycles have been conducted. Of the dozens of OER and UOR electroanalytical studies referenced in this work, however, only two used more than 30 potential cycles, and only one of those used more than 200. Accordingly, these works may not be representative of long-term activity and stability, and it is suggested that future studies on the electrocatalytic properties of NiOOH-based electrodes ensure adequate development of the oxide structure before benchmarking.

BIBLIOGRAPHY

1. *Total Energy Annual Data - U.S. Energy Information Administration (EIA)*
2. Schlapbach, L. & Züttel, A. Hydrogen-storage materials for mobile applications. *Nature* **414,** 353–358. doi:10.1038/35104634 (Nov. 2001).
3. Ardo, S. *et al.* Pathways to electrochemical solar-hydrogen technologies. *Energy & Environmental Science* **11,** 2768–2783. doi:10.1039/C7EE03639F (2018).
4. IEA. *Grid-Scale Storage* 2022.
5. Vaidyanathan ClimateWire, G. *How Bad of a Greenhouse Gas Is Methane?* en.
6. Encinas Fernández, J., Hofmann, H. & Peeters, F. Diurnal Pumped-Storage Operation Minimizes Methane Ebullition Fluxes From Hydropower Reservoirs. *Water Resources Research* **56.** doi:10.1029/2020WR027221 (Dec. 2020).
7. IEA. *The Role of Critical Minerals in Clean Energy Transitions* 2021.
8. *Nickel in batteries* en-US.
9. ASM International. in *Metals Handbook Desk Edition* 22–15 (1984).
10. Vij, V. *et al.* Nickel-Based Electrocatalysts for Energy-Related Applications: Oxygen Reduction, Oxygen Evolution, and Hydrogen Evolution Reactions. *ACS Catalysis* **7,** 7196–7225. doi:10.1021/acscatal.7b01800 (Oct. 2017).
11. *Publications - Dimensions* en.
12. Boggs, B. K., King, R. L. & Botte, G. G. Urea electrolysis: Direct hydrogen production from urine. *Chemical Communications,* 4859–4861. doi:10.1039/b905974a (2009).
13. McKee, D. W. & Pak, M. S. Electrocatalysts for Hydrogen Carbon Monoxide Fuel Cell Anodes. *Journal of The Electrochemical Society* **116,** 516. doi:10.1149/1.2411937 (1969).
14. Feitknecht, W., Christen, H. R. & Studer, H. Zur Kenntnis der hohern Nickelhydroxyde; die Oxydation von Nickelhydroxyd. *Zeitschrift for anorganische und allgemeine Chemie* **283,** 88–95. doi:10.1002/zaac.19562830111 (Jan. 1956).
15. Bode, H., Dehmelt, K. & Witte, J. Zur kenntnis der nickelhydroxidelektrode—I.Uber das nickel (II)-hydroxidhydrat. *Electrochimica Acta* **11,** 1079–1087. doi:10.1016/0013-4686(66)80045-2 (Aug. 1966).
16. Song, F. *et al.* An Unconventional Iron Nickel Catalyst for the Oxygen Evolution Reaction. *ACS Central Science* **5,** 558–568. doi:10.1021/acscentsci.9b00053 (Mar. 2019).

17. Juodkazis, K., Juodkazytė, J., Vilkauskaitė, R. & Jasulaitienė, V. Nickel surface anodic oxidation and electrocatalysis of oxygen evolution. *Journal of Solid State Electrochemistry* **12,** 1469–1479. doi:10.1007/s10008-007-0484-0 (Nov. 2008).

18. Van der Ven, A., Morgan, D., Meng, Y. S. & Ceder, G. Phase Stability of Nickel Hydroxides and Oxyhydroxides. *Journal of The Electrochemical Society* **153,** A210. doi:10.1149/1.2138572 (2006).

19. Oliva, P. *et al.* Review of the structure and the electrochemistry of nickel hydroxides and oxy-hydroxides. *Journal of Power Sources* **8,** 229–255. doi:10.1016/0378-7753(82)80057-8 (Jan. 1982).

20. Alsabet, M., Grden, M. & Jerkiewicz, G. Electrochemical Growth of Surface Oxides on Nickel. Part 2: Formation of β-Ni(OH)2 and NiO in Relation to the Polarization Potential, Polarization Time, and Temperature. *Electrocatalysis* **5,** 136–147. doi:10.1007/s12678-013-0172-z (Apr. 2014).

21. Alsabet, M., Grdeń, M. & Jerkiewicz, G. Electrochemical Growth of Surface Oxides on Nickel. Part 3: Formation of β-NiOOH in Relation to the Polarization Potential, Polarization Time, and Temperature. *Electrocatalysis* **6,** 60–71. doi:10.1007/s12678-014-0214-1 (Jan. 2015).

22. Hall, D. S., Lockwood, D. J., Bock, C. & MacDougall, B. R. Nickel hydroxides and related materials: a review of their structures, synthesis and properties. *Proceedings of the Royal Society A: Mathematical, Physical and Engineering Sciences* **471,** 20140792. doi:10.1098/rspa.2014.0792 (Feb. 2015).

23. Singh, D. Characteristics and Effects of γ-NiOOH on Cell Performance and a Method to Quantify It in Nickel Electrodes. *Journal of The Electrochemical Society* **145,** 116–120. doi:10.1149/1.1838222 (Jan. 1998).

24. Chen, Y., Rui, K., Zhu, J., Dou, S. X. & Sun, W. Recent Progress on Nickel-Based Oxide/(Oxy)Hydroxide Electrocatalysts for the Oxygen Evolution Reaction. *Chemistry – A European Journal* **25,** 703–713. doi:10.1002/chem.201802068 (Jan. 2019).

25. Alsabet, M., Grden, M. & Jerkiewicz, G. Electrochemical Growth of Surface Oxides on Nickel. Part 1: Formation of α-Ni(OH)2 in Relation to the Polarization Potential, Polarization Time, and Temperature. *Electrocatalysis* **2,** 317–330. doi:10.1007/s12678-011-0067-9 (Dec. 2011).

26. Barnard, R., Randell, C. F. & Tye, F. L. Studies concerning charged nickel hydroxide electrodes I. Measurement of reversible potentials. *Journal of Applied Electrochemistry* **10,** 109–125. doi:10.1007/BF00937345 (Jan. 1980).

27. Angeles-Olvera, Z. *et al.* Nickel-Based Electrocatalysts for Water Electrolysis. *Energies* **15,** 1609. doi:10.3390/en15051609 (Feb. 2022).

28. Shinagawa, T., Garcia-Esparza, A. T. & Takanabe, K. Insight on Tafel slopes from a microkinetic analysis of aqueous electrocatalysis for energy conversion. *Scientific Reports* **5,** 13801. doi:10.1038/srep13801 (Nov. 2015).
29. Yu, M., Budiyanto, E. & Tüysüz, H. Principles of Water Electrolysis and Recent Progress in Cobalt-, Nickel-, and Iron-Based Oxides for the Oxygen Evolution Reaction. *Angewandte Chemie International Edition* **61.** doi:10.1002/anie.202103824 (Jan. 2022).
30. Long, X. *et al.* A Strongly Coupled Graphene and FeNi Double Hydroxide Hybrid as an Excellent Electrocatalyst for the Oxygen Evolution Reaction. *Angewandte Chemie International Edition* **53,** 7584–7588. doi:10.1002/anie.201402822 (July 2014).
31. Swierk, J. R., Klaus, S., Trotochaud, L., Bell, A. T. & Tilley, T. D. Electrochemical Study of the Energetics of the Oxygen Evolution Reaction at Nickel Iron (Oxy)Hydroxide Catalysts. *The Journal of Physical Chemistry C* **119,** 19022–19029. doi:10.1021/acs.jpcc.5b05861 (Aug. 2015).
32. Song, F. & Hu, X. Exfoliation of layered double hydroxides for enhanced oxygen evolution catalysis. *Nature Communications* **5,** 4477. doi:10.1038/ncomms5477 (July 2014).
33. Wang, C. *et al.* Facet Engineering of Advanced Electrocatalysts Toward Hydrogen/Oxygen Evolution Reactions. *Nano-Micro Letters* **15,** 52. doi:10.1007/s40820-023-01024-6 (Dec. 2023).
34. Anantharaj, S. *et al.* High-Performance Oxygen Evolution Anode from Stainless Steel via Controlled Surface Oxidation and Cr Removal. *ACS Sustainable Chemistry & Engineering* **5,** 10072–10083. doi:10.1021/acssuschemeng.7b02090 (Nov. 2017).
35. Fu, S. *et al.* Highly Ordered Mesoporous Bimetallic Phosphides as Efficient Oxygen Evolution Electrocatalysts. *ACS Energy Letters* **1,** 792–796. doi:10.1021/acsenergylett.6b00408 (Oct. 2016).
36. Dionigi, F. *et al.* Intrinsic Electrocatalytic Activity for Oxygen Evolution of Crystalline 3d-Transition Metal Layered Double Hydroxides. *Angewandte Chemie - International Edition* **60,** 14446–14457. doi:10.1002/anie.202100631 (June 2021).
37. Ganesan, P., Sivanantham, A. & Shanmugam, S. Inexpensive electrochemical synthesis of nickel iron sulphides on nickel foam: super active and ultra-durable electrocatalysts for alkaline electrolyte membrane water electrolysis. *Journal of Materials Chemistry A* **4,** 16394–16402. doi:10.1039/C6TA04499A (2016).
38. McCrory, C. C. L. *et al.* Benchmarking Hydrogen Evolving Reaction and Oxygen Evolving Reaction Electrocatalysts for Solar Water Splitting Devices. *Journal of the American Chemical Society* **137,** 4347–4357. doi:10.1021/ja510442p (Apr. 2015).

39. Zhou, T. *et al.* Transition metal ions regulated oxygen evolution reaction performance of Ni-based hydroxides hierarchical nanoarrays. *Scientific Reports* **7,** 46154. doi:`10.1038/srep46154` (Apr. 2017).
40. Xia, C., Jiang, Q., Zhao, C., Hedhili, M. N. & Alshareef, H. N. Selenide-Based Electrocatalysts and Scaffolds for Water Oxidation Applications. *Advanced Materials* **28,** 77–85. doi:`10.1002/adma.201503906` (Jan. 2016).
41. Sumboja, A., Chen, J., Zong, Y., Lee, P. S. & Liu, Z. NiMn layered double hydroxides as efficient electrocatalysts for the oxygen evolution reaction and their application in rechargeable Zn–air batteries. *Nanoscale* **9,** 774–780. doi:`10.1039/C6NR08870H` (2017).
42. Collins, V. G. & Popma, D. C. *Space vehicle water reclamation systems* tech. rep. (1965).
43. YAO, S. J., WOLFSON, S. K., AHN, B. K. & LIU, C. C. Anodic Oxidation of Urea and an Electrochemical Approach to De-ureation. *Nature* **241,** 471–472. doi:`10.1038/241471a0` (1973).
44. Simka, W., Piotrowski, J. & Nawrat, G. Influence of anode material on electrochemical decomposition of urea. *Electrochimica Acta* **52,** 5696–5703. doi:`10.1016/j.electacta.2006.12.017` (May 2007).
45. Bolzan, A. & Iwasita, T. Determination of the volatile products during urea oxidation on platinum by on line mass spectroscopy. *Electrochimica Acta* **33,** 109–112. doi:`10.1016/0013-4686(88)80040-9` (Jan. 1988).
46. Wang, D., Yan, W., Vijapur, S. H. & Botte, G. G. Enhanced electrocatalytic oxidation of urea based on nickel hydroxide nanoribbons. *Journal of power sources* **217,** 498–502 (2012).
47. Vedharathinam, V. & Botte, G. G. Understanding the electro-catalytic oxidation mechanism of urea on nickel electrodes in alkaline medium. *Electrochimica Acta* **81,** 292–300 (2012).
48. Bard, A. J., Faulkner, L. R. & White, H. S. *Electrochemical methods: fundamentals and applications* (John Wiley \& Sons, 2022).
49. Yan, W., Wang, D. & Botte, G. G. Nickel and cobalt bimetallic hydroxide catalysts for urea electro-oxidation. *Electrochimica Acta* **61,** 25–30 (2012).
50. Miller, A. T., Hassler, B. L. & Botte, G. G. Rhodium electrodeposition on nickel electrodes used for urea electrolysis. *Journal of Applied Electrochemistry* **42,** 925–934 (2012).
51. Xu, D. *et al.* The role of Cr doping in Ni Fe oxide/(oxy)hydroxide electrocatalysts for oxygen evolution. *Electrochimica Acta* **265,** 10–18. doi:`10.1016/j.electacta.2018.01.143` (Mar. 2018).

52. Yang, D., Yang, L., Zhong, L., Yu, X. & Feng, L. Urea electro-oxidation efficiently catalyzed by nickel-molybdenum oxide nanorods. *Electrochimica Acta* **295,** 524–531. doi:10.1016/j.electacta.2018.10.190 (Feb. 2019).
53. Yang, D. *et al.* Nanostructured Ni ¡sub¿2¡/sub¿ P-C as an Efficient Catalyst for Urea Electrooxidation. *ChemElectroChem* **5,** 659–664. doi:10.1002/celc.201701304 (Feb. 2018).
54. Tatarchuk, S. W., Choueiri, R. M., Medvedeva, X. V., Chen, L. D. & Klinkova, A. Inductive effects in cobalt-doped nickel hydroxide electronic structure facilitating urea electrooxidation. *Chemosphere* **279,** 130550. doi:10.1016/j.chemosphere.2021.130550 (Sept. 2021).
55. Xu, H. *et al.* A branch-like Mo-doped Ni ¡sub¿3¡/sub¿ S ¡sub¿2¡/sub¿ nanoforest as a high-efficiency and durable catalyst for overall urea electrolysis. *Journal of Materials Chemistry A* **9,** 3418–3426. doi:10.1039/D0TA09423D (2021).
56. Lin, C. *et al.* ¡i¿In situ¡/i¿ growth of single-layered α-Ni(OH) ¡sub¿2¡/sub¿ nanosheets on a carbon cloth for highly efficient electrocatalytic oxidation of urea. *Journal of Materials Chemistry A* **6,** 13867–13873. doi:10.1039/C8TA05064C (2018).
57. Adhikari, S., Kwon, Y. & Kim, D.-H. Three-dimensional core–shell structured NiCo2O4@CoS/Ni-Foam electrocatalyst for oxygen evolution reaction and electrocatalytic oxidation of urea. *Chemical Engineering Journal* **402,** 126192. doi:10.1016/j.cej.2020.126192 (Dec. 2020).
58. Sha, L. *et al.* In situ grown 3D hierarchical MnCo2O4.5@Ni(OH)2 nanosheet arrays on Ni foam for efficient electrocatalytic urea oxidation. *Chemical Engineering Journal* **381,** 122603. doi:10.1016/j.cej.2019.122603 (Feb. 2020).
59. Daramola, D. A., Singh, D. & Botte, G. G. Dissociation Rates of Urea in the Presence of NiOOH Catalyst: A DFT Analysis. *The Journal of Physical Chemistry A* **114,** 11513–11521. doi:10.1021/jp105159t (Nov. 2010).
60. Li, J. *et al.* Deciphering and Suppressing Over-Oxidized Nitrogen in Nickel-Catalyzed Urea Electrolysis. *Angewandte Chemie International Edition* **60,** 26656–26662. doi:10.1002/anie.202107886 (Dec. 2021).
61. Yang, W. *et al.* Rapid room-temperature fabrication of ultrathin Ni(OH)2 nanoflakes with abundant edge sites for efficient urea oxidation. *Applied Catalysis B: Environmental* **259,** 118020. doi:10.1016/j.apcatb.2019.118020 (Dec. 2019).
62. Orazem, M. E. & Tribollet, B. *Electrochemical impedance spectroscopy* 2nd edition (Wiley, Hoboken, New Jersey, 2017).
63. Lacey, M. *Electrochemical Impedance Spectroscopy* en-us. May 2023.
64. Pine Research. *Electrochemcal Impedance Spectroscopy (EIS) Basics* en-US. Jan. 2022.
65. Gamry Instruments. *Basics of Electrochemical Impedance Spectroscopy*

66. Espinoza, E. M. *et al.* Practical Aspects of Cyclic Voltammetry: How to Estimate Reduction Potentials When Irreversibility Prevails. *Journal of The Electrochemical Society* **166,** H3175–H3187. doi:10.1149/2.0241905jes (Jan. 2019).
67. Murbach, M., Gerwe, B., Dawson-Elli, N. & Tsui, L.-k. impedance.py: A Python package for electrochemical impedance analysis. *Journal of Open Source Software* **5,** 2349. doi:10.21105/joss.02349 (Aug. 2020).
68. Cossar, E., Houache, M. S., Zhang, Z. & Baranova, E. A. Comparison of electrochemical active surface area methods for various nickel nanostructures. *Journal of Electroanalytical Chemistry* **870,** 114246. doi:10.1016/J.JELECHEM.2020.114246 (Aug. 2020).
69. Liu, L., Zhou, Z. & Peng, C. Sonochemical intercalation synthesis of nano γ-nickel oxyhydroxide: Structure and electrochemical properties. *Electrochimica Acta* **54,** 434–441. doi:10.1016/j.electacta.2008.07.055 (Dec. 2008).
70. Klapper, H. S., Zadorozne, N. S. & Rebak, R. B. Localized Corrosion Characteristics of Nickel Alloys: A Review. *Acta Metallurgica Sinica (English Letters)* **30,** 296–305. doi:10.1007/s40195-017-0553-z (Apr. 2017).
71. Forest, I.-S. The corrosion resistance of nickel-containing alloys in sulfuric acid and related compounds. *INCO The International Nickel Company* (1983).
72. Abd El-Haleem, S. & Abd El-Wanees, S. Chloride induced pitting corrosion of nickel in alkaline solutions and its inhibition by organic amines. *Materials Chemistry and Physics* **128,** 418–426. doi:10.1016/j.matchemphys.2011.03.023 (Aug. 2011).
73. Okuyama, M. & Haruyama, S. Passive film formed on nickel in a neutral solution. *Corrosion Science* **14,** 1–14. doi:10.1016/S0010-938X(74)80003-X (Jan. 1974).
74. MacDougall, B. & Graham, M. Pitting of nickel during anodic galvanostatic charging in Na2SO4 solutions. *Electrochimica Acta* **27,** 1093–1096. doi:10.1016/0013-4686(82)80115-1 (Aug. 1982).
75. Huang, L.-F., Hutchison, M. J., Santucci, R. J., Scully, J. R. & Rondinelli, J. M. Improved Electrochemical Phase Diagrams from Theory and Experiment: The Ni–Water System and Its Complex Compounds. *The Journal of Physical Chemistry C* **121,** 9782–9789. doi:10.1021/acs.jpcc.7b02771 (May 2017).
76. Mishra, A. & Shoesmith, D. The activation/depassivation of nickel–chromium–molybdenum alloys: An oxyanion or a pH effect—Part II. *Electrochimica Acta* **102,** 328–335. doi:10.1016/j.electacta.2013.03.177 (July 2013).
77. Lloyd, A. C., Noël, J. J., McIntyre, S. & Shoesmith, D. W. Cr, Mo and W alloying additions in Ni and their effect on passivity. *Electrochimica Acta* **49,** 3015–3027. doi:10.1016/j.electacta.2004.01.061 (July 2004).
78. Saji, V. S. & Lee, C.-W. Molybdenum, Molybdenum Oxides, and their Electrochemistry. *ChemSusChem* **5,** 1146–1161. doi:10.1002/cssc.201100660 (July 2012).

79. Ebrahimi, N., Biesinger, M. C., Shoesmith, D. W. & Noël, J. J. The influence of chromium and molybdenum on the repassivation of nickel-chromium-molybdenum alloys in saline solutions. *Surface and Interface Analysis* **49,** 1359–1365. doi:`10.1002/sia.6254` (Dec. 2017).

80. Zhao, J. *et al.* Ultra-thin wrinkled NiOOH–NiCr 2 O 4 nanosheets on Ni foam: an advanced catalytic electrode for oxygen evolution reaction. *Chemical Communications* **54,** 4987–4990. doi:`10.1039/C8CC01002A` (2018).

81. Singh, R. K. & Schechter, A. Electroactivity of NiCr Catalysts for Urea Oxidation in Alkaline Electrolyte. *ChemCatChem* **9,** 3374–3379. doi:`10.1002/CCTC.201700451` (Sept. 2017).

82. González-Buch, C., Herraiz-Cardona, I., Ortega, E., García-Antón, J. & Pérez-Herranz, V. Study of the catalytic activity of 3D macroporous Ni and NiMo cathodes for hydrogen production by alkaline water electrolysis. *Journal of Applied Electrochemistry* **46,** 791–803. doi:`10.1007/s10800-016-0970-0` (July 2016).

83. Li, R.-Q. *et al.* Energy-efficient hydrogen production over a high-performance bifunctional NiMo-based nanorods electrode. *Journal of Colloid and Interface Science* **571,** 48–54. doi:`10.1016/j.jcis.2020.03.023` (July 2020).

84. Shetty, S., Mohamed Jaffer Sadiq, M., Bhat, D. K. & Hegde, A. C. Electrodeposition and characterization of Ni-Mo alloy as an electrocatalyst for alkaline water electrolysis. *Journal of Electroanalytical Chemistry* **796,** 57–65. doi:`10.1016/j.jelechem.2017.05.002` (July 2017).

85. Pissinis, D. E., Sereno, L. E. & Marioli, J. M. Utilization of Special Potential Scan Programs for Cyclic Voltammetric Development of Different Nickel Oxide-Hydroxide Species on Ni Based Electrodes. *Open Journal of Physical Chemistry* **02,** 23–33. doi:`10.4236/ojpc.2012.21004` (2012).

86. Chen, Z. *et al.* One-step facile synthesis of nickel–chromium layered double hydroxide nanoflakes for high-performance supercapacitors. *Nanoscale Advances* **2,** 2099–2105. doi:`10.1039/D0NA00178C` (2020).

87. Haynes International. *Corrosion-resistant Alloys*

88. Research Solutions & Resources LLC. *Hg/HgO Reference Electrode*

89. Clark, E. L. *et al.* Standards and Protocols for Data Acquisition and Reporting for Studies of the Electrochemical Reduction of Carbon Dioxide. *ACS Catalysis* **8,** 6560–6570. doi:`10.1021/acscatal.8b01340` (July 2018).

90. Ping, H. *et al.* Electrochemical Oxidation of Metal Chromium in odium Hydroxide Aqueous Solution. *Journal of Electrochemistry* **26,** 413. doi:`10.13208/J.ELECTROCHEM.190710` (June 2020).

91. Lyons, M. E. G., Doyle, R. L., Godwin, I., O'Brien, M. & Russell, L. Hydrous Nickel Oxide: Redox Switching and the Oxygen Evolution Reaction in Aqueous Alkaline Solution. *Journal of The Electrochemical Society* **159,** H932–H944. doi:10.1149/2.078212jes (Jan. 2012).

92. ThermoFisher Scientific. *Nickel Periodic Table - US* en.

93. Biesinger, M. *Nickel*

94. ThermoFisher Scientific. *Chromium Periodic Table - US* en.

95. Biesinger, M. *Chromium*

96. Yeo, B. S. & Bell, A. T. In Situ Raman Study of Nickel Oxide and Gold-Supported Nickel Oxide Catalysts for the Electrochemical Evolution of Oxygen. *The Journal of Physical Chemistry C* **116,** 8394–8400. doi:10.1021/jp3007415 (Apr. 2012).

97. Colli, A. N., Girault, H. H. & Battistel, A. Non-Precious Electrodes for Practical Alkaline Water Electrolysis. *Materials* **12,** 1336. doi:10.3390/ma12081336 (Apr. 2019).

98. Clayton, C. R. & Lu, Y. C. A Bipolar Model of the Passivity of Stainless Steel: The Role of Mo Addition. *Journal of The Electrochemical Society* **133,** 2465–2473. doi:10.1149/1.2108451 (Dec. 1986).

99. Wikstrom, L. L. & Nobe, K. The Electrochemical Behavior of Molybdenum. *Journal of The Electrochemical Society* **116,** 525. doi:10.1149/1.2411941 (1969).

100. Hayes, J. R., Gray, J. J., Szmodis, A. W. & Orme, C. A. Influence of Chromium and Molybdenum on the Corrosion of Nickel-Based Alloys. *CORROSION* **62,** 491–500. doi:10.5006/1.3279907 (June 2006).

101. Mangel Raventos, A. & Kortlever, R. Effect of different alkali metal cations on the oxygen evolution activity and battery capacity of nickel electrodes in concentrated hydroxide electrolytes. *Electrochimica Acta* **415,** 140255. doi:10.1016/j.electacta.2022.140255 (May 2022).

102. Kamath, P. Suppression of the $\alpha \rightarrow \beta$-nickel hydroxide transformation in concentrated alkali: Role of dissolved cations. *Journal of Applied Electrochemistry* **31,** 1315–1320. doi:10.1023/A:1013876006707 (Dec. 2001).

103. Anantharaj, S., Karthik, P. E. & Noda, S. The Significance of Properly Reporting Turnover Frequency in Electrocatalysis Research. *Angewandte Chemie International Edition* **60,** 23051–23067. doi:10.1002/anie.202110352 (Oct. 2021).

104. Lyons, M. E. & Brandon, M. P. A comparative study of the oxygen evolution reaction on oxidised nickel, cobalt and iron electrodes in base. *Journal of Electroanalytical Chemistry* **641,** 119–130. doi:10.1016/j.jelechem.2009.11.024 (Mar. 2010).

105. Lin, Z., Bu, P., Xiao, Y., Gao, Q. & Diao, P. β- and γ-NiFeOOH electrocatalysts for an efficient oxygen evolution reaction: an electrochemical activation energy aspect. *Journal of Materials Chemistry A* **10,** 20847–20855. doi:10.1039/D2TA04688A (2022).

106. Armstrong, R., Bell, M. & Metcalfe, A. A. The anodic dissolution of molybdenum in alkaline solutions — electrochemical measurements. *Journal of Electroanalytical Chemistry and Interfacial Electrochemistry* **84,** 61–72. doi:`10.1016/S0022-0728(77)80228-3` (Nov. 1977).

107. Lian, K. K., Kirk, D. W. & Thorpe, S. J. Investigation of a "Two-State" Tafel Phenomenon for the Oxygen Evolution Reaction on an Amorphous Ni-Co Alloy. *Journal of The Electrochemical Society* **142,** 3704–3712. doi:`10.1149/1.2048402` (Nov. 1995).

108. Arulmozhi, N., Esau, D., Lamsal, R. P., Beauchemin, D. & Jerkiewicz, G. Structural Transformation of Monocrystalline Platinum Electrodes upon Electro-oxidation and Electro-dissolution. *ACS Catalysis* **8,** 6426–6439. doi:`10.1021/acscatal.8b00319` (July 2018).

109. Jacobse, L. *et al.* Electrochemical oxidation of Pt(111) beyond the place-exchange model. *Electrochimica Acta* **407,** 139881. doi:`10.1016/j.electacta.2022.139881` (Mar. 2022).

110. Li, X., Cui, X. & Jiang, L. Low-temperature and anhydrous preparation of NixFey-LDHs as an efficient electrocatalyst for water and urea electrolysis. *Catalysis Communications* **162,** 106390. doi:`10.1016/j.catcom.2021.106390` (Feb. 2022).

111. Bates, M. K., Jia, Q., Ramaswamy, N., Allen, R. J. & Mukerjee, S. Composite Ni/NiO-Cr ¡sub¿2¡/sub¿ O ¡sub¿3¡/sub¿ Catalyst for Alkaline Hydrogen Evolution Reaction. *The Journal of Physical Chemistry C* **119,** 5467–5477. doi:`10.1021/jp512311c` (Mar. 2015).

112. Prasad, R. Fertilizer urea, food security, health and the environment. *Current Science* **75,** 677–683 (1998).

113. Van Gelder, M. K. *et al.* Urea removal strategies for dialysate regeneration in a wearable artificial kidney. *Biomaterials* **234,** 119735. doi:`10.1016/j.biomaterials.2019.119735` (Mar. 2020).

114. Dose, W. M. *et al.* The influence of electrochemical cycling protocols on capacity loss in nickel-rich lithium-ion batteries. *Journal of Materials Chemistry A* **9,** 23582–23596 (2021).

115. Lyons, M. & Brandon, M. The Oxygen Evolution Reaction on Passive Oxide Covered Transition Metal Electrodes in Aqueous Alkaline Solution. Part 1-Nickel. *Int. J. Electrochem. Sci. International Journal* **3,** 1386–1424 (Mar. 2008).

116. Iwamoto, M., Yoda, Y., Yamazoe, N. & Seiyama, T. *Study of Metal Oxide Catalysts by Temperature Programmed Desorption. 4. Oxygen Adsorption on Various Metal Oxides* tech. rep. 24 (1978). doi:`https://doi.org/10.1021/j100513a006.`.

117. Lee, S. B., Yoon, D. Y., Hwang, N. M. & Henry, M. F. Grain boundary faceting and abnormal grain growth in nickel. *Metallurgical and Materials Transactions A* **31,** 985–994. doi:`10.1007/s11661-000-0040-3` (Mar. 2000).

118. Randle, V. & Horton, D. Grain growth phenomena in nickel. *Scripta Metallurgica et Materialia* **31,** 891–895. doi:10.1016/0956-716X(94)90498-7 (Oct. 1994).

119. Esau, D. *et al.* Controlled-Atmosphere Flame Fusion Growth of Nickel Poly-oriented Spherical Single Crystals—Unraveling Decades of Impossibility. *Electrocatalysis* **11,** 1–13. doi:10.1007/s12678-019-00575-w (Jan. 2020).

120. Doyle, R. L. & Lyons, M. E. G. An electrochemical impedance study of the oxygen evolution reaction at hydrous iron oxide in base. *Physical Chemistry Chemical Physics* **15,** 5224. doi:10.1039/c3cp43464h (2013).

121. Dau, H. *et al. The Mechanism of Water Oxidation: From Electrolysis via Homogeneous to Biological Catalysis* July 2010. doi:10.1002/cctc.201000126.

122. Mellsop, S. R., Gardiner, A., Johannessen, B. & Marshall, A. T. Structure and transformation of oxy-hydroxide films on Ni anodes below and above the oxygen evolution potential in alkaline electrolytes. *Electrochimica Acta* **168,** 356–364. doi:10.1016/j.electacta.2015.04.020 (June 2015).

123. Straumal, B. B., Kogtenkova, O. A., Gornakova, A. S., Sursaeva, V. G. & Baretzky, B. Review: grain boundary faceting–roughening phenomena. *Journal of Materials Science* **51,** 382–404. doi:10.1007/s10853-015-9341-1 (Jan. 2016).

124. Papawassiliou, W. *et al.* Crystal and electronic facet analysis of ultrafine Ni2P particles by solid-state NMR nanocrystallography. *Nature Communications* **12,** 4334. doi:10.1038/s41467-021-24589-5 (July 2021).

125. Couser, W. G., Remuzzi, G., Mendis, S. & Tonelli, M. The contribution of chronic kidney disease to the global burden of major noncommunicable diseases. *Kidney International* **80,** 1258–1270. doi:10.1038/ki.2011.368 (Dec. 2011).

126. Evangelidis, N. *et al.* Developing a Set of Core Outcomes for Trials in Hemodialysis: An International Delphi Survey. *American Journal of Kidney Diseases* **70,** 464–475. doi:10.1053/j.ajkd.2016.11.029 (Oct. 2017).

127. Rose, C., Parker, A., Jefferson, B. & Cartmell, E. The Characterization of Feces and Urine: A Review of the Literature to Inform Advanced Treatment Technology. *Critical Reviews in Environmental Science and Technology* **45,** 1827–1879. doi:10.1080/10643389.2014.1000761 (Sept. 2015).

128. Zhang, B., Lei, Y., Bai, B. & Zhao, T. A two-dimensional model for the design of flow fields in vanadium redox flow batteries. *International Journal of Heat and Mass Transfer* **135,** 460–469. doi:10.1016/j.ijheatmasstransfer.2019.02.008 (June 2019).

129. Patzer, J. F., Yao, S. J., Wolfson, S. K. & Ruppel-Kerr, R. Urea oxidation kinetics via cyclic voltammetry. *Journal of Electroanalytical Chemistry and Interfacial Electrochemistry* **276,** 341–353. doi:10.1016/0022-0728(89)87276-6 (Dec. 1989).

130. Dickinson, E. *Modeling Surface Reactions in Porous Media and Reactive Pellet Beds* en. 2017.

131. Hazar, H., Yilmaz, M. & Sevinc, H. The effects of different flow field patterns on polymer electrolyte membrane fuel cell performance. *Energy Conversion and Management* **248,** 114818. doi:10.1016/j.enconman.2021.114818 (Nov. 2021).

132. Amarnath, G. & Babu, A. V. Comparative computational fluid dynamic analysis between split and dual serpentine flow field for proton exchange membrane fuel cells. *Chemical Papers.* doi:10.1007/s11696-023-02841-0 (Apr. 2023).

133. Sauermoser, M., Kizilova, N., Pollet, B. G. & Kjelstrup, S. Flow Field Patterns for Proton Exchange Membrane Fuel Cells. *Frontiers in Energy Research* **8.** doi:10.3389/fenrg.2020.00013 (Feb. 2020).

134. Çelik, E. & Karagöz, İ. Polymer electrolyte membrane fuel cell flow field designs and approaches for performance enhancement. *Proceedings of the Institution of Mechanical Engineers, Part A: Journal of Power and Energy* **234,** 1189–1214. doi:10.1177/0957650919893543 (Dec. 2020).

135. Tang, Y., Yuan, W., Pan, M. & Wan, Z. Feasibility study of porous copper fiber sintered felt: A novel porous flow field in proton exchange membrane fuel cells. *International Journal of Hydrogen Energy* **35,** 9661–9677. doi:10.1016/j.ijhydene.2010.06.101 (Sept. 2010).

136. Jang, J.-Y., Cheng, C.-H., Liao, W.-T., Huang, Y.-X. & Tsai, Y.-C. Experimental and numerical study of proton exchange membrane fuel cell with spiral flow channels. *Applied Energy* **99,** 67–79. doi:10.1016/j.apenergy.2012.04.011 (Nov. 2012).

137. Spiegel, C. *Flow-Field Design*

Appendix A

PROCEDURES

A.1 Electrode polishing

To minimize noise and ensure that the reproducible electrochemical data, a polished electrode was used during all experiments. The procedure for creating a polished electrode is shown below, and the resulting electrode presented in Figure A.1.

1. Support the electrode sheet to be cut using a C-clamp or other vise.
2. Use a Dremel rotary tool with cut-off attachment to cut the electrode to size.
3. Clean the electrode with ethanol and DI water, allow to dry completely, and tape to the underside of specimen-holder.
4. Place a 400 grit silicon-carbide sandpaper sheet on the mechanical sander (Buehler Ecomet III), followed by a small amount of water to hydrate the surface.
5. While holding the specimen-holder firmly with one hand, turn the mechanical sander on to the lowest setting.
6. Slowly increase the rotational speed to its maximum setting.
7. When the mechanical sander is at its maximum speed, with one hand controlling the specimen holder and the other placed on top, press down to lower the electrode to the sanding surface.
8. Move the specimen holder in a slow, circular pattern counter to the direction of the mechanical sander's rotation.
9. After 1 full rotation, rotate the specimen-holder 180○, then complete a second rotation.
10. Check the electrode by lifting the specimen-holder off the sandpaper, flipping it over, and flushing with DI. Turn off the mechanical sander. If there are no major scratches, divots, bumps, etc. on the electrode surface, it is ready for the next sandpaper grit. Otherwise, repeat steps 5–9 again.

11. Flush the electrode with DI water until no loose particles remain on the surface. Repeat steps 4-10 using the next highest grit sandpaper.

12. After polishing with the highest grit sandpaper, a smooth, semi-reflective surface with no scratches should be obtained.

13. Remove the electrode from the specimen-holder, then flush with ethanol and DI repeatedly to ensure no particles remain.

14. Using a polishing pad and 9-micron diamond suspension, move the electrode in a figure-8 motion for 1 minute. Flush the electrode with ethanol and DI water.

15. Repeat step 14 using 3-micron diamond suspension, then again with 1-micron diamond suspension.

A number of variations of this procedure were used in this work, including the additional use of a Dremel felt-tipped attachment and buffing paste to improve the reflectivity of the surface. In all cases, the resulting electrode surface was effectively smoothed to the point of no visible blemishes or defects.

Figure A.1: Resulting electrode after polishing procedure.

A.2 Electrochemical Procedures

A variety of different electrochemical experiments were conducted in this work, and a step-by-step breakdown is included below.

A.2.1 Cell and Electrode preparation

1. Clean the three-electrode cell using concentrated H_2SO_4 to minimize iron contamination from the glassware.
2. Fill the three-electrode cell with KOH, then submerge two platinum electrodes and the Hg/HgO reference electrode.
3. Pre-electrolyze the solution at a potential of –0.54 V_{RHE} for 1 hour to remove remaining electrolyte contaminants.
4. Polish and prepare NiCrMo electrode during the pre-electrolysis period, then replace the platinum working electrode with the NiCrMo electrode.

A.2.2 Oxide Development and OER/UOR Benchmarking of NiCrMo Alloys

1. Follow the cell and electrode preparation process using 0.1 M KOH
2. Potential Hold: –0.54 V_{RHE} for 20 minutes to remove residual air-formed oxide layer.
3. CV: 0.85–1.52 V_{RHE}, 50 mV s^{-1}, x50
4. CV: 0.85–1.52 V_{RHE}, 1 mV s^{-1}, x3
5. ECSA measurement (as described in Chapter 3)
6. Repeat steps 6–8 a total of fourteen times for a total of 700 fast scans, 42 slow scans, and 14 ECSA measurements.
7. After the 14th “block” is completed, add KOH pellets while stirring until a 1 M KOH electrolyte (pH 14) is reached.
8. Potential Step: 1.47–1.62 V_{RHE} in 10 mV, 15 minute increments.
9. CV: 1.12–1.62 V_{RHE}, 15 mV s^{-1}, x75
10. CV: 1.12–1.62 V_{RHE}, 1 mV s^{-1}, x2

11. Add urea pellets to the electrolyte while stirring to create a 1 M KOH + 0.01 M urea solution
12. Repeat steps 12–13
13. Add urea pellets to the electrolyte while stirring to create a 1 M KOH + 0.33 M urea solution
14. Repeat steps 12–13

A.2.3 HER Benchmarking of NiCrMo Alloys

1. Follow the cell and electrode preparation process using 1 M KOH
2. CV: 0–0.46 V_{RHE}, 30 mV s^{-1}, x30
3. CV: 0–0.46 V_{RHE}, 1 mV s^{-1}, x1

A.2.4 Selective Development of NiOOH on Nickel

1. Follow the cell and electrode preparation process using 0.5 M KOH
2. Potential Hold: –0.49 V_{RHE} for 20 minutes to remove residual air-formed oxide layer.
3. CV: 0.90–X V_{RHE}, 10 mV s^{-1}, x600, (X is initially 1.51 V)
4. EIS: 1.51–1.66 V V_{RHE}, 10 mV increments, $f = 100000 - 0.1$ Hz, 5 mV amplitude
5. Repeat steps 1–4, increasing X by 20 mV. Repeat until values of 1.51, 1.53, 1.55, 1.57, 1.59, and 1.61 V have been completed

A.3 Data Processing

Due to the significant number of potential cycles used, manual processing of the data was not possible. CorrWare — the software used for data collection — outputs data as a ".cor" file, which can be opened in any text-editor. The following Python code is used to automatically extract potential (E), current (i), and time (t) data from the .cor files and output them as a dataframe:

```
def CV_import(file,strng,FILES):
with open(file) as input_data:
    for k,line in enumerate(input_data):
        if line.strip() == ’End Comments’:
            break

    dfTEMP = pd.DataFrame()
    E_val = []
    i_val = []
    t_val = []

    for line in (input_data):
        arr = line.split(’\t’)
        arr = [float(x) for x in arr]
        E,i,t = arr[0],arr[1],arr[2]

        E_val.append(E)
        i_val.append(i)
        t_val.append(t)

    dfTEMP[strng+’-E’] = E_val
    dfTEMP[strng+’-i’] = i_val
    dfTEMP[strng+’-t’] = t_val
    FILES.append(dfTEMP)
```

```
df = pd.DataFrame()
FILES = []
alloy_list = [’Ni’,’G35’,’B3’,’C276’]

for i,alloy in enumerate(tqdm(alloy_list)):
    direc = r’G:\My Drive\Electrochemical Data\Oxide’+’\\’+alloy

    criteria = [’slow’,’Cy02’] # Only accesses files with these terms in
                                         the filename
    file_list = [x for x in glob.glob(direc+’/*.cor’) if all(c in x for c
                                         in criteria)]

    for q,file in enumerate(file_list):

        block = str(file.split(’_Cy’)[0].split(’_’)[-1]) # Splits filepath
                                              based on these strings
        strng = ’-’.join([alloy,block])

        CV_import(file,strng,FILES)

df = pd.concat(FILES,axis=1)
df.head()
```

Appendix B

ADDITIONAL WORK

B.1 Catalyst Development

As part of the urea oxidation reaction research, alternate electrocatalysts were investigated for their urea oxidation capabilities and their chloride-resistance characteristics.

Catalyst	Substrate	Procedure	Results
$NiFe(OH)_2$	Stainless Steel 316	Electrolysis · 1 M KOH · 75°C, 10 hours	No urea EO, not stable in Cl^- conditions
$Ni(OH)_2$	Stainless Steel 316	Hydrothermal · 5 mM urea · 1 mM $Ni(NO_3)_2$ · 120°C, 12 hours	Biologically relevant urea EO. Difficult to deposit catalyst, not stable in Cl^- conditions
$Ni(OH)_2$	Stainless Steel 316	Hydrothermal · 100 mM urea · 20 mM $Ni(NO_3)_2$ · 120°C, 12 hours	Biologically relevant urea EO, marginally higher than previous test. Difficult to deposit catalyst, not stable in Cl^- conditions
$NiFe(OH)_2$	Stainless Steel 316	Solution-phase · 2.7 M NaOH · 0.133 M APS · 25°C, 18 hours	No urea EO, not stable in Cl^- conditions
MgO_2	Nickel Foam	Hydrothermal · 400 mM $KMnO_4$ · 180°C, 24 hours	Biologically relevant urea EO, low E_{ons}. Not stable in Cl^- conditions

$NiCr(OH)_2$	Nickel Foam	Hydrothermal · 100 mM urea · 20 mM $Ni(NO_3)_2$ · 10 mM $Cr(NO_3)_3$ · 160°C, 18 hours	Biologically relevant urea EO, low E_{ons}. Less inhibited in Cl^- conditions, but still unstable
$NiFe(OH)_2$	Sulfur-doped Nickel Foam	Solvothermal · 52 mM Toluene · 150°C, 5 hours Hydrothermal · 100 mM urea · 20 mM $Ni(NO_3)_2$ · 6 mM $Fe(NO_3)_3$ · 160°C, 18 hours	Poor sulfur deposition, no urea EO
$NiFe(OH)_2{-}S$	Nickel Foam	Solution phase · 800 mM $Fe(NO_3)_3$ · 20 mM $Na_2S_2O_3$ · 25°C, 5 minutes	Fast synthesis time, biologically relevant urea EO. Kinetics slowed with Cl^-, inconsistent at neutral pH
$Ni(OH)_2{-}S$	Nickel Foam	Hydrothermal · 25 mM APS · 150°C, 24 hours	Only sulfur is hydrothermally deposited, high urea EO, not limited by Cl^- at pH 14

Table B.1: Summary of catalyst development for investigation of urea EO in Cl^--containing media.

A select few of the developed catalysts' electrochemical responses are shown in Figure B.1. It was clear that all the developed electrodes were active towards urea, as seen by the current increase between 0.50–0.625 $V_{\text{Hg/HgO}}$ when urea was added to the solution (black to red). The increase in current for the Cr-doped electrode was higher than the base $Ni(OH)_2$ electrode, while the Fe-doped electrode was the lowest. The implication here is that the addition of Cr improves the UOR on a $Ni(OH)_2$-based catalyst, while doping with Fe acts as an inhibitor. Moreover, when Cl^- is added to the electrolyte, it acts as an inhibitor towards the UOR.

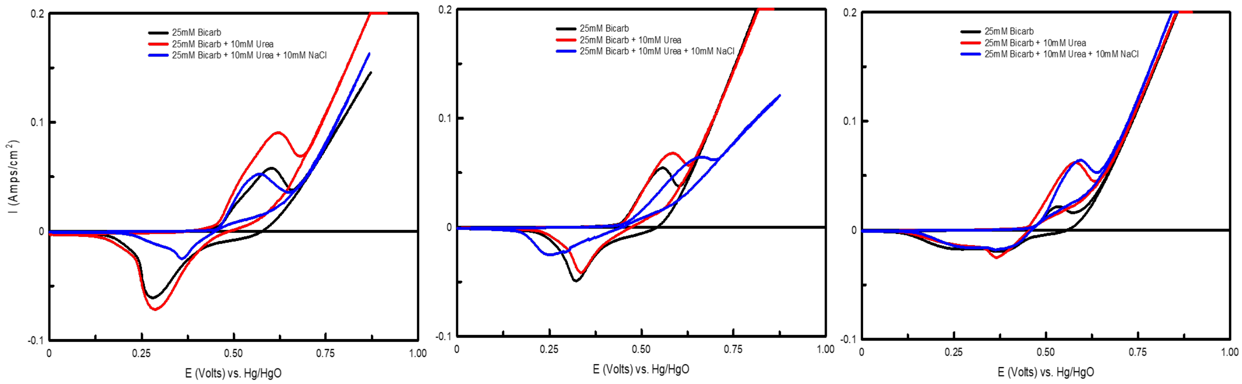

Figure B.1: Electrochemical response for (left) $Ni(OH)_2$, (middle) $NiFe(OH)_2$–S, and (right) $NiCr(OH)_2$ in 1 M KOH plus (black) 25 mM bicarbonate, (red) 25 mM bicarbonate + 10 mM urea, and (blue) 25 mM bicarbonate + 10 mM urea + 10 mM NaCl.

As seen in Figure B.1(a), there is a decrease in current back down to the approximate original current with no urea or Cl^- addition. It is suggested that nickel's strong affinity for Cl^- results in blocking of active sites, inhibiting the UOR and OER while still allowing the $Ni(OH)_2$ to NiOOH oxidation reaction to occur. The effect is even more noticeable in Figure B.1(b), as the current slope decreases dramatically throughout the entire UOR and OER responses. In Figure B.1(c), however, the addition of Cr seems to inhibit the effect of Cl^-. One possible explanation for this is the formation of $CrCl_3$ species; due to the dissolution of Cr from the electrode, the free Cr(III) ions may act as a “magnet” for the Cl^-, freeing up active sites.

B.2 Oxide Layer Thickness Estimation

As part of the NiCrMo oxide development process, an experimental procedure for estimating the relative thickness of the oxyhydroxide layer was tested. The two oxide models used to describe the structure are shown in Figure B.2

In the split — or ideal — model, the oxide structure is assumed to be made up of a metal substrate, an inner compact layer and a separate, porous, outer layer. Using nickel as an

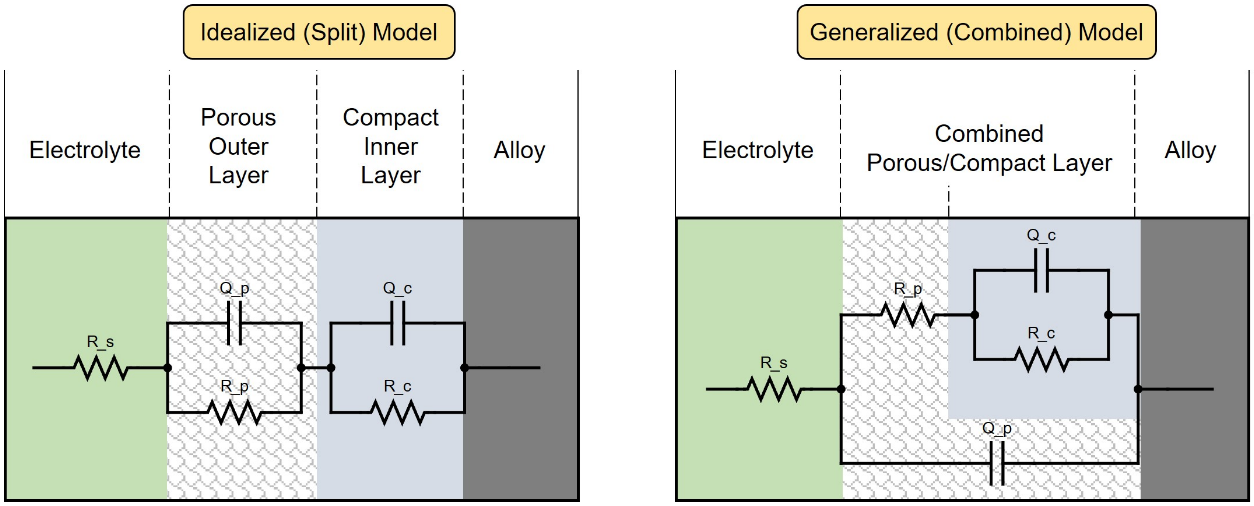

Figure B.2: Two of the possible equivalent circuit models to represent the structure of an electrochemically formed oxide layer on NiCrMo in alkaline medium.

analogy, this would be Ni^0, NiO, and $Ni(OH)_2/NiOOH$, respectively. In the generalized — or combined — model, the inner compact layer is assumed to have defects, pores, etc., that result in the formation of a mixed porous-compact layer. For nickel, this would be a combined NiO and $Ni(OH)_2/NiOOH$ layer. Both of these models have very similar characteristic equivalent circuit shapes, but they differ in the resulting parameter values.

After conducting EIS near the onset of the $Ni(OH)_2$ to NiOOH transition, the equivalent circuits shown above were fit to the data, and an example Nyquist plot for each of the NiCrMo alloys is shown in Figure B.3 The Nyquist plots are comparable in shape for most of the electrodes, but the scale is not. The upper limit of the arc ranges from 3000–25000 Ω depending on the electrode. For alloys G35 and C276, the data is best fit by a single, large semicircle, while for alloy B3 and pure Ni, the data is made up of two clear features, assumed to be semicircles as well. Using the impedance equation for a capacitor:

$$Z = \frac{1}{Q_o\left(j\omega\right)^n} \tag{B.1}$$

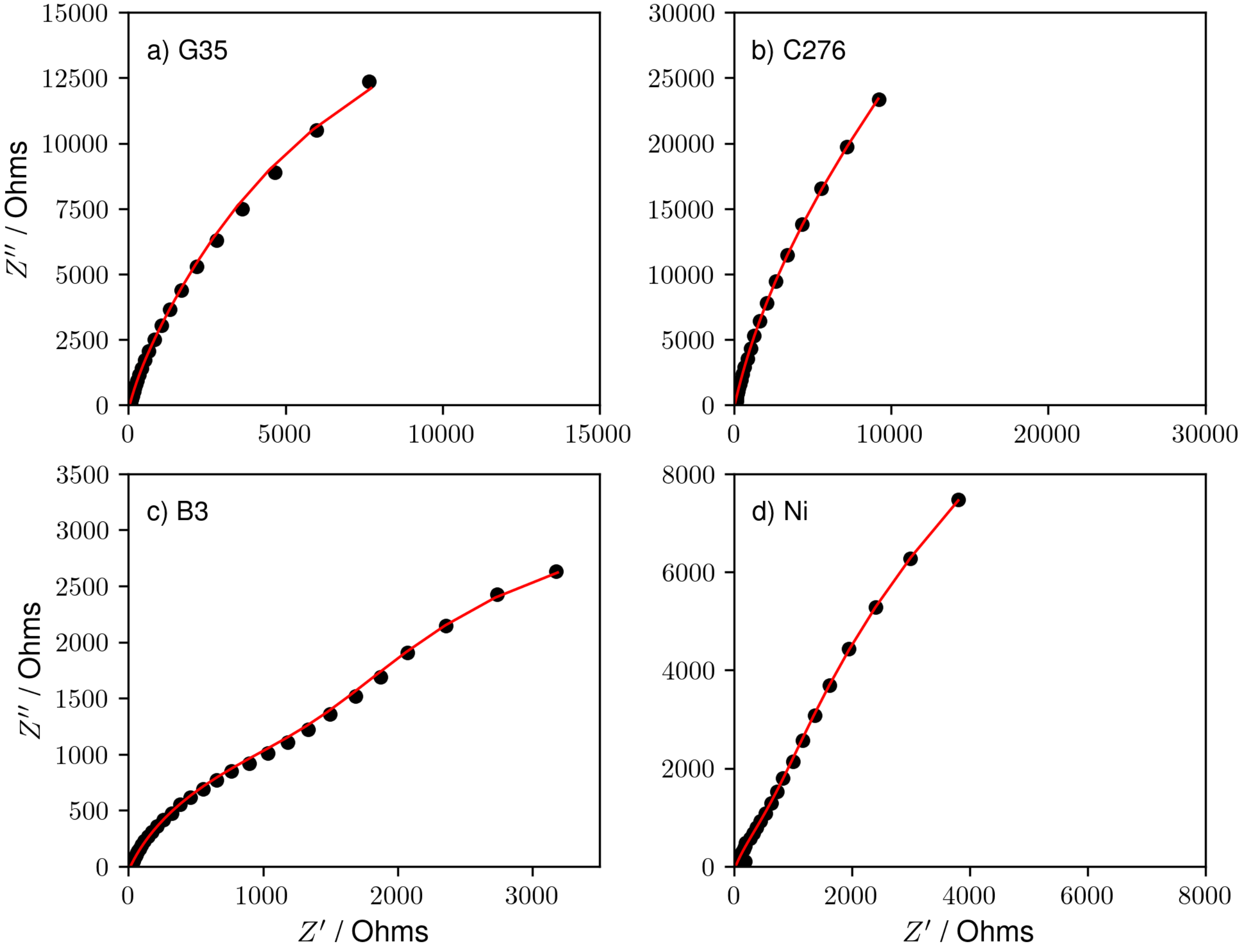

Figure B.3: Impedance spectra measured at 1.4 V_{RHE} using a 5 mV amplitude and from 100000–0.1 Hz in 0.5 M KOH for each of the NiCrMo alloys and pure Ni. The equivalent circuit used to fit the data (red line) was the generalized model, shown in Figure B.2.

the effective capacitance can be estimated:

$$C_{\mathrm{eff}} = \frac{(Q_{\mathrm{o}}R)^{\frac{1}{n}}}{R} \tag{B.2}$$

From the effective capacitance, the steady-state oxide layer thickness (L_{ss}) can be estimated:

$$L_{\mathrm{ss}} = \frac{\epsilon\epsilon_{\mathrm{o}}A}{C_{\mathrm{eff}}} \tag{B.3}$$

where *epsilon* is the relative dielectric constant (~ 12), ϵ_o is the permittivity of free space ($8.854 \times 10^{-12}\,\mathrm{F\,m^{-1}}$), and A is the area of the electrode. Evaluating this parameter for each of the oxide models described in Figure B.2 results in the estimated thickness for (each) oxide layer, as shown in Figure B.4 In the split model, two separate oxide layers are identified: the outer, porous hydroxide layer and the inner, compact oxide layer. The total thickness is largest for alloy C276 (4.5 nm), followed by G35 (3.7 nm), B3 (3.1 nm), and pure Ni (2.7 nm). The proportion of outer to inner oxide thickness is approximately equal for all electrodes except alloy B3, which has a significantly larger outer layer than inner layer. In the generalized model, the same trend in total oxide thickness is seen, but the values are approximately 20% smaller.

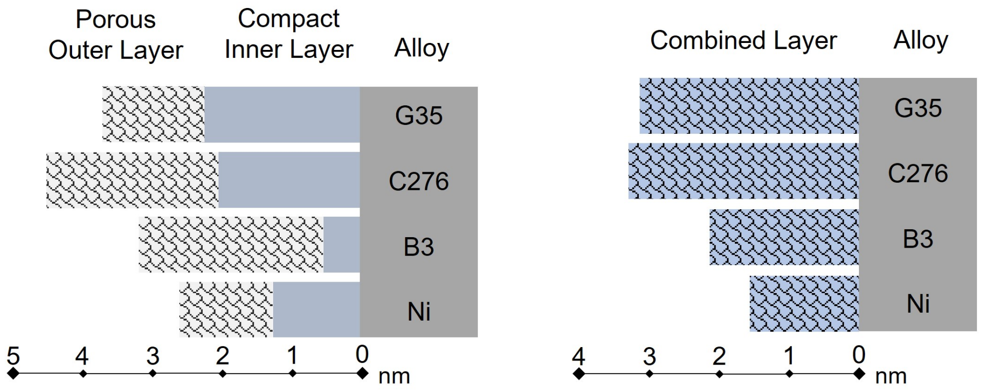

Figure B.4: Estimated oxide layer thicknesses for the (left) split model and (right) combined model.

This process was repeated over the course of 150 cycles for alloy G35. For each cycle, the values of L_{ss} were estimated and are plotted in Figure B.5. In the combined model, the data is relatively noisy, and the resulting confidence band does not provide very much evidence of how the oxide layer is changing with time. Using the split mode, however, there is a clear trend in oxide thickness with cycle; the outer, porous hydroxide layer increases in thickness over the course of 150 cycles, while the inner, compact layer decreases. These

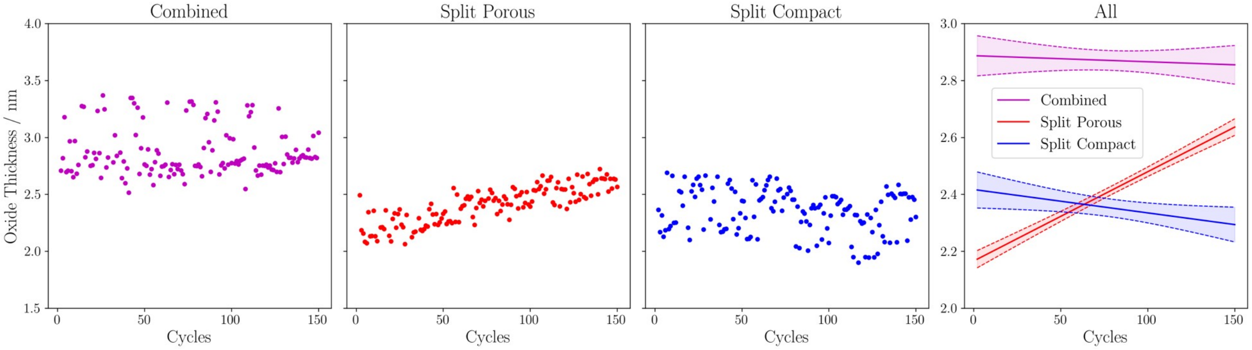

Figure B.5: Estimated oxide thickness as a function of potential cycle for alloy G35 using the (a) combined model and (b-c) split model. (c) Linear regression fit to the data with a 95% confidence band.

results suggest that, throughout electrochemical cycling, the inner, compact layer is being replaced by the thicker, outer porous layer. This is consistent with the electrochemical development results seen throughout this work; due to lattice expansion and contraction, transport pathways through the oxide layer form, exposing fresh Ni and NiO. These compact oxides are electrochemically converted to $Ni(OH)_2$ in the presence of hydroxide ions, resulting in growth of the outer, porous hydroxide layer.

While these results are consistent with the analysis conducted in the body of this work, there are a few unknowns that make its validity questionable. The primary reason is that the actual oxide structure is not known. The addition of Cr and Mo cause formation of multi-layered hydroxides with unknown structures. It would be presumptuous to assume that either the split or generalized model accurately represents the oxide structure without a more in-depth materials characterization and analysis. For this reason, the oxide thickness modeling using EIS was left out of the main body and included here.

B.3 Nickel-Phase Impedance Spectroscopy

As part of the investigation into how the switching potential affects the resulting oxide layer and OER performance, EIS was conducted between 1.51 V and 1.66 V for each of the electrodes. In Figure B.6, EIS using E_{dc} biases between 1.51 V and 1.56 V are shown for each of the electrodes. In Figure B.7, EIS using E_{dc} biases between 1.57 V and 1.66 V are shown for each of the electrodes.

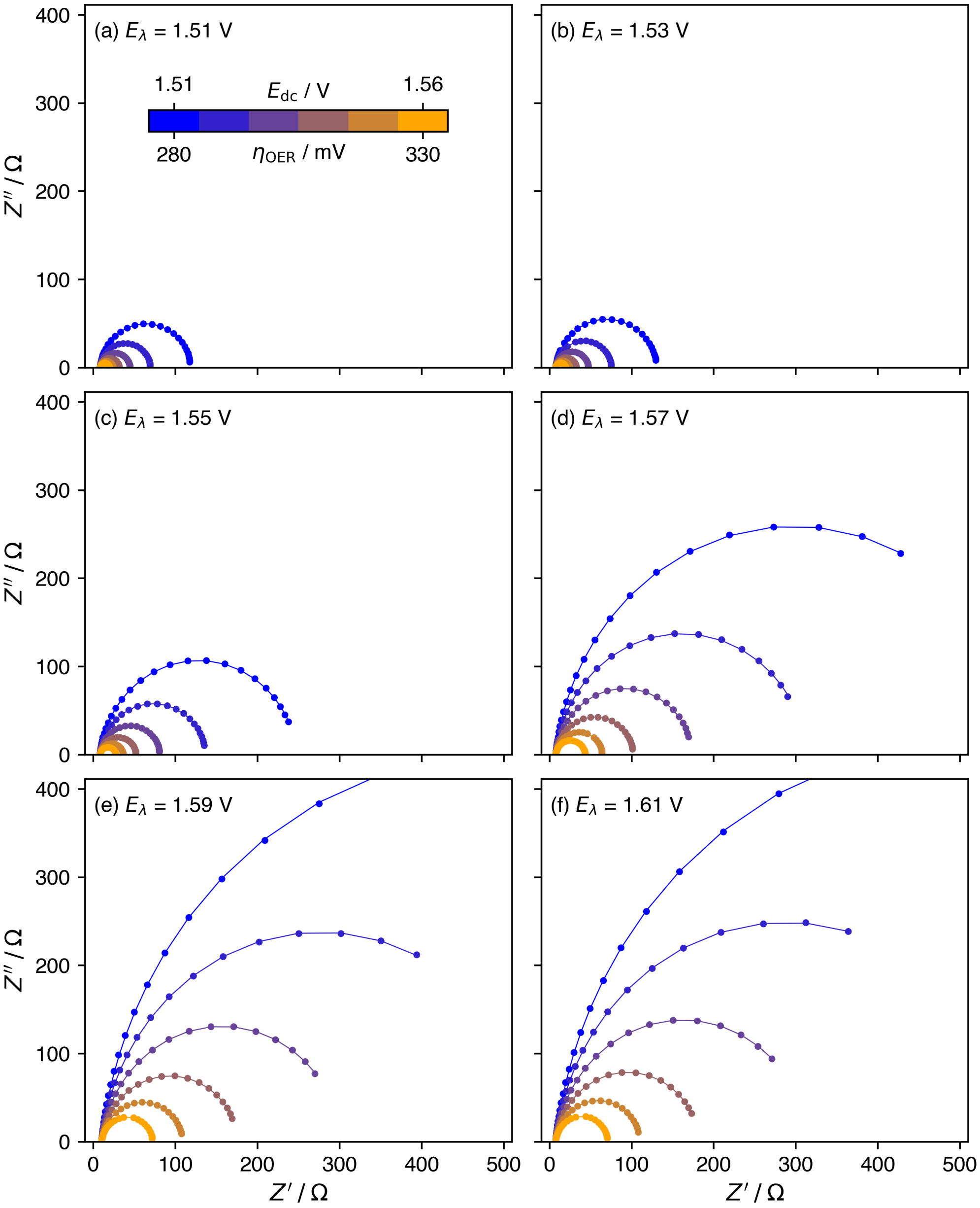

Figure B.6: Nyquist plots evaluated between E_{dc} values of 1.51 V (blue) and 1.56 V (orange) for electrodes developed with switching potentials (a) 1.51 V to (f) 1.61 V.

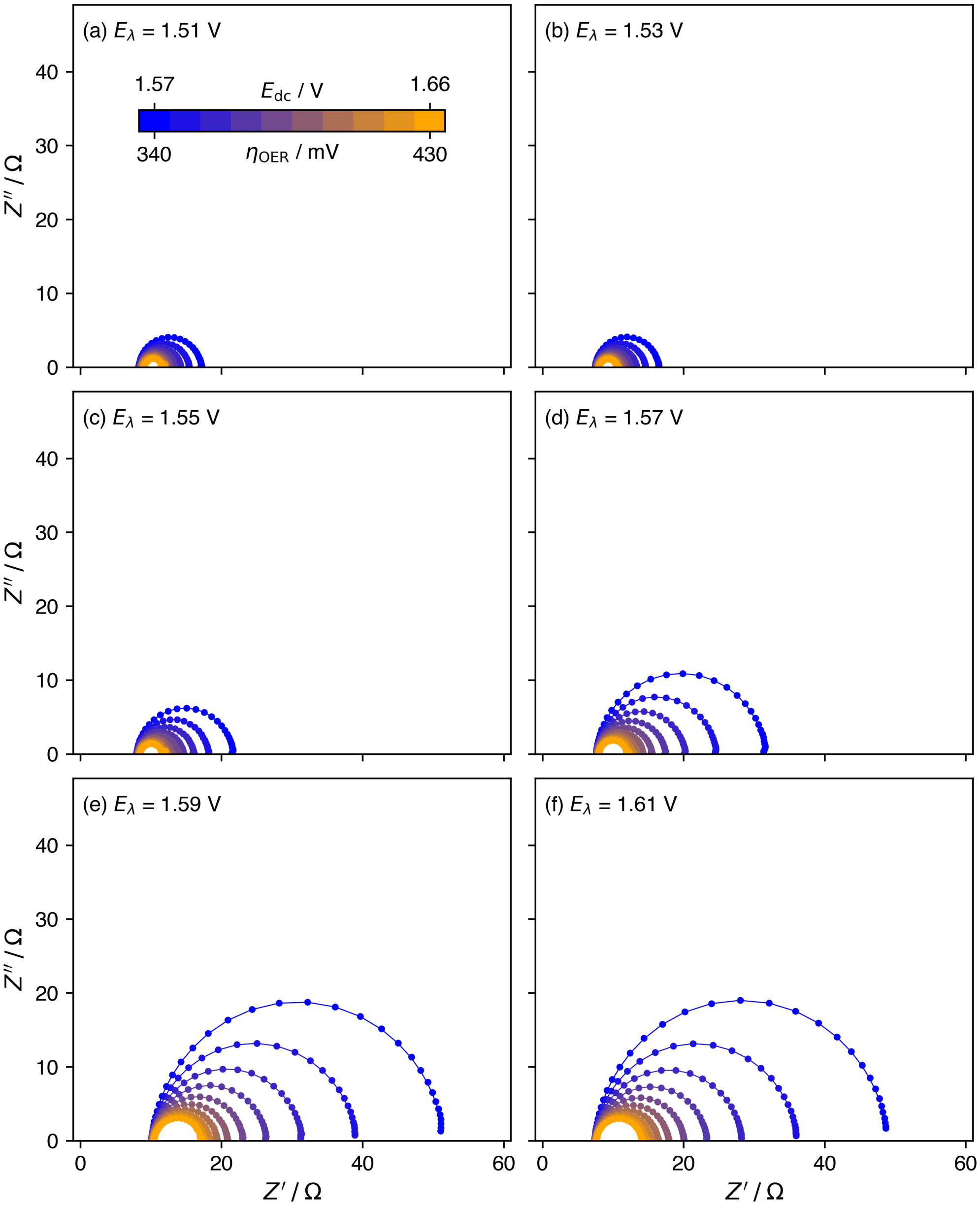

Figure B.7: Nyquist plots evaluated between E_{dc} values of 1.57 V (blue) and 1.66 V (orange) for electrodes developed with switching potentials (a) 1.51 V to (f) 1.61 V.

The Nyquist plots can be summarized in the following way:

- For all biases and switching potentials, the simplified Randles circuit provides an accurate fit for the characteristic shape: a semicircle shifted along the real impedance axis

- With increasing E_{dc} bias (blue to orange), the size of the semicircles decrease. The leftmost point of the semicircle (high-frequency), stays approximately constant for each E_{dc} bias.

- With increasing switching potential (a to f), the size of the semicircles increase. The leftmost point of the semicircle (high-frequency), stays approximately constant for each switching potential.

In Figure B.8, parameters extracted using the simplified Randles circuit are shown as a function of E_{dc} bias (x-axis) for each of the electrodes. The ohmic resistance, R_{e}, encapsulates the electrolyte and electrical resistances. This value increases slightly with E_{dc}, but not so significantly as to assume a significant change is occurring in the system. The ohmic resistance for a switching potential of 1.55 V is noticeably higher than the other switching potentials, and is assumed to be an outlier. The charge-transfer resistance, R_{ct}, decreases with EIS bias. As a higher overpotential is applied, the OER becomes more favorable, and R_{ct} decreases. Consequently, the charge-transfer resistance can be used as a performance benchmark of the OER, where a lower value indicates a more active surface. With increasing switching potential — and increasing γ-NiOOH concentration — the charge-transfer resistance increases, implying the γ-NiOOH phase is less active than the β-NiOOH phase.

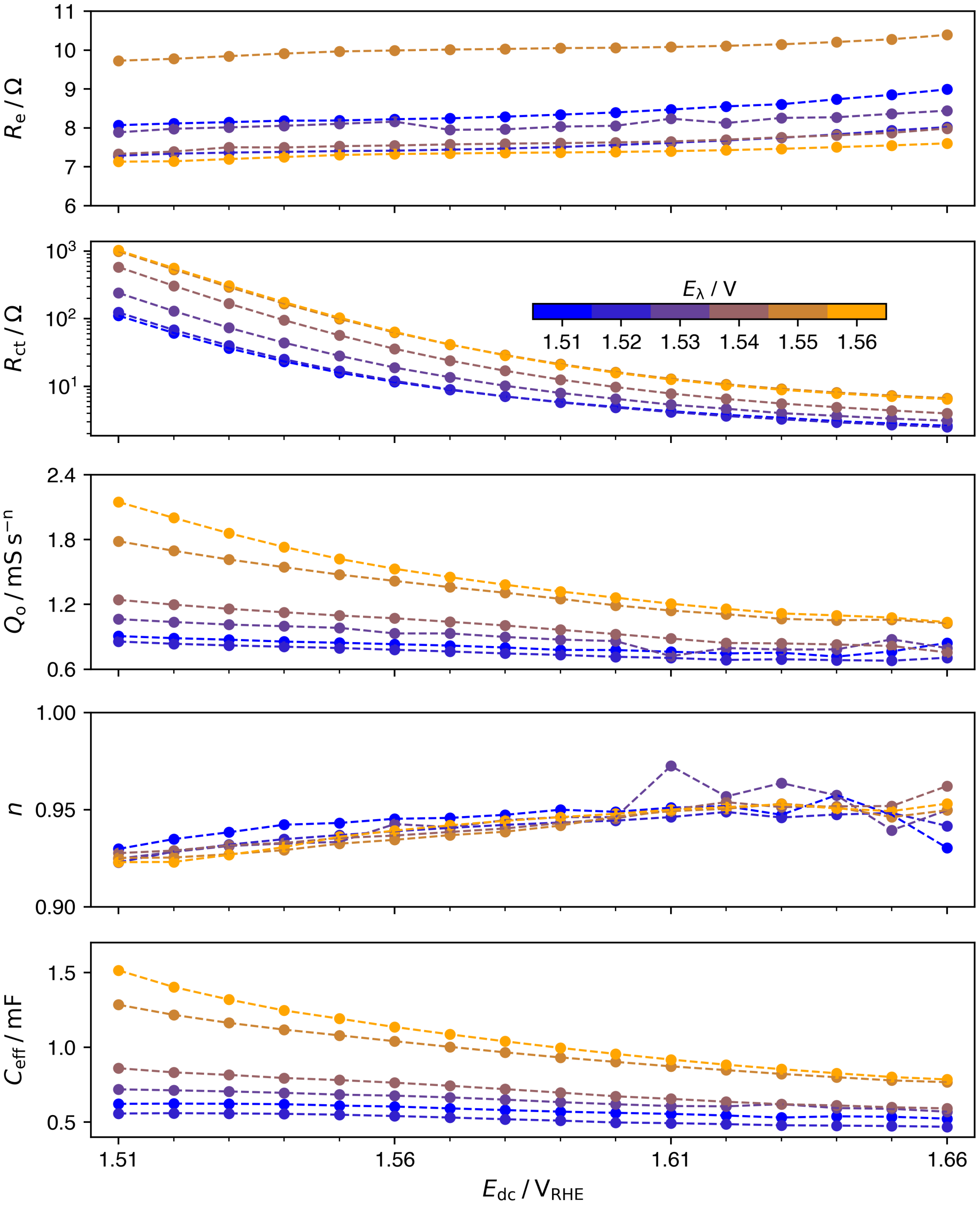

Figure B.8: Extracted equivalent circuit parameters as a function of applied EIS potential for each switching potential, including the ohmic resistance (R_e), charge-transfer resistance (R_{ct}), CPE parameter (Q_o), CPE exponent (n), and the effective capacitance (C_{eff})